LEVEL II

(12)

DNA 5471F

AD A102523

REQUIREMENTS FOR IMPROVED INFRARED PREDICTION CAPABILITY: LWIR

Douglas H. Archer

Mission Research Corporation

P.O. Drawer 719

Santa Barbara, California 93102

31 October 1980

Final Report fo Period 31 October 1979—31 October 1980

CONTRACT No. DNA 001-79-C-0116

DTIC FILE COPY

Prepared for

Director

DEFENSE NUCLEAR AGENCY

Washington, D. C. 20305

81 8 05 017

Destroy this report when it is no longer
needed. Do not return to sender.

PLEASE NOTIFY THE DEFENSE NUCLEAR AGENCY,
ATTN: STTI, WASHINGTON, D.C. 20305, IF
YOUR ADDRESS IS INCORRECT, IF YOU WISH TO
BE DELETED FROM THE DISTRIBUTION LIST, OR
IF THE ADDRESSEE IS NO LONGER EMPLOYED BY
YOUR ORGANIZATION.

REPORT DOCUMENTATION PAGE	READ INSTRUCTIONS BEFORE COMPLETING FORM

1. REPORT NUMBER	2. GOVT ACCESSION NO.	3. RECIPIENT'S CATALOG NUMBER
DNA 5471F	AD-A102 523	

4. TITLE (and Subtitle)	5. TYPE OF REPORT & PERIOD COVERED
REQUIREMENTS FOR IMPROVED INFRARED PREDICTION CAPABILITY:LWIR	Final Report for Period 31 Oct 79 — 31 Oct 80
	6. PERFORMING ORG. REPORT NUMBER
	MRC-R-583

7. AUTHOR(s)	8. CONTRACT OR GRANT NUMBER(s)
Douglas H. Archer	DNA 001-79-C-0116

9. PERFORMING ORGANIZATION NAME AND ADDRESS	10. PROGRAM ELEMENT PROJECT TASK AREA & WORK UNIT NUMBERS
Mission Research Corporation P.O. Drawer 719 Santa Barbara, California 93102	Subtask S99QAXHI004-30

11. CONTROLLING OFFICE NAME AND ADDRESS	12. REPORT DATE
Director Defense Nuclear Agency Washington, D. C. 20305	31 October 1980
	13. NUMBER OF PAGES
	130

14. MONITORING AGENCY NAME & ADDRESS(if different from Controlling Office)	15. SECURITY CLASS (of this report)
	UNCLASSIFIED
	15a. DECLASSIFICATION DOWNGRADING SCHEDULE N/A

16. DISTRIBUTION STATEMENT (of this Report)

Approved for public release, distribution unlimited.

17. DISTRIBUTION STATEMENT (of the abstract entered in Block 20, if different from Report)

19. KEY WORDS (Continue on reverse side if necessary and identify by block number)
Infrared Prediction
Infrared Radiation
Infrared Research Requirements
Nuclear-Induced Infrared
Uncertainties (Infrared)

20. ABSTRACT (Continue on reverse side if necessary and identify by block number)
This report describes work performed to determine the major uncertainties involved in the prediction of the long wavelength infrared (LWIR) environment following a megaton-class, high-altitude burst. Included for consideration is emission from the molecular species O_3, NO_2, N_2O, CO_2, uranium- and fission-fragment oxide ions, and from electrons in the fireball plume. A priority listing is provided of recommended research items necessary for improvement of our prediction capability.

DD FORM 1 JAN 73 1473 EDITION OF 1 NOV 65 IS OBSOLETE

TABLE OF CONTENTS

LIST OF ILLUSTRATIONS

LIST OF ILLUSTRATIONS (continued)

LIST OF ILLUSTRATIONS (continued)

SECTION 1
INTRODUCTION

Reasonably accurate prediction of the infrared environment following atmospheric nuclear bursts is necessary for a realistic assessment of its impact on the performance of defensive infrared systems. Such prediction entails a knowledge of various quantities including the principal radiating species, their optical properties, excitation and quenching mechanisms, disturbed air chemistry, and bomb phenomenology. In most instances, not all of the quantities are known with sufficient accuracy to provide an adequate representation of the infrared environment. This report, along with an earlier companion volume (Reference 1-1), attempts to pinpoint the major uncertainties associated with our infrared prediction capability in a nuclear environment and to make recommendations for a research effort designed to improve the prediction accuracy. Reference 1-1 dealt with the shorter-wave infrared region from about 2 to 5 μm. This report deals with the long-wave infrared (LWIR) region at wavelengths greater than about 5 or 6 μm.

LWIR sensor systems are valuable for use in detection and tracking of relatively cold objects whose thermal emission peaks at wavelengths in the LWIR region. Sight paths that intersect the earth's surface, or nearly so, will tend to be avoided by such systems so that the signal from the tracked object will not be obscured by the large earth-background emission. Thus, viewing aspects will be upward-looking or, at worst, limb-viewing with the sight path nadir at a high enough altitude to sufficiently reduce the limb radiance.

In the work reported here, we have attempted to determine how window regions* in the ambient atmosphere, under limb-viewing conditions, are modified in a nuclear environment. The extent to which a species is excited to radiate and fill a window region is taken as a measure of the importance of that species under nuclear-burst conditions. Uncertainties in the radiating properties (including excitation/deexcitation mechanisms, etc.) of the most important of the species are identified so that a prioritized listing of needed research items can be delineated. Uncertainties arising from inadequate knowledge of nuclear-burst phenomenology, however, which in some cases may overshadow those associated with the chemical/optical phenomena, generally lie outside the scope of the present effort. The one exception is the case of metal oxides where differences arising from different models of debris deposition are considered.

The procedure adopted was to first identify those molecular species known to radiate in the LWIR region. Next we estimated the limb-viewing window regions existing in the ambient atmosphere at limb altitudes between 60 and 200 km as determined from high-latitude rocket field data, from published calculations of earth-limb radiance, and from our own calculations of ambient chemiluminescent processes. We then utilized results of prior MHD/chemistry code runs for high-yield, high-altitude bursts to estimate the burst effects in the windows from each of the species of potential importance above 60 km. Included in these considerations are limb-radiance effects from plasma in high-altitude fireball plumes. These results were then used as a yardstick to measure the relative importance of the various species and mechanisms expected to contribute to the LWIR nuclear environment, and to formulate a priority listing of needed data to upgrade our prediction capability.

---

* A window region is defined in terms of a threshold radiance such that the radiance is less than the threshold at all wavelengths in the window.

Section 2 presents the results of our survey to identify the potentially important LWIR molecular emitters and wavelength bands, and provides a graphical estimate of the ambient limb windows.

Section 3 contains our work on the determination of limb radiances in a nuclear environment and assessment of the principal emitters and uncertainties associated with prediction of the radiation. Included for consideration are the species O_3, NO_2, N_2O, CO_2, and metal oxides, with emphasis on their LWIR emission following a megaton-class high-altitude burst. Specifically treated are chemiluminescence from O_3 and NO_2, photon excitation of N_2O formed by reaction between $N_2(A^3\Sigma)$ and O_2, CO_2 vibraluminescence, and photon excitation of metal oxides. Special attention is paid to oxides of aluminum, uranium, and fission fragments. Results of MICE-Code calculations are used to estimate the vertical distribution of the oxides and to determine the resulting limb radiances. Also included is a comparison between the molecular emissions and plasma radiation from the fireball plume. Uncertainties in key quantities needed for calculation of the radiation from each species, along with required work to reduce them, are identified in the appropriate subsections.

Finally, Section 4 gives a summary of our findings and presents an overall priority listing of recommended field, laboratory, and theoretical research programs needed to upgrade our modeling capability for the LWIR.

SECTION 2
SPECIES IDENTIFICATION
AND AMBIENT LIMB WINDOWS

SPECIES IDENTIFICATION

The species of potential importance in the LWIR can be divided
into two classes: (1) those that exist in the ambient atmosphere and,
(2) those that are formed following a nuclear detonation. Table 2-1 is a
listing, in order of increasing wavelength, of LWIR bands, the transitions
that give rise to them, and the associated species. Also shown (Column 4)
is the type of each species, i.e., whether it exists in the ambient atmosphere
or is formed from the bomb material, the fission fragments, weapon carrier,
etc. The last column in Table 2-1 shows the approximate altitude region
where the species may be important* in the limb-viewing mode in the ambient
or nuclear environment as inferred from work to be described later.

The listing of metal oxides in Table 2-1 is not necessarily very
complete, particularly those of the fission fragments and their ions whose
spectroscopic properties are generally not well known. Furthermore, the
precise altitude region over which certain of the species could be important
is rather uncertain, especially for the metal oxides, although the last
column in Table 2-1 is an attempt to provide realistic estimates that may
be valid at various times following a high-yield burst at altitudes above
100 km. For D-region bursts, the upper limit on altitude for the metal
oxides will be determined by the fireball stabilization altitude which will

---

* Based on a threshold radiance of 10^{-10} watts cm^{-2} $ster^{-1}$ μm^{-1}.

Table 2-1. Some LWIR bands and radiators of potential importance in a nuclear environment.

Band Center (μm)	Transition	Species	Species Type	Altitude (h) (km)
5.85	NO_2 assym. stretch	HNO_3	ambient	60
6.19	001-000	NO_2	ambient	110
6.27	010-000	H_2O	ambient	100
6.51	ν_2	CH_4	ambient	100
7.20	010-000	HO_2	ambient	100
7.52	NOH bend	HNO_3	ambient	60
7.55	NO_2 symm. stretch	HNO_3	ambient	60
7.57	100-000	NO_2	ambient	130
7.66	ν_4	CH_4	ambient	100
7.78	100-000	N_2O	ambient	230*
9.01	100-000	O_3	ambient	100
9.09	100-000	HO_2	ambient	100
9.60	001-000	O_3	ambient	120
?	1-0	NdO^+	fission fragment	130 < h < 275*
10.3**	1-0	ZrO^+	fission fragment	130 < h < 275*
?	1-0	SmO^+	fission fragment	130 < h < 275*
10.4	001-100	CO_2	ambient	130
11.21	001-000	HO_2^+	bomb material	120 < h < 450*
11.38	ν_5	HNO_3	ambient	60
11.6**	1-0	CeO^+	fission fragment	130 < h < 275*
11.8*	1-0	UO^+	bomb material	120 < h < 450*
11.8**	1-0	YO^+	fission fragment	130 < h < 275*

* Very tentative

** Based on fundamental of the neutral oxide

Table 2-1 (continued). Some LWIR bands and radiators of potential importance in a nuclear environment.

Band Center (μm)	Transition	Species	Species Type	Altitude (h) (km)
12.0	100-000	UO_2^+	bomb material	$120 \leq h \leq 450$*
12.2**	1-0	PrO^+	fission fragment	$130 \leq h \leq 275$*
12.4	1-0	LaO^+	fission fragment	$130 \leq h \leq 275$*
13.1	N out of plane	HNO_3	ambient	≤ 60
13.3	010-000	NO_2	ambient	≤ 125
14.2	010-000	O_3	ambient	≤ 100
15.0	010-000	CO_2	ambient	≤ 120
15.5	NO_2 valence bend	HNO_3	ambient	≤ 60
17.0	010-000	N_2O,	ambient	≤ 170*
17.3	ONO bend	HNO_3	ambient	≤ 60
≥ 18	rotational	H_2O	ambient	≤ 100

* Very tentative

** Based on fundamental of the neutral oxide

be considerably less than the upper limits shown in Table 2-1. Other potential LWIR emitters in a nuclear environment, such as vaporized rocket fuel, have been omitted from consideration here due to a lack of time.

AMBIENT LIMB WINDOWS

In this report, limb windows are defined as wavelength regions over which the earth's limb radiance is less than 10^{-10} or 10^{-9} watts cm^{-2} $ster^{-1}$ μm^{-1}. Results will be presented for each of these two thresholds. Figures 2-1 and 2-2 are graphical estimates of the limb-window regions in the ambient atmosphere under night and day conditions, respectively, for a radiance threshold of 10^{-10} and for altitudes between 60 and 200 km. The ordinate in these figures is the tangent altitude, or distance of closest approach to the earth's surface, of the viewing sight path. The abscissa is the wavelength of the earth-limb radiation. The cross-hatched areas are altitude-wavelength regions for which the limb radiance exceeds 10^{-10} watts cm^{-2} $ster^{-1}$ μm^{-1}. All non-hatched areas are window regions. Thus, for example, the figures show that at an altitude of 65 km the limb radiance exceeds 10^{-10}, both day and night, for all wavelengths from 2.5 μm to at least 25 μm. That is, no window region exists at that altitude. On the other hand, for an altitude of 140 km at night, the only wavelength regions that are not windows occur in a narrow band near 4.3 μm (due to CO_2 emission), a band from 5 to 6 μm (due mainly to NO emission), and one from about 14.3 to 15.6 μm (due to CO_2 emission). Figures 2-3 and 2-4 are corresponding representations of the window regions for a limb-threshold radiance of 10^{-9}.

Figures 2-1 to 2-4 are essentially "low resolution" representations of the window regions. This is especially true of the wavelength region beyond about 19 μm where the emission arises mainly from rotational lines of water vapor and where narrow windows actually exist between the lines but are not shown in our figures. However, since any system operating in
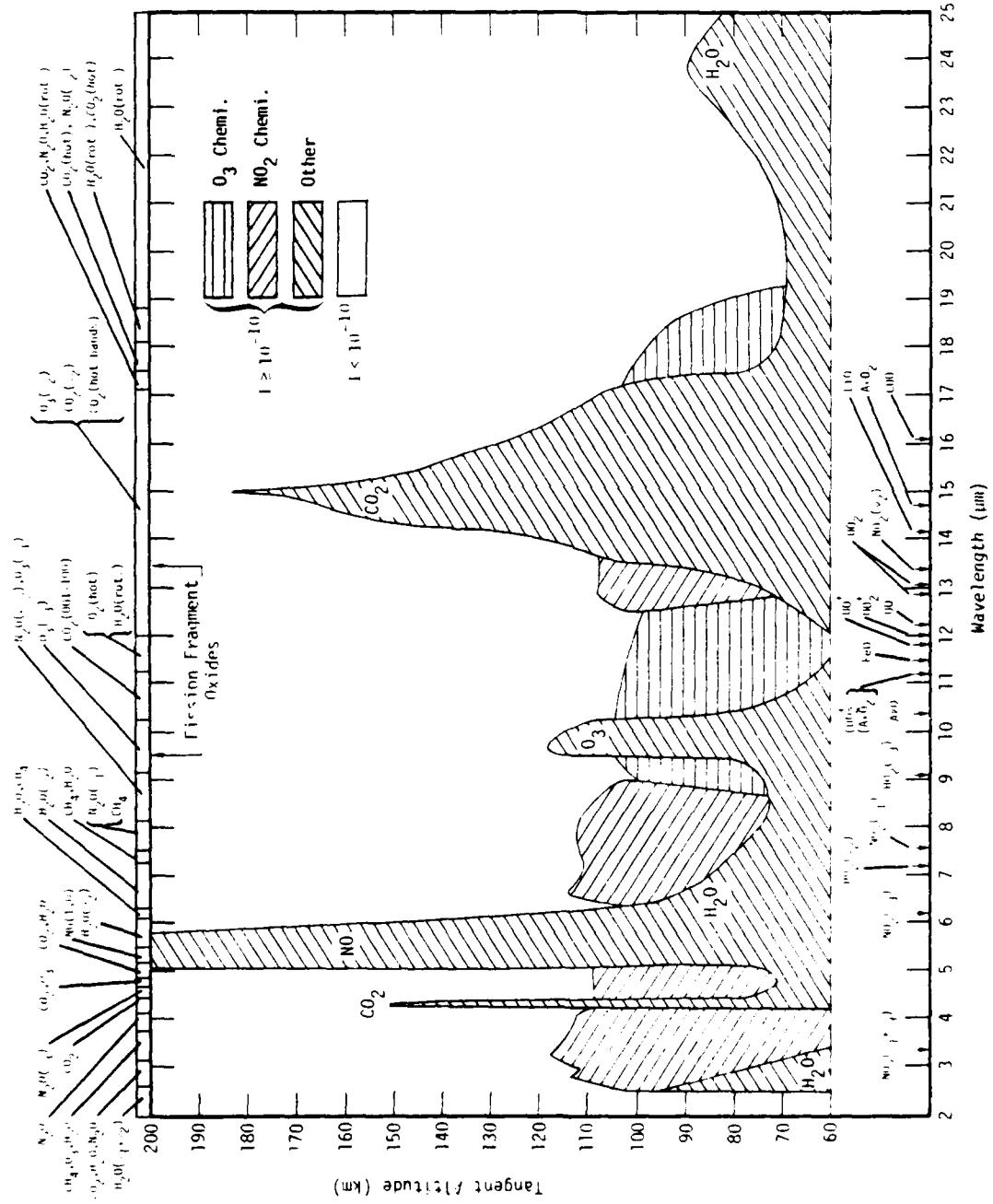
Figure 2-1. Window regions (clear) for limb-viewing geometry where ambient background radiance $\leq 10^{-10}$ watts cm^{-2} $ster^{-1}$ μm^{-1} at night.
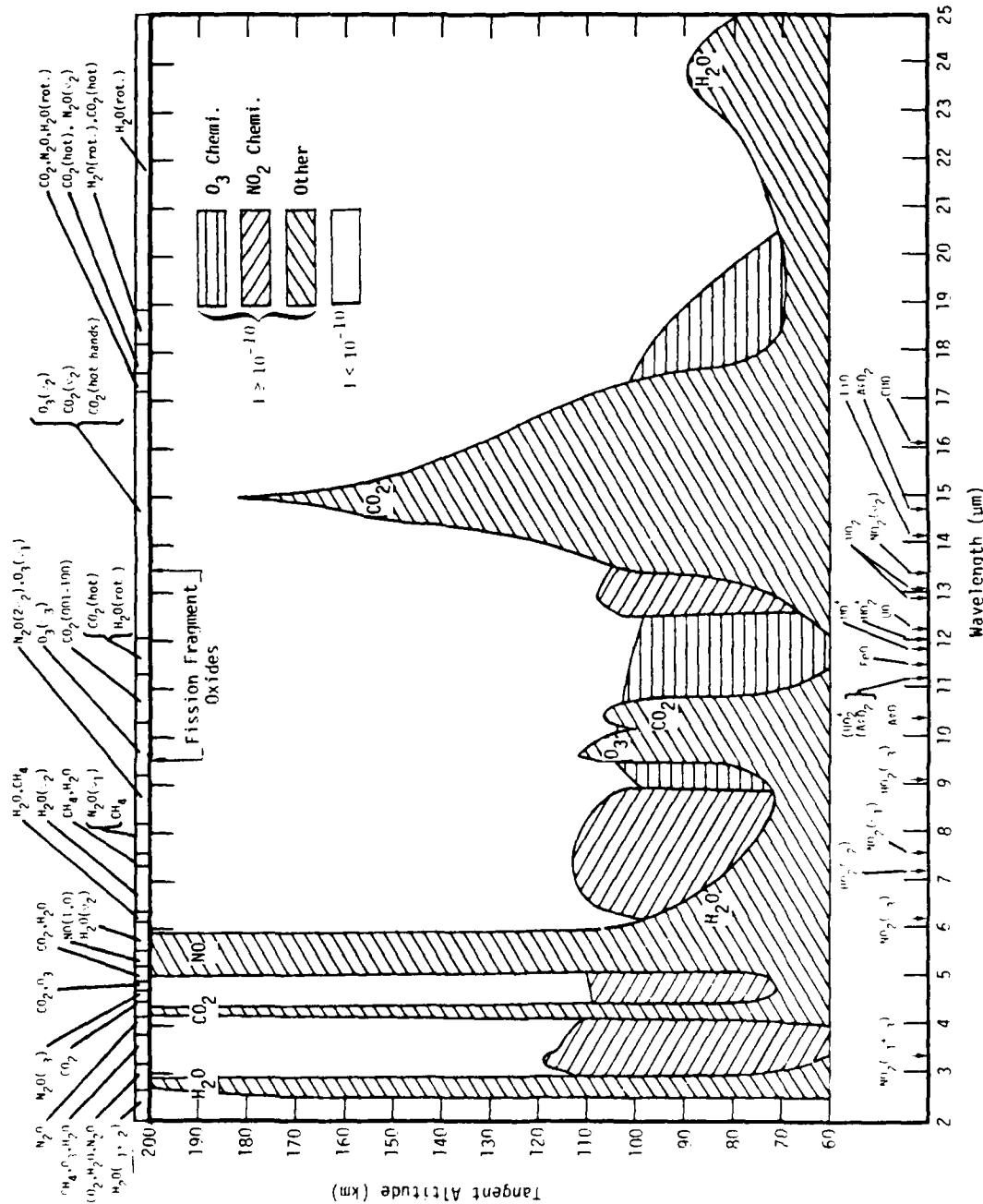
Figure 2-2. Window regions (clear) for limb-viewing geometry where ambient background radiance $\leq 10^{-10}$ watts cm^{-2} ster^{-1} μm^{-1} in day.

17
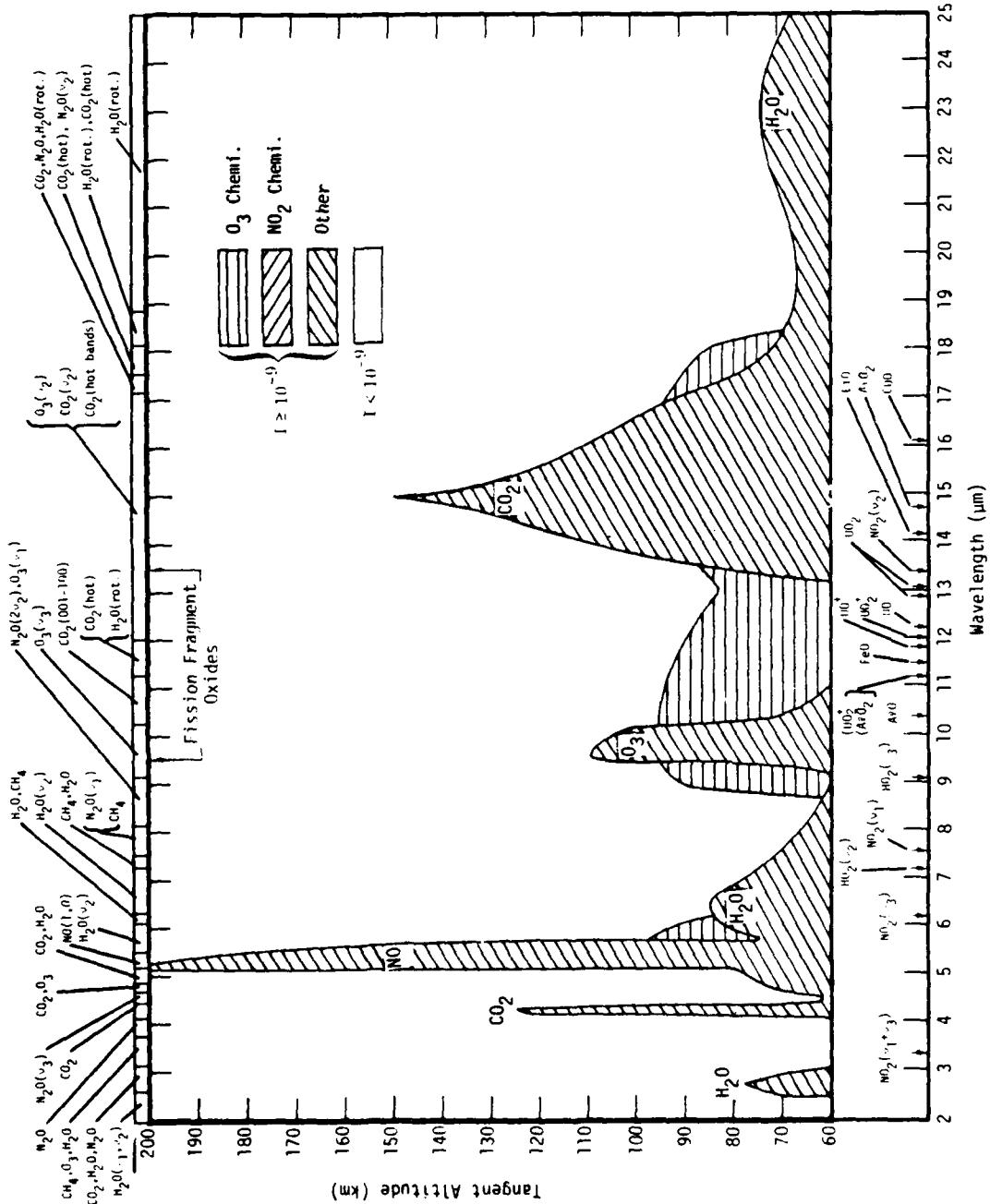
Figure 2-3. Window regions (clear) for limb-viewing geometry where ambient background radiance $\leq 10^{-9}$ watts cm^{-2} $ster^{-1}$ μm^{-1} at night.
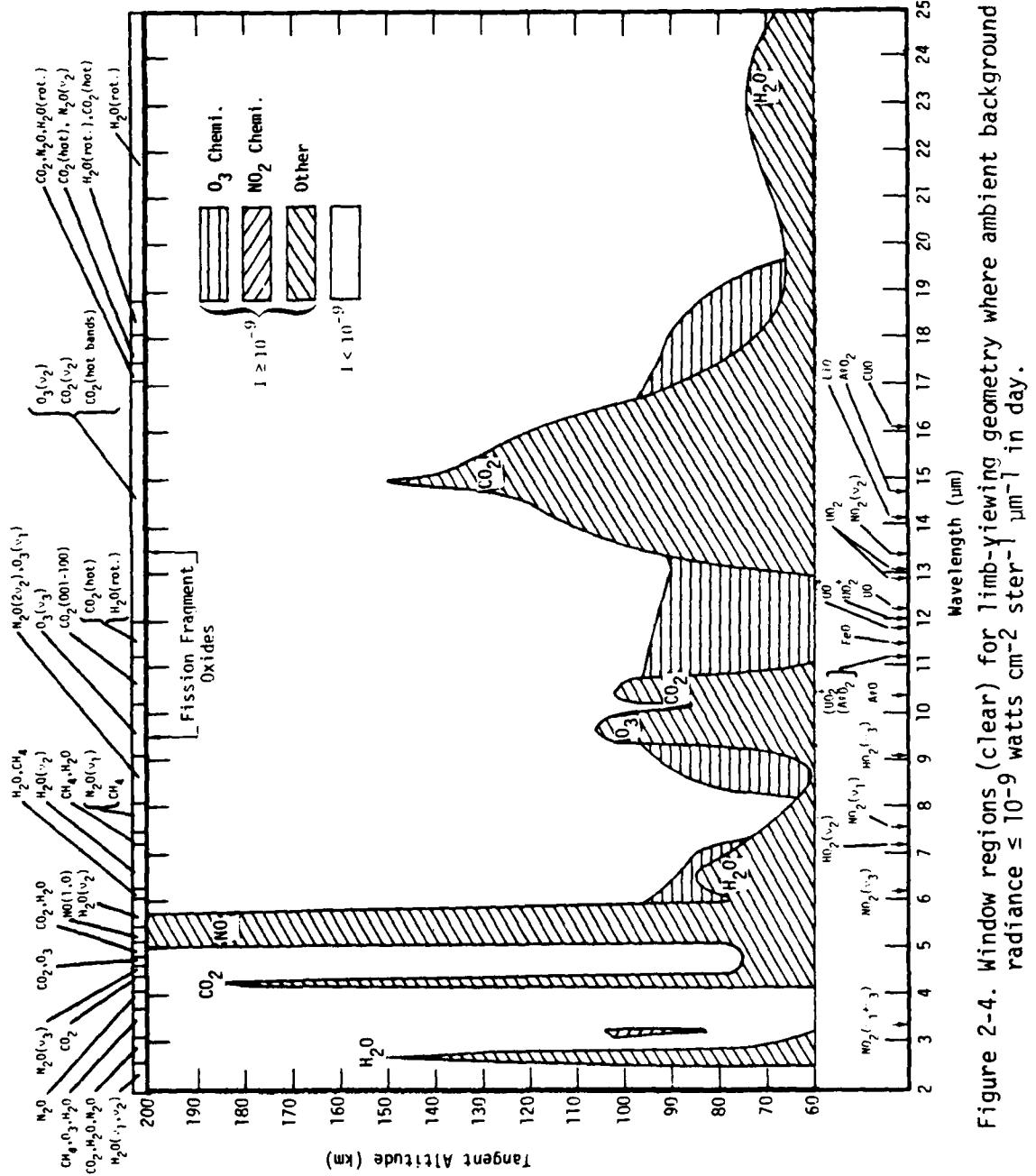
Figure 2-4. Window regions (clear) for limb-viewing geometry where ambient background radiance ≤ 10^{-9} watts cm^{-2} ster^{-1} μm^{-1} in day.

that spectral region is likely to be rather broad band, so as to maximize the detected signal, the existence of these narrow windows is not important for our purpose.

The bases for Figures 2-1 through 2-4 are the following: (1) the Degges high-altitude infrared-radiance model for 1974 (Reference 2-1) and for 1977 (Reference 2-2), (2) earth-limb data from the SPIRE experiment (References 2-3, 2-4) and, (3) calculations by us of the ambient limb radiance from O_3 and NO_2 chemiluminesence. The model by Degges includes the species CO_2, H_2O, NO, and O_3 and assumes excitation by photon scatter as well as by thermal collisions. Other nonthermal excitation processes, such as chemiluminescence, are not included. The 1977 model (Reference 2-2) was utilized except for the case of water vapor where the 1974 model results were employed. The 1977 model assumes an H_2O profile above 100 km that is believed to be too large. SPIRE data was used mainly to modify the CO_2 and O_3 peaks calculated by Degges.

The O_3 and NO_2 chemiluminescence models are described in Appendices A and B, respectively. The calculated effect they have in filling window regions is indicated in Figures 2-1 through 2-4.* The combined effect is particularly significant for the wavelength regions 6.5 to 9.5 μm, 10.5 to 13.5 μm and 17 to 19 μm, with the result that there is effectively no 10^{-10} limb window in the ambient atmosphere below 100-km altitude over the wavelength region from 2.5 to about 18 μm.

We should emphasize that these results (Figures 2-1 to 2-4) are estimates for which there are as yet only limited field data to substantiate them. Nevertheless, we feel that they are sufficiently good to provide a framework within which to judge the relative importance of the different

---

* For computing the ambient chemiluminescent emissions, the O_3 and M concentrations were obtained from the 1972 CIRA Mean Atmosphere (Reference 2-5), the day and night O concentrations from Reference 2-6, and the day and night NO concentrations from Reference 2-2.

LWIR emitting species and mechanisms in a nuclear environment and to permit
a determination of the areas of major uncertainty in our prediction capability.
In later sections of this report, our estimates of the nuclear-induced emissions
will be overlaid on these ambient results so as to determine the extent to
which the ambient windows are filled in.

Indicated near the top of Figures 2-1 through 2-4 are the principal
species responsible for radiation in the various spectral regions under
thermal excitation conditions in the ambient atmosphere. These have been
determined largely from Reference 2-7. Also shown at the top of the figures
is the approximate spectral region over which the fundamentals of the fission-
fragment oxides should occur in a nuclear environment. Near the bottom of
each figure is shown the positions of the band centers for other species that
may be formed, or excited to radiate, in a nuclear environment including
NO_2, HO_2, and certain metal oxides. However, the oxides of some of the
metals shown, especially Li, Aℓ, Cu, and Fe are presently believed to be
formed (by a high-altitude burst) in concentrations too low to present a
problem to systems.

SECTION 3
LIMB RADIANCE IN NUCLEAR ENVIRONMENT

As we have seen in the previous section, there is essentially no 10^{-10} limb window below 100 km in the ambient atmosphere at IR wavelengths out to about 18 μm. Consequently, it seems unlikely that LWIR systems would operate in the limb mode at altitudes below 100 km. We are interested, therefore, in determining how window regions at altitudes above 100 km may be adversely effected by a nuclear environment.

Although bursts at altitudes below 100 km can rise and perturb the atmosphere above 100 km, the greatest potential for large scale excitation of IR radiation above 100 km occurs for large-yield bursts at altitudes considerably above 100 km. For this reason we have concentrated our efforts on megaton-class high-altitude bursts. Specifically, we have utilized results of prior MHD/chemistry code calculations, performed at MRC for such bursts, to determine the limb radiance based on models of emission that reflect our current understanding of the species and radiation mechanisms. Treated here in some detail are the species O_3, NO_2, N_2O, CO_2 and metal oxides, as well as radiation by free electrons in the high-altitude fireball plume. We now consider separately each of the foregoing species.

OZONE (O_3)

Role in Nuclear Environment

With its three fundamentals in the LWIR region, as well as some weaker intercombination bands, ozone is an important minor constituent of

the ambient atmosphere, at least at altitudes below 100 km. Its concentration above about 90 km, however, decreases rapidly with increasing altitude due to the large rate $(10^{-2}$ molecule^{-1} sec$^{-1})$ of solar photodissociation by day and its slow three-body reformation rate at night. Thus, excitation of its bands, even the strong ν_3 band (9.6 μm), by thermal collisions and photon scatter cannot produce significant limb radiance at altitudes much above about 110 km (see previous section, Figures 2-1 through 2-4).

As detailed in Appendix A, and illustrated in Section 2, however, chemiluminescent excitation of O_3 by the reaction

$$O + O_2 + M \longrightarrow O_3 + M \qquad\qquad (3-1)$$

serves to excite the higher-lying vibrational states of O_3 and to thus broaden the thermal spectral bands and narrow the window regions. But, as seen from Figures 2-1 through 2-4, the ozone contribution to the ambient limb radiance is effective mainly at altitudes below about 100 km.

In a nuclear environment there is the potential for raising the ozone limb by upward heave of the atmosphere following a high-altitude detonation. We have investigated the magnitude of this effect for a single megaton-class, high-altitude burst by utilizing previous MHD/chemistry code runs, and incorporating the spectral efficiency for ozone chemiluminescence as described in Appendix A. Figures 3-1 and 3-2 show the maximum perturbation. which occurs under nighttime conditions. These figures are representations of the 10^{-10} and 10^{-9} window regions, respectively, and include the effect of the ambient radiance (compare Figures 2-1 and 2-3) as well as burst-induced O_3 chemiluminescence. As can be seen from Figure 3-1, the burst serves to modify the 10^{-10} window region near 19.5 μm, but only over a small wavelength interval, and only at altitudes below about 90 km. The effect on the 10^{-9} window regions (Figure 3-2) is seen to be somewhat greater by raising the limb altitude in the wavelength intervals 6 to 7 μm, 8 to 13.5 μm,

23
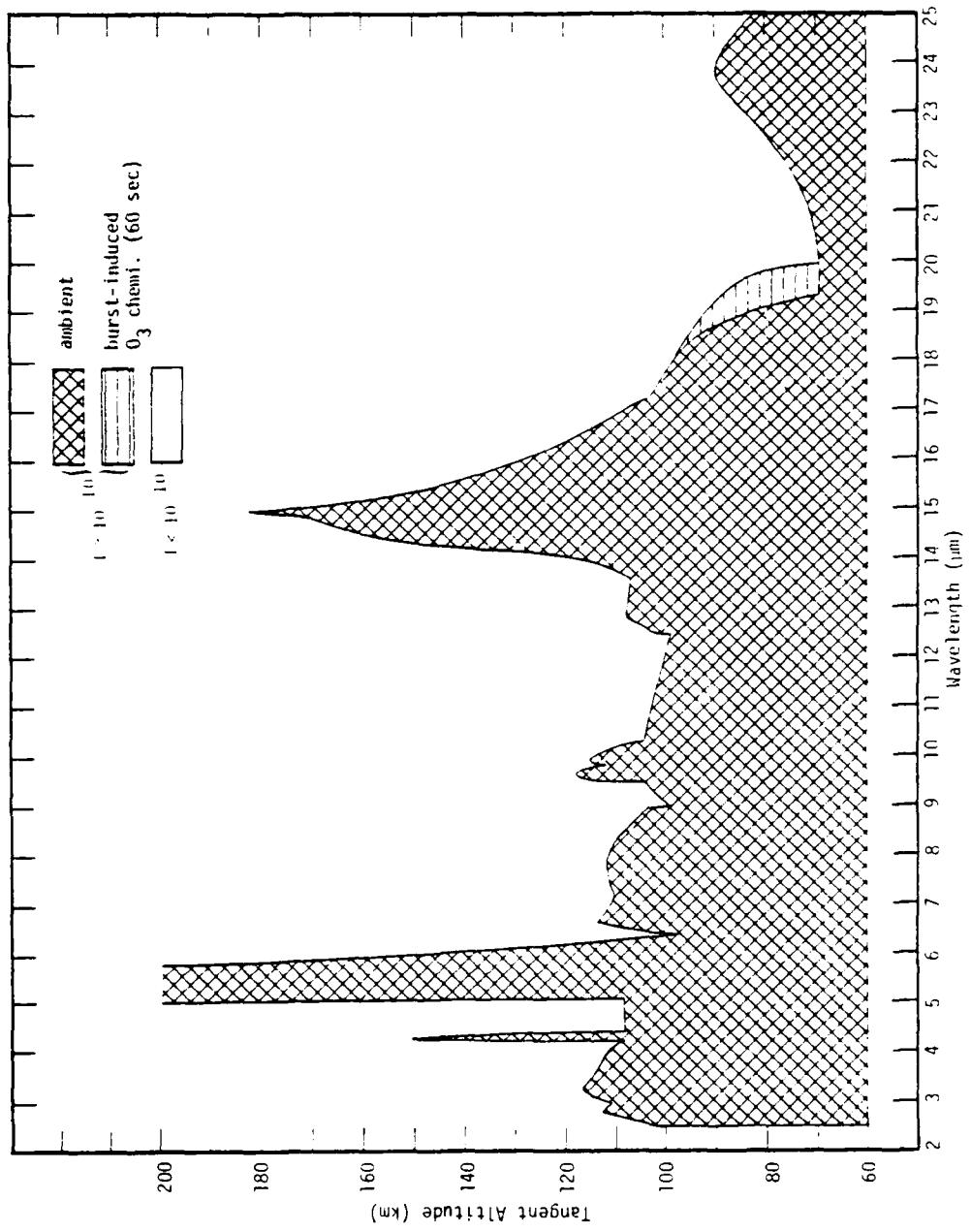
Figure 3-1. Effect on ambient nighttime limb-window radiance (10^{-10} watts cm^{-2} ster^{-1} μm^{-1}) of ozone chemiluminescence induced by megaton-class high-altitude burst at 60 sec.
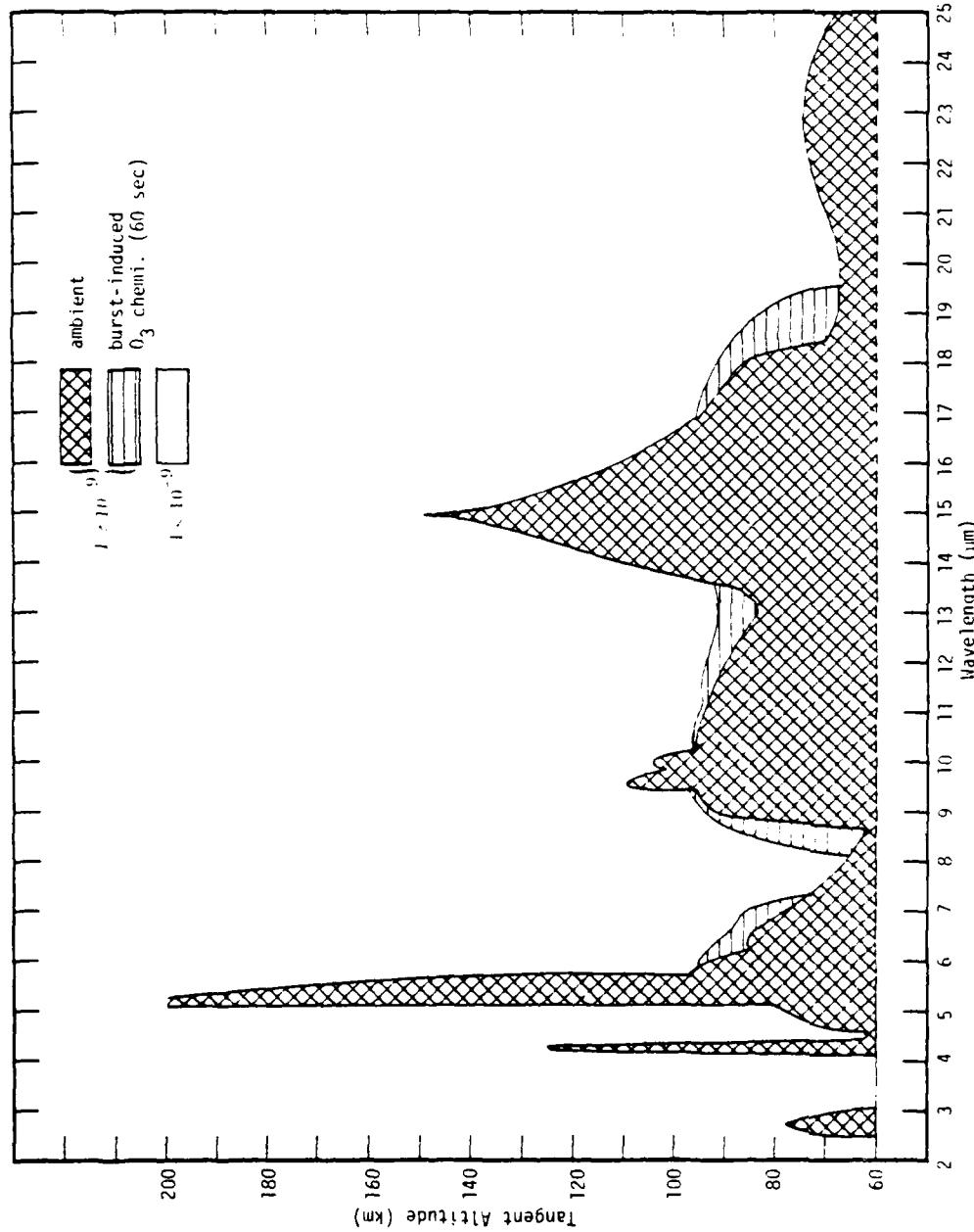
Figure 3-2. Effect on ambient nighttime limb-window radiance (10^{-9} watts cm^{-2} $ster^{-1}$ μm^{-1}) of ozone chemiluminescence induced by megaton-class high-altitude burst at 60 sec.

and 17 to 19.5 μm. However, in each of these regions, the limb is raised to altitudes below 100 km. For daytime conditions, modification of the ambient window regions (Figures 2-2 and 2-4), due to burst-induced O_3 chemiluminescence, is entirely negligible.

The conclusion then is that a single high-yield, high-altitude burst should do little to enhance the LWIR radiation from ozone, over and above the contribution due to O_3 chemiluminescence in the ambient atmosphere. The effect on LWIR systems operating at altitudes above 100 km should be negligible. It is, of course, conceivable that more severe effects from ozone may occur in a multiburst environment, but this has yet to be demonstrated.

Uncertainties

The principal uncertainties involved in predicting the chemiluminescent emission from ozone in a nuclear environment are: (1) the spectral yield of photons per reaction from Reaction 3-1, (2) the species concentrations involved in Reaction 3-1, and (3) the bomb phenomenology relating to energy deposition and subsequent motion of the perturbed atmosphere. However, if burst-induced ozone chemiluminescence were to raise the earth limb to altitudes above 110 to 120 km, as would probably be necessary for there to be any systems impact, the implication would be that our calculated intensities are low by as much as two orders of magnitude. It is very unlikely that uncertainties (1) and (2) above can lead to such large errors in the computed intensity. The photon efficiency, as described in Appendix A, is based on energy conservation and on certain laboratory data, albeit incomplete at this time. Likewise, the chemistry contained in the code computations of species concentrations is based largely on measured rate coefficients. Uncertainty (3), however, related to bomb phenomenology, cannot be ruled out as a possible source of substantial error.

Recommendations

No experimental work on ozone is recommended at this time beyond the efforts already underway. However, multiburst calculations should probably be done to establish whether or not ozone emission is ever important in the LWIR at altitudes above about 120 km. If the results are positive, further field and/or laboratory work might be in order to refine the chemiluminescent yield and spectral distribution.

NITROGEN DIOXIDE (NO_2)

Role in Nuclear Environment

Nitrogen dioxide, with its ν_1, ν_2, and ν_3 fundamentals at 7.6, 13.3, and 6.2 µm, respectively, is a very minor constituent of the ambient atmosphere, having a mixing ratio of only about 10^{-8} in and below the D region, and probably less at higher altitudes due to its rapid rate $(5 \times 10^{-3}$ molecule^{-1} sec$^{-1})$ of photodissociation by day. Thus, thermal and photon scatter excitation of the species results in negligible emission in the ambient atmosphere, especially above 100-km altitude. The potential importance of the species in a nuclear environment, however, lies in the possibility of chemiluminescent excitation of its bands, particularly through the reactions

$$NO + O(+M) \longrightarrow NO_2(+M) + 3.12 \text{ eV} \qquad (3-2)$$

$$NO + O_3 \longrightarrow NO_2 + O_2 + 2.07 \text{ eV} \qquad (3-3)$$
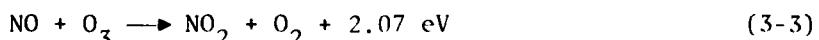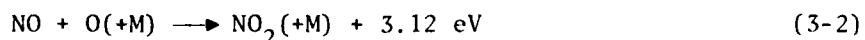
where the concentration of the reactant NO may be considerably enhanced. Reactions 3-2 and 3-3 are sufficiently exothermic to permit the population of high vibrational states of the fundamental and intercombination bands of NO_2 and to broaden the spectrum considerably beyond that due to thermal excitation alone. The assumed spectral distribution arising from NO_2 chemiluminescence is described in Appendix B and includes contributions from nine intercombination bands as well as the three fundamentals.

27

This spectral distribution has been incorporated with results from prior MHD/chemistry code calculations at MRC for the case of a megaton-class, high-altitude burst to obtain the limb radiance as a function of tangent altitude and wavelength at a time of 60 sec after burst. The results, for the cases of 10^{-10} and 10^{-9} limb-threshold radiances at night, are shown in Figures 3-3 and 3-4, respectively, superimposed on the previously-shown results (Figures 2-1 and 2-3) for the ambient atmosphere. We see, for example, that the 10^{-10} limb is raised by about 20 km in the spectral regions 6.5 to 9 μm and 12 to 13.5 μm to peak altitudes of about 130 km and 125 km, respectively. As comparison between Figures 3-1 and 3-3 shows, our estimate of the nuclear-burst enhancement of NO_2 chemiluminescence is considerably greater than that for O_3 chemiluminescence. This is because of the enhanced NO concentration, even at higher altitudes, which serves to increase the rate of NO_2 formation through Reactions 3-2 and 3-3.

The conclusion then is that, to within the uncertainties present in the model adopted, a single high-yield, high-altitude burst can probably raise the earth limb enough to cause potential interference with LWIR systems operating in certain spectral regions, particularly in the 6.5 to 8.5 μm and 12 to 14 μm bands, at tangent altitudes below about 135 km. The severity of the interference will be critically dependent on the degree and nature of any structure that exists within the emitting volume.

Uncertainties

The principal uncertainties involved in predicting the effect of NO_2 chemiluminescence in a nuclear environment are similar in nature to those listed above for ozone chemiluminescence, namely: (1) the spectral yield of photons per reaction from Reactions 3-2 and 3-3, (2) the species concentrations involved in Reactions 3-2 and 3-3, and (3) bomb phenomenology relating to the dynamics of the post-burst environment.
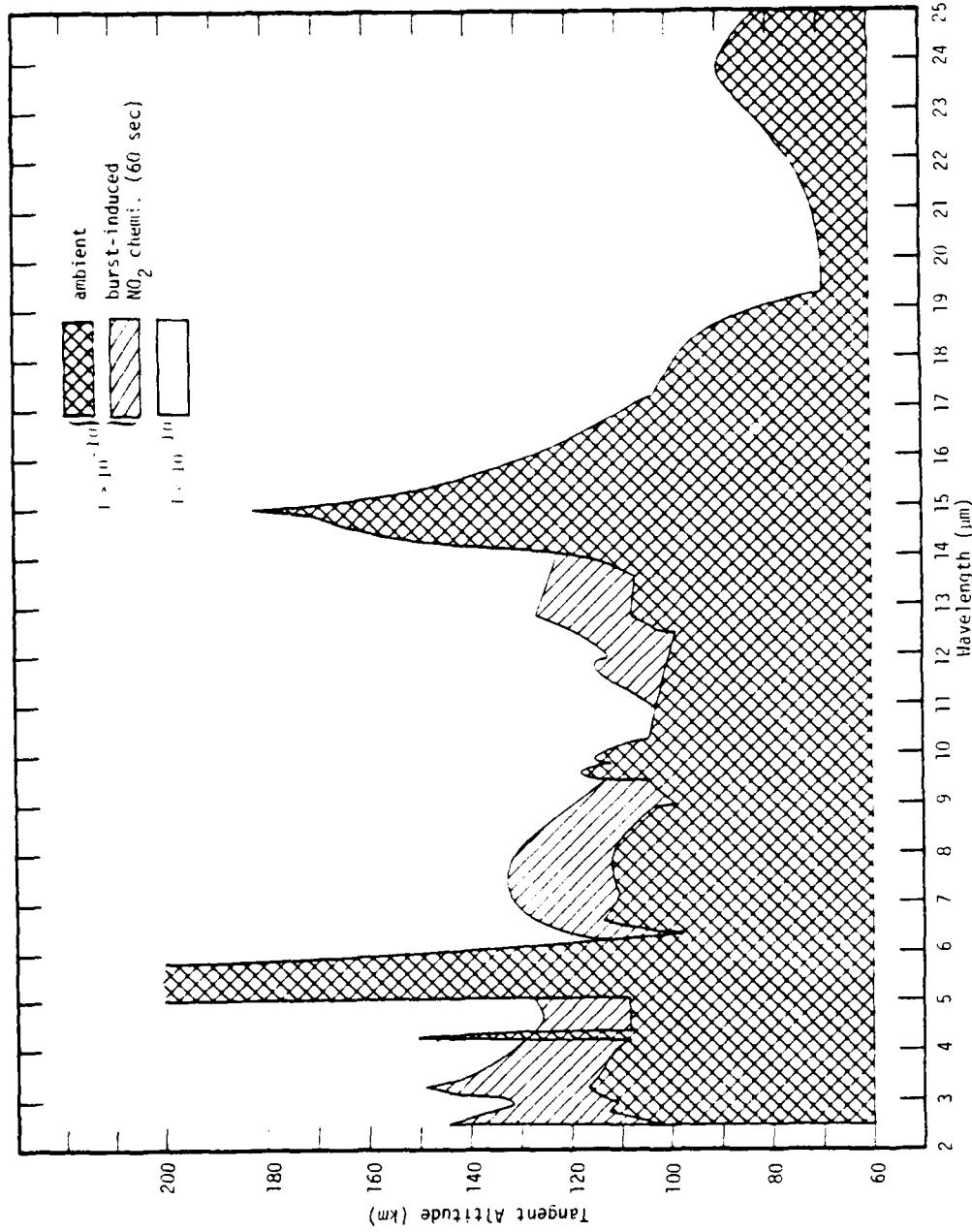
Figure 3-3. Effect on ambient nighttime limb-window radiance (10^{-10} watts cm^{-2} $ster^{-1}$ μm^{-1}) of NO_2 chemiluminescence induced by megaton-class high-altitude burst at 60 sec.
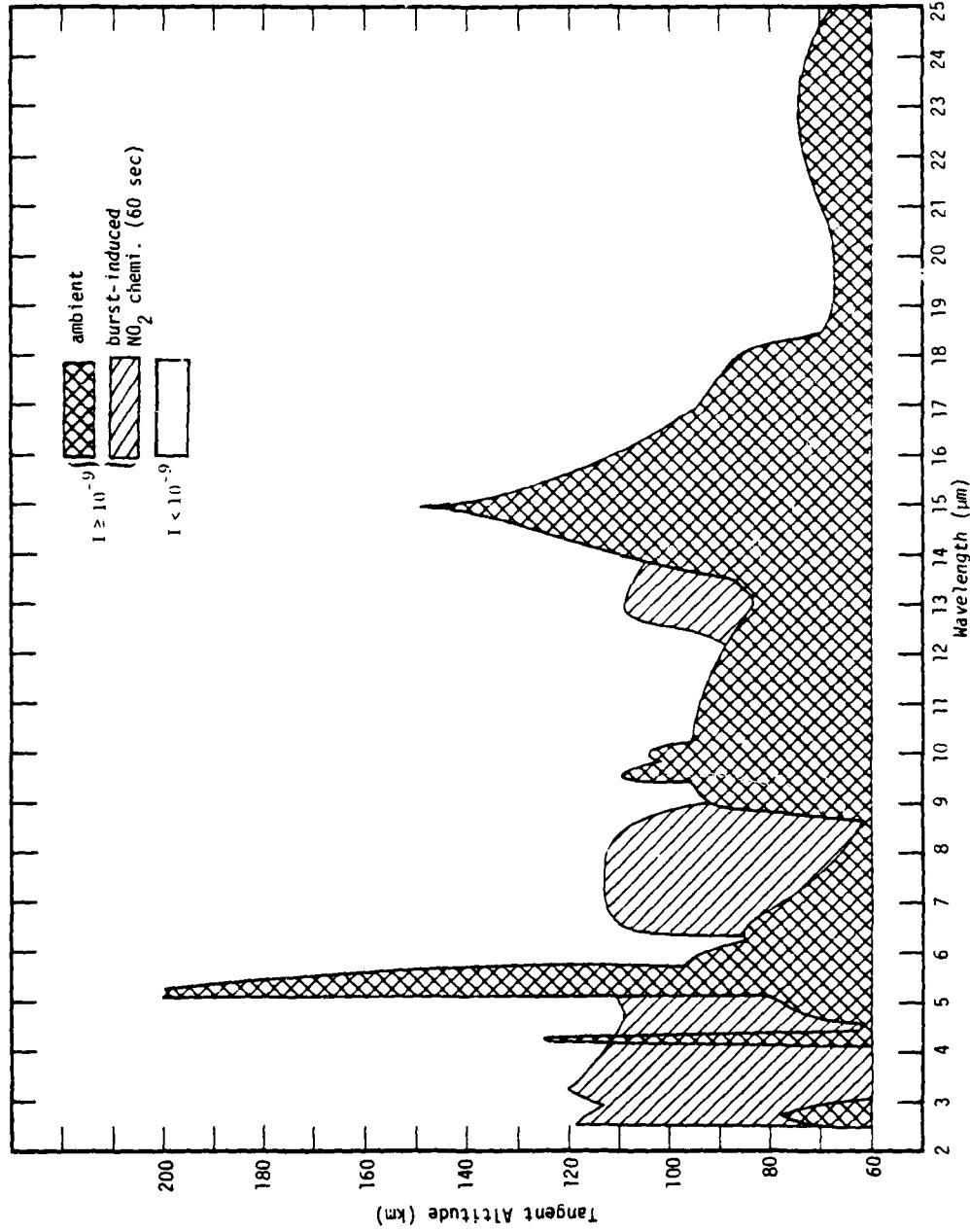
Figure 3-4. Effect on ambient nighttime limb-window radiance (10^{-9} watts cm^{-2} $ster^{-1}$ μm^{-1}) of NO_2 chemiluminescence induced by megaton-class high-altitude burst at 60 sec.

30

The spectral yield of photons in the various LWIR bands of NO_2 from Reactions 3-2 and 3-3 has not been measured. The yield values that we have adopted, as discussed in Appendix B, are those used in the WOE code and are based on the usual assumptions of energy conservation and equal population rates of vibrational states during formation of NO_2. Thus, there is considerable uncertainty regarding the spectral yield, possibly by as much as an order of magnitude at certain wavelengths.

As to the species concentrations involved in Reactions 3-2 and 3-3, perhaps the largest uncertainty (outside of the bomb phenomenology pertaining to atmospheric heave) relates to the NO concentration whose determination is rather sensitively dependent on the relative amounts of $N(^2D)$, $N(^2P)$, and $N(^4S)$ that are formed following a nuclear burst (see, for example, Reference 1-1). Order-of-magnitude uncertainties in the predicted NO concentration are related to relatively small uncertainties in the ratio of metastable to ground-state nitrogen atoms formed both initially and by N_2^+ recombination. Formation rates of NO, $N(^2D)$, and $N(^1S)$ by the reaction $N_2(A^3\Sigma) + O \rightarrow NO + N$ are also very uncertain.

Recommendations

In view of the potential for degradation of LWIR systems from NO_2 chemiluminescence following high altitude detonations, it is recommended that measurements be made to determine:

1. the spectral yield of photons from Reactions 3-2 and 3-3, together with sufficient data to permit a determination of the effect due to quenching.

2. branching ratios for production of $N(^4S)$, $N(^2D)$, and $N(^2P)$ atoms (a) by dissociative recombination in N_2^+ and, (b) immediately following deposition by fast (keV) electrons.

3.   rate constants for production of NO, $N(^2D)$, and $N(^4S)$ by the
reaction $N_2(A^3\Sigma) + O \rightarrow NO + N$.

Recommendations 2 and 3 above were included in the (revised) list of recom-
mendations contained in Reference 1-1.

NITROUS OXIDE (N_2O)

Role in Nuclear Environment

Nitrous oxide, with its ν_1, ν_2, and ν_3 fundamentals at 7.8, 17.0,
and 4.5 μm, respectively, is a very minor constituent of the ambient atmo-
sphere, with a measured mixing ratio that decreases with increasing altitude
from a value of about 3×10^{-7} at 10 km to 1×10^{-7} at 30 km. The potential
importance of the species in a nuclear environment lies in the possible
degradation of LWIR windows by excitation of its ν_1 and ν_2 bands, and of
enhanced background radiation from its ν_3 band which lies in the red-spike
region of the ν_3 fundamental of CO_2. As discussed in Reference 1-1, until
recently the species has not been considered very interesting from the nuclear
IR point of view for several reasons. With a dissociation (+ activation)
energy of just over 2 eV, it is destroyed at relatively low temperatures in
fireballs, and so thermal emission from it is quite low. Outside fireballs,
the principal formation mechanism has been considered to be the reaction

$$N + NO_2 \longrightarrow N_2O + O \qquad\qquad (3-4)$$

where the NO_2 is formed mainly from reaction of NO with odd oxygen. However,
by the time NO_2 has formed, most of the nitrogen atoms have been consumed
to form NO by reaction with the much more abundant O_2.

Recently, however, it has been found (Reference 3-1) that N_2O is
formed quite efficiently by the reaction

$$N_2(A^3\Sigma) + O_2 \longrightarrow N_2O + O + 2.73 \text{ eV} \qquad\qquad (3-5)$$
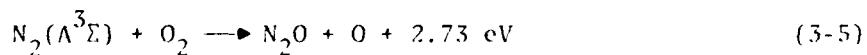
involving the first metastable state of N_2. Since $N_2(A^3\Sigma)$ has a lifetime against radiation of about 2 sec, and since it is believed to be formed copiously (up to about one molecule per ion pair) in a nuclear environment, Reaction 3-5 would appear to provide a mechanism for N_2O formation, even at high altitudes, at least where the O_2 is not dissociated. Further evidence of this possibility comes from LABCEDE experiments (Reference 3-2) in which IR radiation from N_2O was detected following electron bombardment of air at moderately high pressures. These data could not be accounted for on the basis of Reaction 3-4, but were found to be more consistent with N_2O formation by Reaction 3-5.

In Reference 1-1, we implied that since the lifetime of $N_2(A)$ is only about 2 sec, Reaction 3-5 can be significant for N_2O radiation only in regions where there exists a continuing production source for $N_2(A)$. This statement is true for N_2O chemiluminescence, but it ignores the possibility of continuing excitation of the N_2O, formed in Reaction 3-5, by photon scatter. We have investigated the magnitude of this effect for the case of a single megaton-class high-altitude burst, using results of MHD code calculations of the initial electron density distribution, to estimate the volume production of $N_2(A)$ molecules. In so doing, it was assumed that one $N_2(A)$ molecule is formed per initial ion pair, a value that is within a factor of about 3 of most estimates to date. Estimates of the N_2O concentration were then made by assuming that $N_2(A)$ is quenched mainly by reaction with O_2 and O and by radiation of the Vegard-Kaplan bands.* Thus, given the reaction set:

$$N_2(A^3\Sigma) + O_2 \xrightarrow{k_1} N_2O + O \qquad (3\text{-}5)$$

$$N_2(A^3\Sigma) + O_2 \xrightarrow{k_2} \text{other products} \qquad (3\text{-}6)$$

$$N_2(A^3\Sigma) + O \xrightarrow{k_3} \text{products} \qquad (3\text{-}7)$$

$$N_2(A^3\Sigma) \xrightarrow{A} N_2 + h\nu(\text{V-K bands}), \qquad (3\text{-}8)$$

---
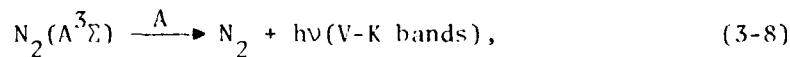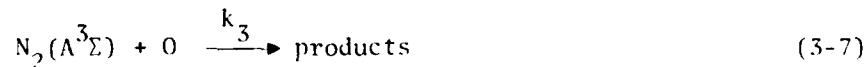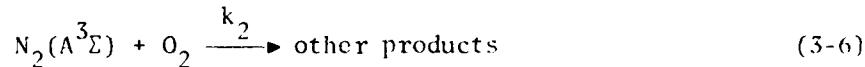
* The quenching of $N_2(A)$ by NO and N can also be significant in regions where the concentration of those species is comparable to that for atomic oxygen.

where A is the Einstein transition rate for the $A^3\Sigma \to X^1\Sigma$ transition in N_2, the concentration of N_2O, relative to $N_2(A^3\Sigma)$, is easily shown to be

$$\frac{[N_2O]}{[N_2(A)]} = \frac{k_1[O_2]}{(k_1+k_2)[O_2] + k_3[O] + A} \left\{ 1 - e^{-[(k_1+k_2)[O_2] + k_3[O] + A]t} \right\} ,$$

(3-9)

where k_1, k_2, and k_3 are rate coefficients for Reactions 3-5, 3-6, and 3-7, respectively. The maximum value for this ratio is, therefore,

$$\left\{ \frac{[N_2O]}{[N_2(A)]} \right\}_{max} = \frac{k_1[O_2]}{(k_1+k_2)[O_2] + k_3[O] + A} .$$

(3-10)

The earth-limb spectral intensity, I_ν, for an N_2O column density N molecules cm^{-2}, excited by photon scatter, is

$$I_\nu = \frac{h\nu}{4\pi} f_\nu N \qquad (ergs\ cm^{-2}\ sec^{-1}\ ster^{-1} (cm^{-1})^{-1})$$

(3-11)

where $h\nu$ is the photon energy (ergs) and f_ν is the number of photons emitted per molecule per sec per wavenumber. In other units, the result is

$$I_{\lambda_\mu} = 1.58 \times 10^{-20} (f_{\lambda_\mu}/\lambda_\mu)N \qquad (watts\ cm^{-2}\ ster^{-1}\ \mu m^{-1}) \quad (3-12)$$

where λ_μ is the wavelength in micrometers, and f_{λ_μ} is the number of photons emitted per molecule per sec per micrometer.

The limb intensity for each of the three fundamentals of N_2O has been determined from Equation 3-12 using values for f_{λ_μ} computed for earthshine scatter, described in Appendix C, and values of N, based on Equation 3-10, determined from the MHD-code results of electron density ($\equiv [N_2(A)]$) at a time of 3 sec. In performing these calculations, the values for $[N_2(A)]$ were assumed equal to the electron density, except in O_2-dissociated regions where they were taken to be zero. Three separate estimates of the N_2O concentration were made corresponding to different

values for the rate coefficients k_1, k_2, k_3, and the common value $A = 0.5$ sec^{-1} (Reference 2-6). The first estimate was an attempt to see if N_2O emission might be important, by using the values $k_1 = 1 \times 10^{-11}$, $k_2 = k_3 = 0$, which should lead to upper limits on the N_2O concentration. The results, for the cases of 10^{-10} and 10^{-9} limb-threshold radiances at night, are shown in Figures 3-5 and 3-6, respectively, superimposed on the previously-shown results (Figures 2-1 and 2-3) for the ambient atmosphere. The effect is seen to be quite dramatic, particularly on the 10^{-10} window regions (Figure 3-5) near 4.5 µm, and from about 7.4 to 8.4 µm and 16 to 18 µm where the limb is raised to altitudes above 180 km. However, these results are probably unrealistically high because the value used for k_1 is larger than any quoted recently and because the quenching of $N_2(A^3\Sigma)$ by atomic oxygen (rate coefficient k_3) has been neglected. Values of k_3 ranging from 2×10^{-11} to 1.3×10^{-10}, with a mean value of 7.5×10^{-11} cm^3 sec^{-1}, have been inferred from auroral measurements (Reference 3-3). Using this mean value for k_3, together with the values $k_1 = 1 \times 10^{-12}$, $k_2 = 2 \times 10^{-12}$ (References 2-6, 3-4, 3-5)*, we find that Equations 3-10 and 3-12 lead to values for the limb radiance that are $<10^{-10}$ watts cm^{-2} $ster^{-1}$ $µm^{-1}$ at all altitudes. Thus, the ambient window regions shown in Figures 3-5 and 3-6 would be unaffected by the N_2O emission.

As a third estimate, we used the values $k_1 = 2 \times 10^{-12}$, $k_2 = 4 \times 10^{-12}$, and $k_3 = 2 \times 10^{-11}$. These values are still within the uncertainty limits of each of the rate coefficients. The results are shown in Figures 3-5 and 3-6. As expected, the window regions are less severely affected than they are in the upper-limit case where $N_2(A)$ quenching by atomic oxygen is neglected. For the 10^{-10} window regions (Figure 3-5) the limb is raised to about 130 km between 16.5 and 17.5 µm, to about 190 km between 7.6 and

---

* Reference 3-4 gives results for quenching of $N_2(A^3\Sigma)$ in various vibrational states. The value adopted here for $k_1 + k_2$ is an average for the $v = 0$ state of results obtained by different experimenters.
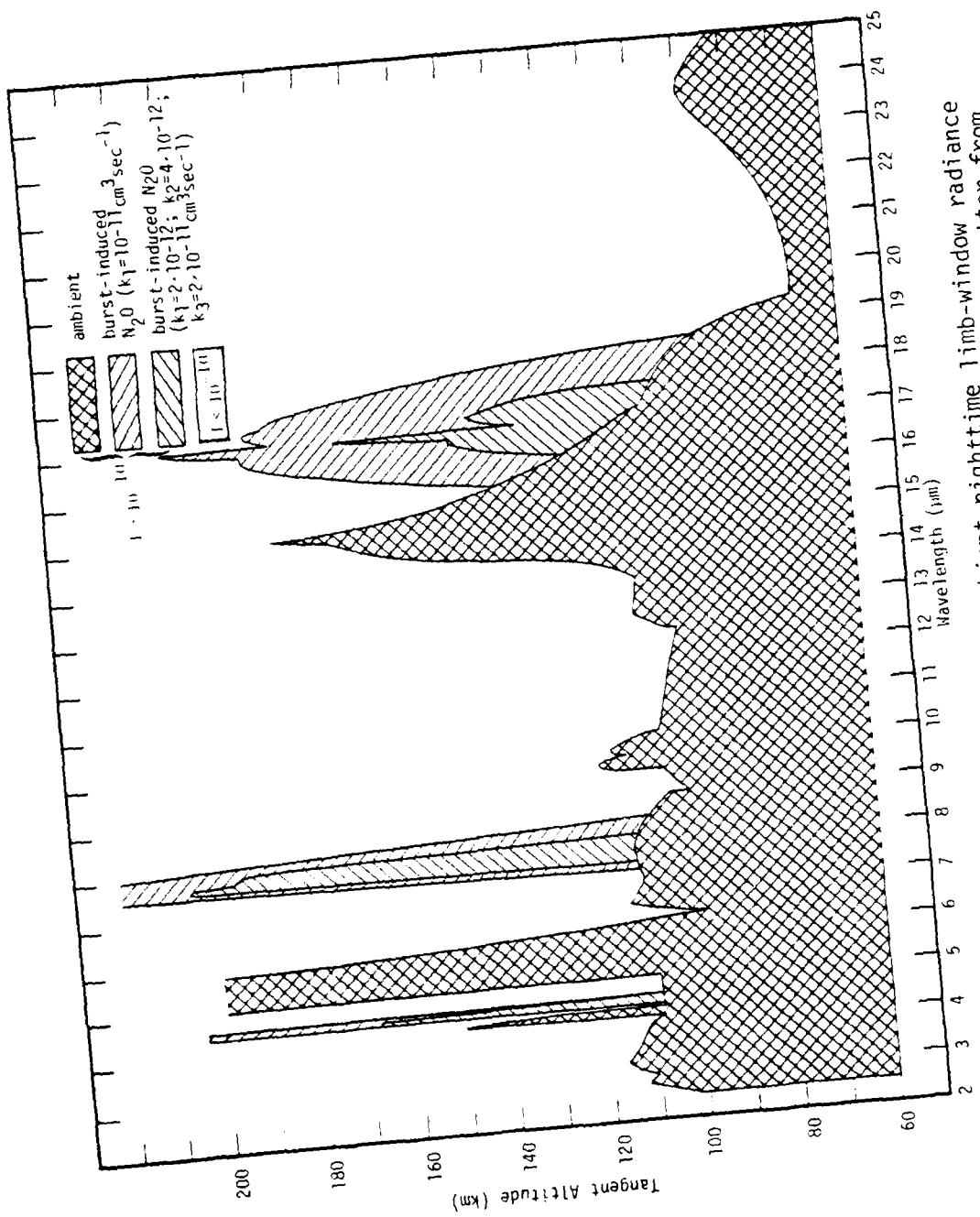
Figure 3-5. Estimated effect on ambient nighttime limb-window radiance from (10^{-10} watts cm^{-2} $ster^{-1}$ μm^{-1}) by earthshine scatter from N_2O formed by megaton-class high-altitude burst at 3 sec.
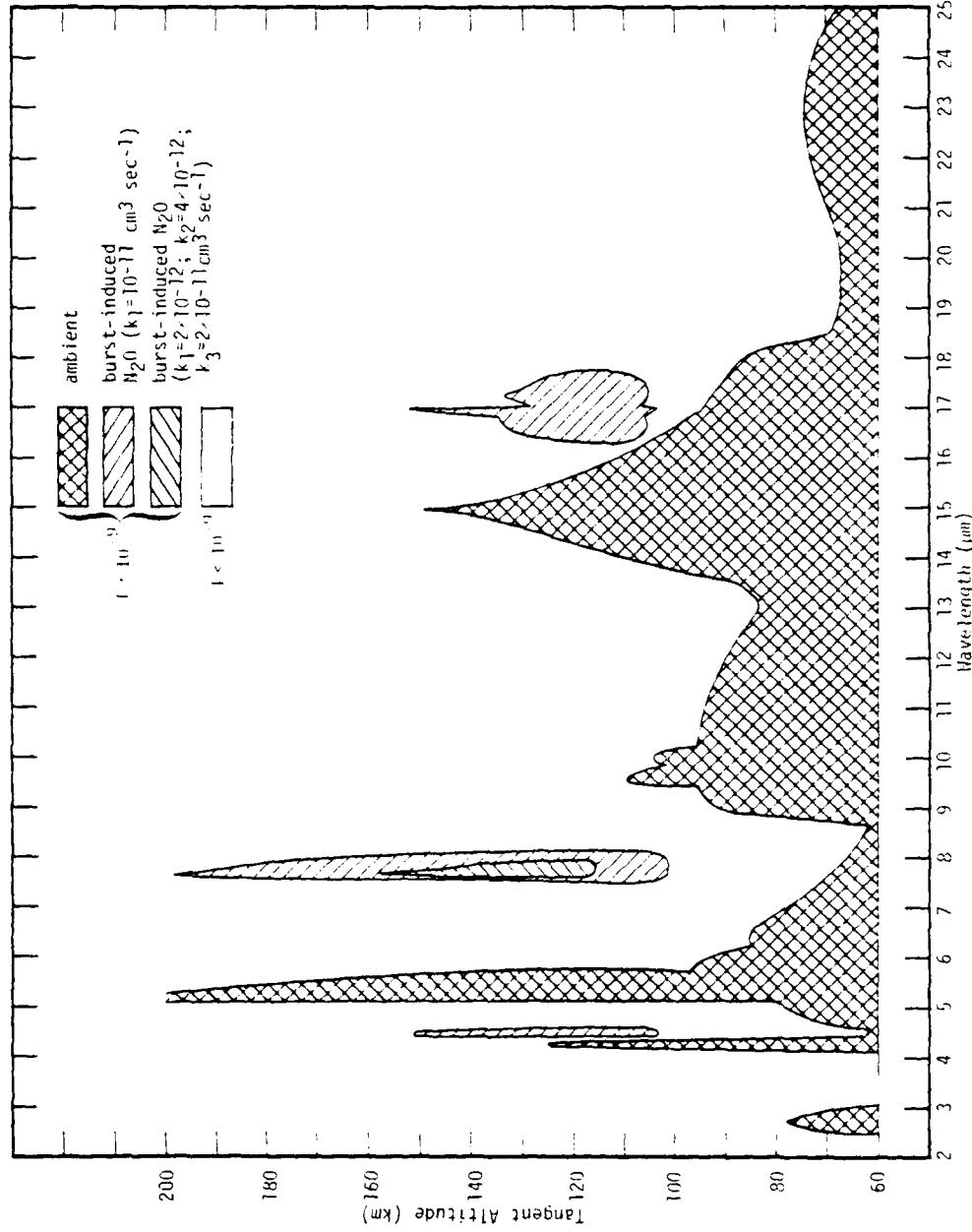
Figure 3-6. Estimated effect on ambient nighttime limb-window radiance (10^{-9} watts cm^{-2} $ster^{-1}$ μm^{-1}) by earthshine scatter from N_2O formed by megaton-class high-altitude burst at 3 sec.

37

7.9 µm, and to about 167 km near 4.5 µm. The 10^{-9} window regions (Figure 3-6) are unaffected by N_2O emission except in a wavelength band near 7.7 µm at altitudes between about 115 and 155 km.

The results shown in Figures 3-5 and 3-6 pertain to a time of 3 sec after burst. Subsequently, there should be some change in them because of the initial upward motion that will tend to heave the N_2O to higher altitudes for at least the first 5 minutes and, later, because of the downward motion as the air falls back under the influence of gravity. Thus, for at least 5 minutes the earth limb may well be raised to altitudes higher than that shown in Figures 3-5 and 3-6. We have not had time to pursue this point. Nevertheless, the results at the early time shown should serve to point up the potential importance of N_2O in a nuclear environment.

The conclusion then is, that to within the considerable uncertainties currently present, a single high-yield, high-altitude burst can possibly produce enough N_2O to cause potential interference with LWIR systems operating in spectral regions near 4.5 µm, 7.6 to 8 µm, and 16.5 to 17.5 µm. The severity of the interference will again be very dependent on the nature and degree of any structure in the emitting volume.

During daylight hours one might expect additional excitation of the N_2O bands by the solar pumping mechanism.* However, N_2O does not absorb in the visible spectral region and most UV absorption appears to result in photodissociation of the molecule (References 3-6 and 3-7) except, possibly in the far UV ($\lambda \leq 1500$Å) where the solar flux is not inte se. It therefore appears that the solar-pumping mechanism is ineffective in exciting the IR bands of N_2O, although a definitive conclusion on this must await a more critical review of the N_2O literature.

---

* This is the process whereby the molecule is first raised to an electronically excited (discrete) state by absorption of a visible/UV photon and then, following radiative cascade, is generally left in a vibrationally excited state of the ground electronic state.

Uncertainties

Apart from uncertainties in the bomb phenomenology relating to the dynamics of the post-burst environment, the principal uncertainties involved in a prediction of the N_2O radiation in a nuclear environment are: (1) the rate constant for quenching $N_2(A^3\Sigma)$ by atomic oxygen, (2) the rate constant for N_2O formation by Reaction 3-5, and (3) the spectral yield of photons arising from photon-scatter excitation of N_2O, especially by sunlight. Of lesser uncertainty is, (4) the number of $N_2(A^3\Sigma)$ molecules formed per initial ion pair.

Probably the fastest collisional quenching of $N_2(A)$ is by atomic oxygen. As mentioned above, measurements on the Vegard-Kaplan bands in the aurora (Reference 3-3) can be accounted for on the basis of a quenching coefficient, k_3, ranging from about 2×10^{-11} to 1.3×10^{-10} cm^3 sec^{-1}. As we have seen, values for k_3 as large as 7.5×10^{-10} appear to produce sufficiently fast quenching of $N_2(A)$ to effectively eliminate N_2O as an important radiator in a nuclear environment. On the other hand, a value of 2×10^{-11} seems to permit sufficient N_2O formation to make it a potential systems threat. Therefore, the degree of importance of N_2O in a nuclear environment depends critically on a better knowledge of the rate coefficient k_3.

In Appendix C we treat the case of excitation of N_2O by earthshine scatter. The basic ingredients involved are the vibrational f numbers for the fundamental bands of N_2O and the spectral flux of earthshine photons, all of which are reasonably well known. As for solar scatter, excitation of N_2O by the UV (or visible light)-pumping mechanism has not been treated in detail, and so at present the rate is very uncertain. However, as mentioned above, the rate is probably small because N_2O does not appear to possess the necessary absorption bands in the visible or UV regions, although this needs to be confirmed.

ome uncertainty exists in the number of $N_2(A^3\Sigma)$ molecules formed per ion pair from electron impact due to uncertainties in the excitation cross sections for formation of the $A^3\Sigma$ state, as well as the $B^3\Pi$, $C^3\Pi$, and $W^3\Delta$ states that lead to the $A^3\Sigma$ state by radiative cascade. However, uncertainties in the individual cross sections appear to be relatively small (± 25 percent) because of recent improvements in experimental techniques (Reference 3-8). As far as we know, no studies have been made to determine the overall uncertainty in the number of $N_2(A^3\Sigma)$ molecules formed following radiative cascade.

Recommendations

To permit a definitive conclusion regarding the possible degradation of both MWIR and LWIR systems in a nuclear environment from N_2O radiation, the following work is recommended:

1. Laboratory measurements to determine the rate coefficient for quenching of $N_2(A^3\Sigma)$ by atomic oxygen.

2. Laboratory measurements to determine, more accurately, the rate coefficient for formation of N_2O by the reaction $N_2(A^3\Sigma) + O_2 \rightarrow N_2O + O$.

3. Calculation of the excitation rate of the N_2O fundamentals by sunlight pumping.

4. Sensitivity calculations to determine the uncertainty in the number of $N_2(A^3\Sigma)$ molecules formed per ion pair, from electron bombardment, by utilizing the best current upper and lower limits on excitation cross sections for the relevant states of of N_2, including $A^3\Sigma$, $B^3\Pi$, $C^3\Pi$, $W^3\Delta$.

CARBON DIOXIDE (CO$_2$)

Role in Nuclear Environment

Carbon dioxide is an important infrared radiator in the ambient atmosphere with its fundamental, intercombination, and hot bands prominent in the SWIR, MWIR, and LWIR regions. For example, its ν_2 fundamental at 15 μm has a measured limb radiance at 100-km altitude of about 5×10^{-7} watts cm^{-2} ster^{-1} μm^{-1} (Reference 3-9). The potential importance of the species in a nuclear environment lies in the fact that N$_2$(v=1), which is initially the sink for about 5 percent of the X-ray energy released from a high-altitude nuclear burst, can readily transfer this energy to CO$_2$ which can then radiate it over a long period of time by the ν_3 fundamental at 4.3 μm and by other bands at longer wavelengths.

In the past few years a lot of effort has gone into modeling this emission, particularly for the ν_3 band, although considerable attention has recently been given to the longer wavelength bands as well. Refinements have been added to the theory to allow for radiation trapping of the 4.26-μm resonance radiation below about 100 km, for emission by the so-called weak isotopic and hot bands, and for fluorescence resulting from absorption by CO$_2$ of sunlight and bomblight at 2.7 μm with subsequent reradiation in other bands, especially those near 4.3 μm (see, for example, References 3-10 to 3-14). The basic theory of CO$_2$ vibraluminescence near 4.3 μm has been substantially verified by the ICECAP auroral measurements.

For our purpose of estimating the relative importance of LWIR vibraluminescence of CO$_2$ in a nuclear environment above 100-km altitude, it is not necessary to invoke all the refinements in theory referred to above, but rather to consider the basic mechanism of vibrational energy transfer from N$_2$ to the 001 vibrational state of the major isotope of CO$_2$ according to the reaction

$$N_2(v=1) + CO_2(000) \rightarrow N_2(v=0) + CO_2(001) \quad . \qquad (3-13)$$

41
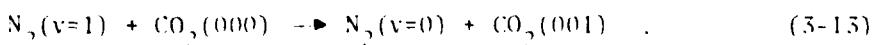
In Appendix D we describe the simple model used to compute the subsequent radiative cascade from the 001 state to lower vibrational states of CO_2 with emission in bands near 4.3, 9.4, 10.4, 13.9, 15.0, and 16.2 μm. The spectral distribution for each of these bands was adopted from the WOE code.

The model in Appendix D was applied in estimating the limb radiance from CO_2 vibraluminescence following a megaton-class high-altitude burst by utilizing values for $[N_2(v=1)]$, $[CO_2]$, and temperature determined from prior MHD/chemistry code calculations. The results, for a time of 60 sec after burst, and for the cases of 10^{-10} and 10^{-9} limb-threshold radiances at night, are shown in Figures 3-7 and 3-8, respectively, along with the previously-shown ambient results for comparison. In both cases we see that, except for the 4.3-μm band where the earth limb is raised to over 200-km altitude, the effect in the LWIR is relatively small. In rather narrow spectral regions near 9.3 μm band 10.4 μm, the limb is raised, by about 20 km, to an altitude of about 125 km. Near 13.5 μm, it is raised by about 10 km to an altitude of 120 km.*

In these calculations, the spectral yield of photons adopted was based on an atmospheric temperature of 300 °K. The actual temperature exceeded this at various points along the sight paths so that the vibra-luminescent contribution should be a little broader in wavelength than that shown in Figures 3-7 and 3-8 and would not extend quite so high in altitude. Nevertheless, the conclusion would remain essentially the same. This is, that a single high-yield, high-altitude burst should not produce sufficient CO_2 vibraluminescence to seriously degrade the LWIR window regions, especially at limb altitudes above about 125 km.

---

* The SPIRE data (Reference 3-9) indicates that the cross-hatched areas in Figures 3-7 and 3-8 (corresponding to regions where the ambient limb radiance exceeds 10^{-10} and 10^{-9}, respectively) should be a little broader near 14 μm at tangent altitudes from 100 to 120 km than that shown in these figures. Thus, the burst-induced vibraluminescence near 13.5 μm may be almost obscured by the ambient emission.

42
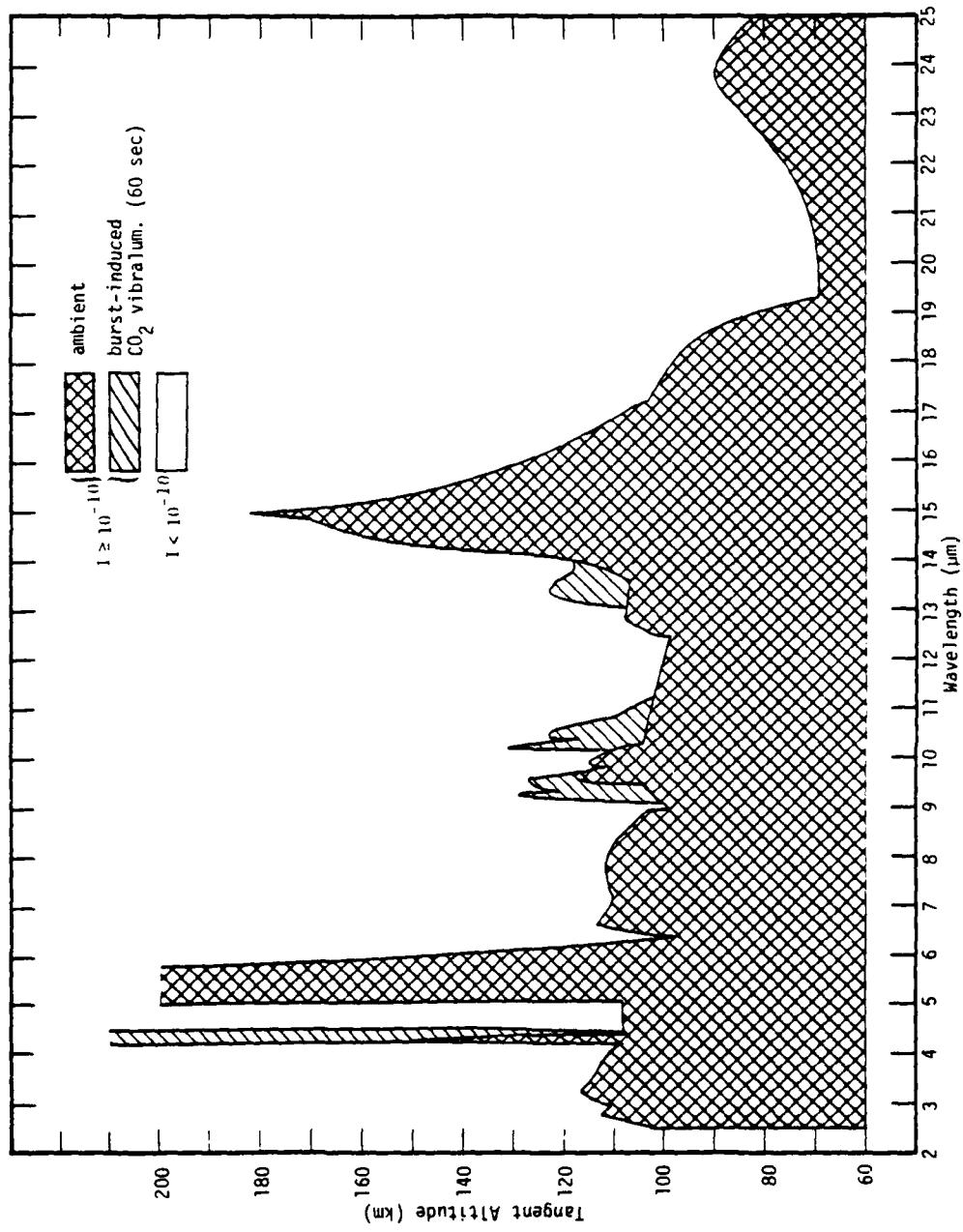
Figure 3-7. Effect on ambient nighttime limb-window radiance (10^{-10} watts cm^{-2} $ster^{-1}$ μm^{-1}) of CO_2 vibraluminescence induced by megaton-class high-altitude burst at 60 sec.
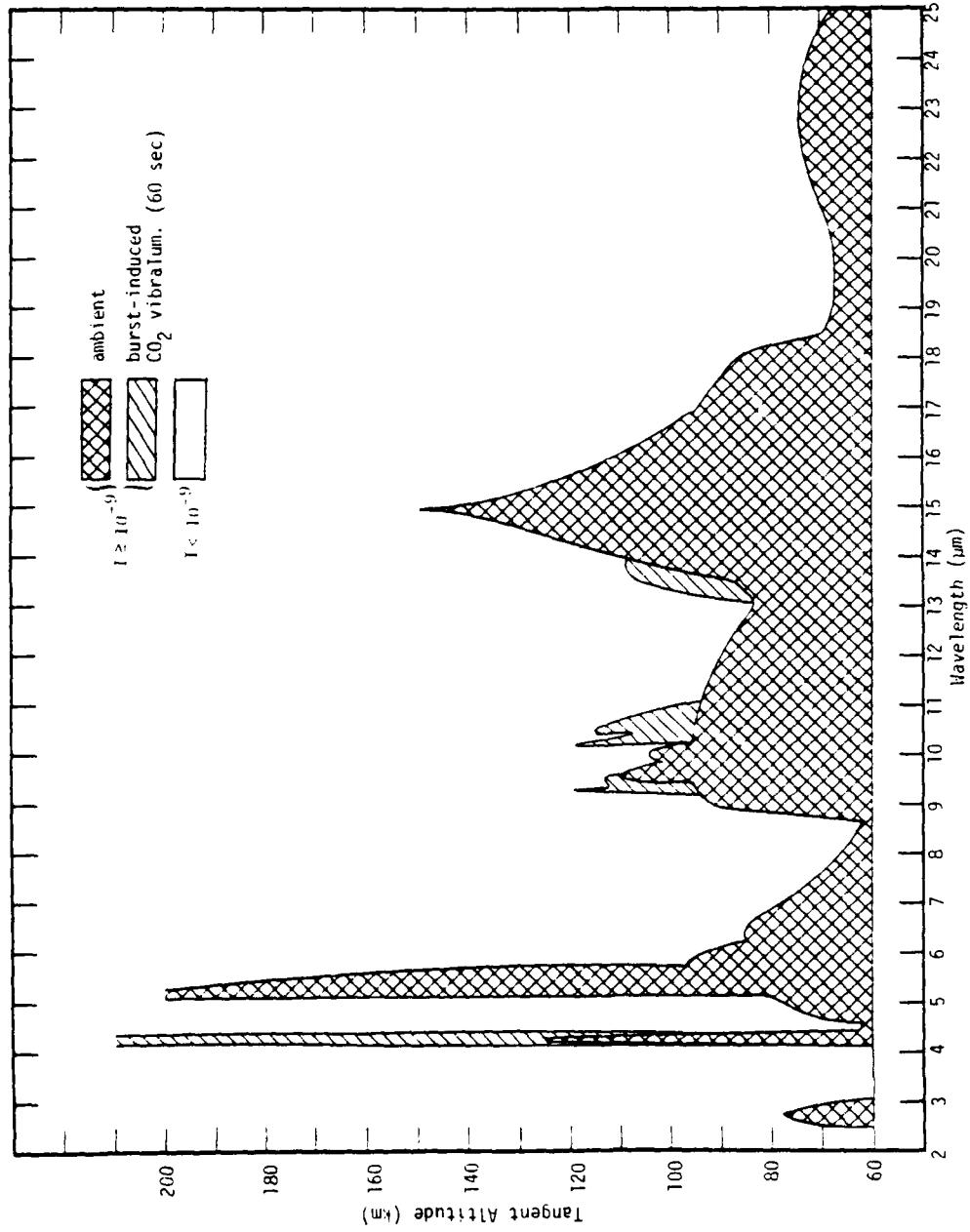
Figure 3-8. Effect on ambient nighttime limb-window radiance (10^{-9} watts cm^{-2} $ster^{-1}$ μm^{-1}) of CO_2 vibraluminescence induced by megaton-class high-altitude burst at 60 sec.

44

Uncertainties

In our estimation, the major uncertainties associated with a determination of the nuclear-induced LWIR vibraluminescence from CO_2 are related to bomb phenomenology, particularly to the dynamics of the disturbed region and its temperature distribution. Apart from these, there are, of course, other uncertainties relating to the actual mechanisms of energy transfer from N_2 to CO_2, to the internal redistribution of this energy among the many vibrational states of CO_2, and to quenching rates for the various states. Although the rate coefficient for Reaction 3-13 is well known, as are also most of the Einstein transition rates necessary for calculating the branching ratios in the radiative cascade to lower states, the rate of energy transfer from $N_2(v>1)$ to higher vibrational states of CO_2 is not well known. However, this is probably not a serious limitation, except possibly in a multiburst environment, because after a short period of time following a burst most of the $v>1$ states of N_2 should end up in the $v=1$ state, by resonance exchange with N_2 molecules in the ground vibrational state, where they can then transfer their energy to CO_2 by Reaction 3-13.

Given that the hydrodynamics and chemistry involved in the calculations leading to the results presented in Figures 3-7 and 3-8 is reasonably correct, we believe that the other uncertainties referred to above are not sufficiently great to substantially alter the LWIR results and conclusions, at least for the case of a single high-altitude burst. There has not been sufficient time to consider possible modifications in the case of a multiburst environment.

Recommendations

In Reference 1-1 a recommendation was made for laboratory experiments to measure, simultaneously, the spectral intensity of CO_2 vibraluminescence near 2.7 and 4.3 µm. We believe that, for the SWIR, this is still

45

an important experiment to perform. For the LWIR, however, no experimental work is recommended at this time.

We do recommend that further code work and/or analytical studies be carried out to determine if CO_2 vibraluminescence (LWIR) plays a more significant role in a multiburst environment than it appears to do in the single-burst case. Depending on the outcome of such studies, further consideration might then be given to the need for specific experimental work.

METAL OXIDES

Role in Nuclear Environment

Oxides formed from metallic or other weapon debris atoms have long been considered a potential threat to LWIR systems operating in a nuclear environment because most, if not all, of their fundamental bands lie in the LWIR region. Considerable work, both laboratory and theoretical, has been done over the past decade to determine the basic parameters needed to formulate good predictive models for this radiation. Much has been learned, but there are still many unknowns. Before attempting to pinpoint which, if any, of the unknowns are crucial, however, a fundamental question to answer is this. In view of the fact that LWIR systems will probably operate at tangent altitudes greater than about 120 km (to avoid the ambient earth-limb obscuration) and since much of the weapon debris from a high-altitude burst is believed to be deposited below 120 km, is the depth of the region above 120 km in which systems may be adversely affected sufficiently great to worry about? This is one of the main questions addressed in this subsection.

The metal species of potential importance in a nuclear environment have been reviewed by Gilmore (Reference 3-15). The dominant ones cited are aluminum and uranium. Many of the metals, including Fe, Li, Ni, Cu, and Mg,

46

do not react strongly with O_2 to form oxides because the reactions are endothermic. Thus, the concentrations of their oxides, following a high-altitude burst, should be sufficiently small to cause negligible interference with LWIR systems. In addition to aluminum and uranium, we will also consider oxide formation by certain fission fragments whose collective concentration may be nearly as great as that of uranium.

Aluminum (Al). Aluminum oxide can be formed by the reaction

$$Al + O_2 \longrightarrow AlO + O \qquad . \tag{3-14}$$

However, aluminum, like the other metallic species, will be fully ionized initially. For Reaction 3-14 to proceed, Al^+ must first be neutralized. This can be accomplished through radiative-collisional recombination with free electrons, but the process is very slow, requiring several hours. A possible alternative that we considered involves the formation of AlO^+ by the reaction

$$Al^+(^3P°) + O_2 \longrightarrow AlO^+(X^3\Sigma) + O(^3P) + 1.2 \text{ eV} \tag{3-15}$$
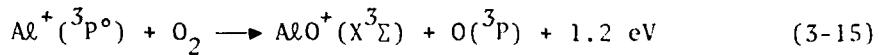
followed by dissociative recombination of AlO^+ with electrons:

$$AlO^+ + e \longrightarrow Al + O \qquad . \tag{3-16}$$

Here, $Al^+(^3P°)$ is the lowest triplet state of Al^+. It is metastable and has sufficient energy (4.65 eV) to make Reaction 3-15 exothermic. The difficulty with this scheme, however, is that AlO^+ can also be destroyed by reaction with atomic oxygen:

$$AlO^+ + O \longrightarrow Al^+ + O_2 \tag{3-17}$$

which has a rate coefficient (unmeasured) that is probably on the order of 10^{-10} cm^3 sec^{-1}. Thus, given a rate coefficient for Reaction 3-16 of about 4×10^{-7} cm^3 sec^{-1}, Reaction 3-17 will dominate Reaction 3-16 when $[O] \approx 4 \times 10^3 N_e$, where N_e is the electron density. Except within the

47

fireball region (where A&O would not be formed anyway), this condition is generally satisfied following megaton-class high-altitude bursts.

We conclude that A&O formation, following a high-altitude burst, is probably insufficient to cause degradation of LWIR systems.

Uranium (U) and Fission Fragments (FF). The situation with respect to uranium, and at least several of the fission fragments (including Zr, La, Sm, Nd, Y, Ce, Pr), is quite different. It is not necessary to first neutralize the ions because they can react directly with O_2 to form oxide ions that are very stable. For example, the reactions

$$U^+ + O_2 \rightarrow UO^+ + O + 3.1 \text{ eV} \quad (k \approx 8.5 \times 10^{-10}) \text{]} \qquad (3\text{-}18)$$

$$UO^+ + O_2 \longrightarrow UO_2^+ + O + 2 \text{ eV} \quad (k \approx 2 \times 10^{-9}) \qquad (3\text{-}19)$$
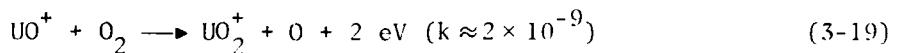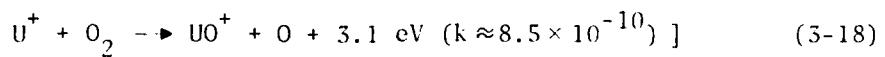
proceed rapidly to form the LWIR-emitting species UO^+ and UO_2^+. In fact, with the measured values for the rate coefficients shown above, most U^+ ions deposited in the ambient atmosphere would be converted to UO_2^+ ions in less than 1 sec for altitudes up to 170 km, and in less than 1 minute for altitudes to 280 km. Once formed, these ions should retain their identity because their dissociation energy is nearly 8 eV. The dissociative recombination reaction

$$UO_2^+ + e \longrightarrow UO + O \qquad (3\text{-}20)$$

is endothermic by 2 eV and should be quite ineffective in destroying the UO_2^+. The same is true for UO^+ ions.

Once formed, the UO_2^+ and UO^+ ions can be excited continuously by earthshine scatter at night and, possibly in addition, by solar pumping by day.

Similar remarks apply to the above-mentioned fission-fragment oxides (for which the dissociation potential exceeds the ionization potential).

We have attempted to estimate the magnitude of the limb radiance
from uranium and fission-fragment oxide ions as a function of altitude for
selected times following a megaton-class high-altitude burst. The details
of this calculation are presented in Appendix E. In this section we will
just give a brief description of the procedure adopted and a composite
picture of the final results.

The daytime spectral limb radiance is determined from the
expression

$$1 = 1.58 \times 10^{-20} \frac{(\dot{\phi}_e + \dot{\phi}_s)}{\lambda_\mu \Delta\lambda_\mu} \int [\text{oxide}] d\ell \quad (\text{watts cm}^{-2} \text{ ster}^{-1} \text{ } \mu\text{m}^{-1})$$

(3-21)

where the integral represents the column number density (molecules cm^{-2}) of
oxide ions along a detector's sight path, $\dot{\phi}_e$ and $\dot{\phi}_s$ are the rates of
photon emission per molecule by earthshine and sunlight scatter, respectively,
λ_μ is the wavelength in micrometers, and $\Delta\lambda_\mu$ is the effective bandwidth
over which the radiation occurs.* At nighttime, $\dot{\phi}_s = 0$. Values of $\dot{\phi}_e$ and
$\dot{\phi}_s$ for uranium and fission-fragment oxide ions are not known. To be
explicit, we have assumed both of them equal to 0.2, the same as for AℓO
(see Appendix E).

Briefly, the column density of oxide ions along a limb path was
estimated by considering the following sequence of events. To begin with,
we assume that 7×10^{26} U^+ ions and 3×10^{26} fission fragment ions† are

_____

* For uranium and fission-fragment oxide ions, the band shapes are not well
  known. For simplicity, we assume here that the contributing bands of
  UO_2^+ and UO^+ radiate uniformly over the region from 10.5 to 12.5 μm
  ($\Delta\lambda_\mu = 2$) and that the fission-fragment oxide ions radiate uniformly over
  the region from 9.5 to 13.5 μm ($\Delta\lambda_\mu = 4$). See also Appendix E.

† These numbers are based on 2×10^{27} uranium atoms present initially.
  Thirty percent of these are assumed to fission leaving 1.4×10^{27} U^+ ions
  and 1.2×10^{27} fission-fragment ions. Half of these are lost in the upward
  direction and half are deposited in the downward hemisphere. Fifty percent
  of the fission-fragment ions are assumed to be of a variety that can form
  oxide ions.

ejected toward the downward hemisphere with the common velocity of 2×10^8 cm sec^{-1}. The component of the velocity of these ions normal to the earth's magnetic field pushes the field outward and it, in turn, drags the air ions with it. In this manner, a considerable fraction of the initial debris kinetic energy is transferred to the air ions. It is the air ions that ultimately deposit most of the original debris kinetic energy. Following the debris-air interaction, the energy-degraded debris ions will be left with a velocity distribution. The fastest moving ions will be deposited at the lowest altitude possible; the slower ones will be deposited at higher altitudes. There will thus be established an initial vertical distribution of the debris ions that will be dependent on their velocity distribution immediately following the debris-air interaction. After the air ions have deposited their kinetic energy, an upward motion of the heated atmosphere will ensue which will carry the debris ions with it and, thereby, alter their vertical distribution. Given the velocity distribution of the debris ions, we can compute the initial vertical distribution of these ions. Given a model for the subsequent heave, we can then calculate the vertical distribution of the ions at subsequent times. If, additionally, the lateral spread of the debris ions is known, the column number density in the horizontal direction can be found as a function of limb altitude and time after burst.

As described in Appendix E, the lateral spread of the debris from a megaton-class high-altitude burst is taken to be 200 km. Two initial vertical distributions of the debris ions were calculated. One of them corresponds to a velocity distribution proportional to v^{-2} (Case 1); the other to a velocity distribution independent of v (Case 2). In both cases the subsequent vertical distributions were determined from the MICE-code description of the heave. In determining whether a debris particle is an oxide ion or an atomic ion we assume, because of the large rates for Reactions 3-18 and 3-19, that oxidation will occur where O_2 is not dissociated, i.e., everywhere outside the fireball plume. Elsewhere, the ions are taken to be atomic.

50

The calculated limb radiance from uranium and fission-fragment oxide ions as a function of tangent altitude, and for selected times after burst, is shown in Appendix E for Cases 1 and 2 (Figures E-8 to E-11 and E-13 to E-16). Although the detailed shapes of the radiance-altitude curves are different for the two cases, the altitude regions over which the limb radiance exceeds a certain value (say 10^{-10}) are nearly the same in both cases. We conclude from this that a determination of the limb-window regions is not particularly sensitive to the assumed velocity distribution of the debris ions.

The detailed results presented in Appendix E have been used to show the possible effect of uranium and fission-fragment oxide ions on the ambient limb-window regions. The results, for tangent altitudes to 200 km, are shown in Figures 3-9 through 3-12. Figure 3-11 shows, for example, that by day the limb radiance from fission-fragment oxide ions may exceed 10^{-10} watts cm^{-2} $ster^{-1}$ μm^{-1} (at certain times after burst) for tangent altitudes ranging from about 130 km to over 200 km in a wavelength band extending from about 9.5 to 13.5 μm.* Also, Figure 3-11 shows limb radiances from uranium oxide ions exceeding 10^{-10}, at certain times, for tangent altitudes from about 120 km to over 200 km in a wavelength band from about 10.5 to 12.5 μm.

Figures 3-13 and 3-14, respectively, show the effect on the 10^{-10} and 10^{-9} ambient limb-window radiances at nighttime from uranium and fission-fragment oxide ions as well as the burst-induced effects from the other molecular species considered earlier in this report. For the 10^{-10} window in particular, the potential effect of the uranium and fission-fragment oxide ions is seen to be considerable. The effect is particularly note-worthy in view of the fact that the oxide ions should be striated along the magnetic field lines and thus give rise to structured radiation in the LWIR.

---

* Actually, according to Figures E-16 and E-9, at a time of 210 sec the radiance from the fission-fragment oxide ions and the uranium oxide ions exceeds 10^{-10} for altitudes to nearly 300 km and 500 km, respectively.
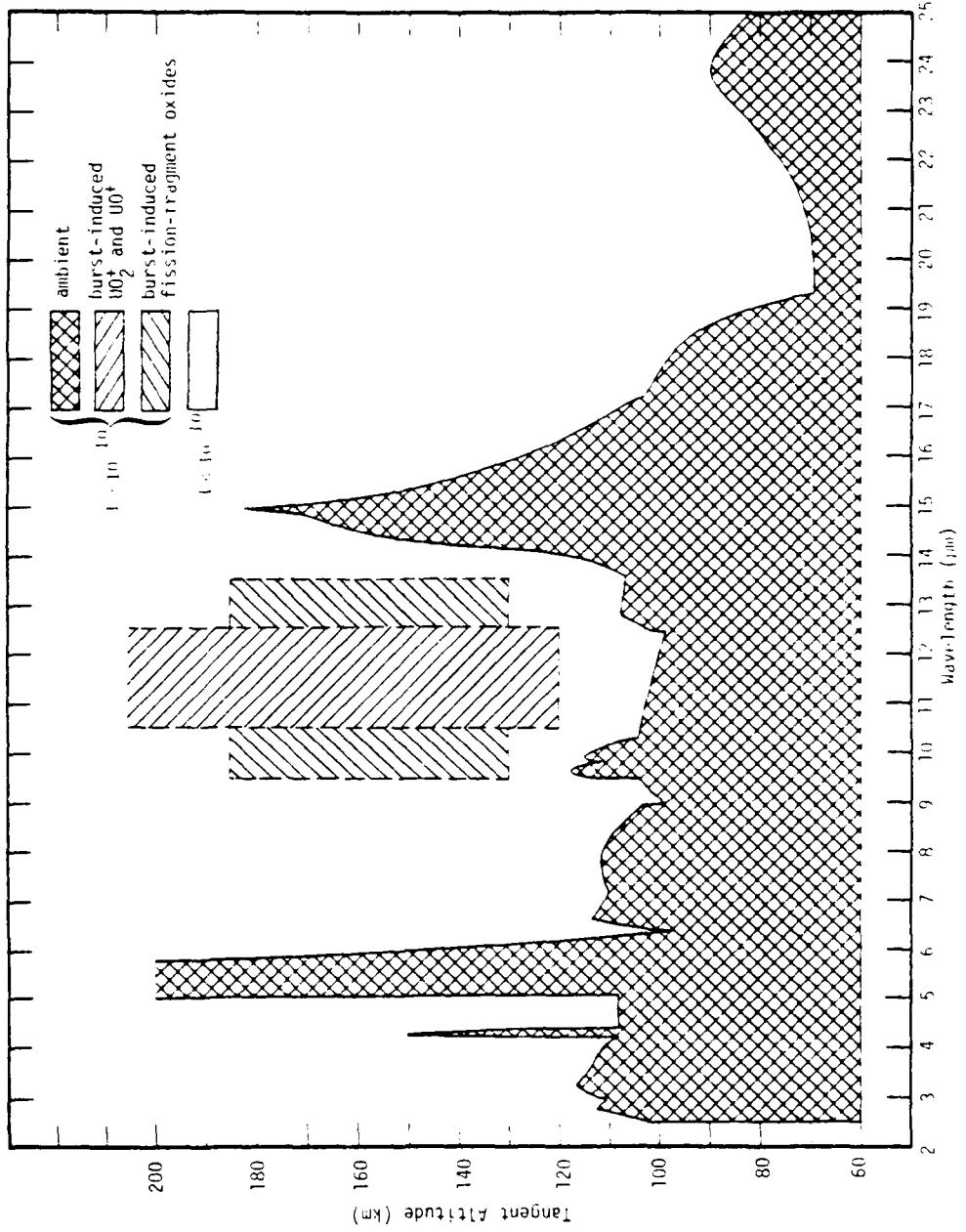
Figure 3-9. Possible effect on ambient nighttime limb-window radiance (10^{-10} watts cm^{-2} $ster^{-1}$ μm^{-1}) of earthshine scatter from UO_2^+ and UO^+ and from fission-fragment oxides formed following megaton-class high-altitude burst.

52
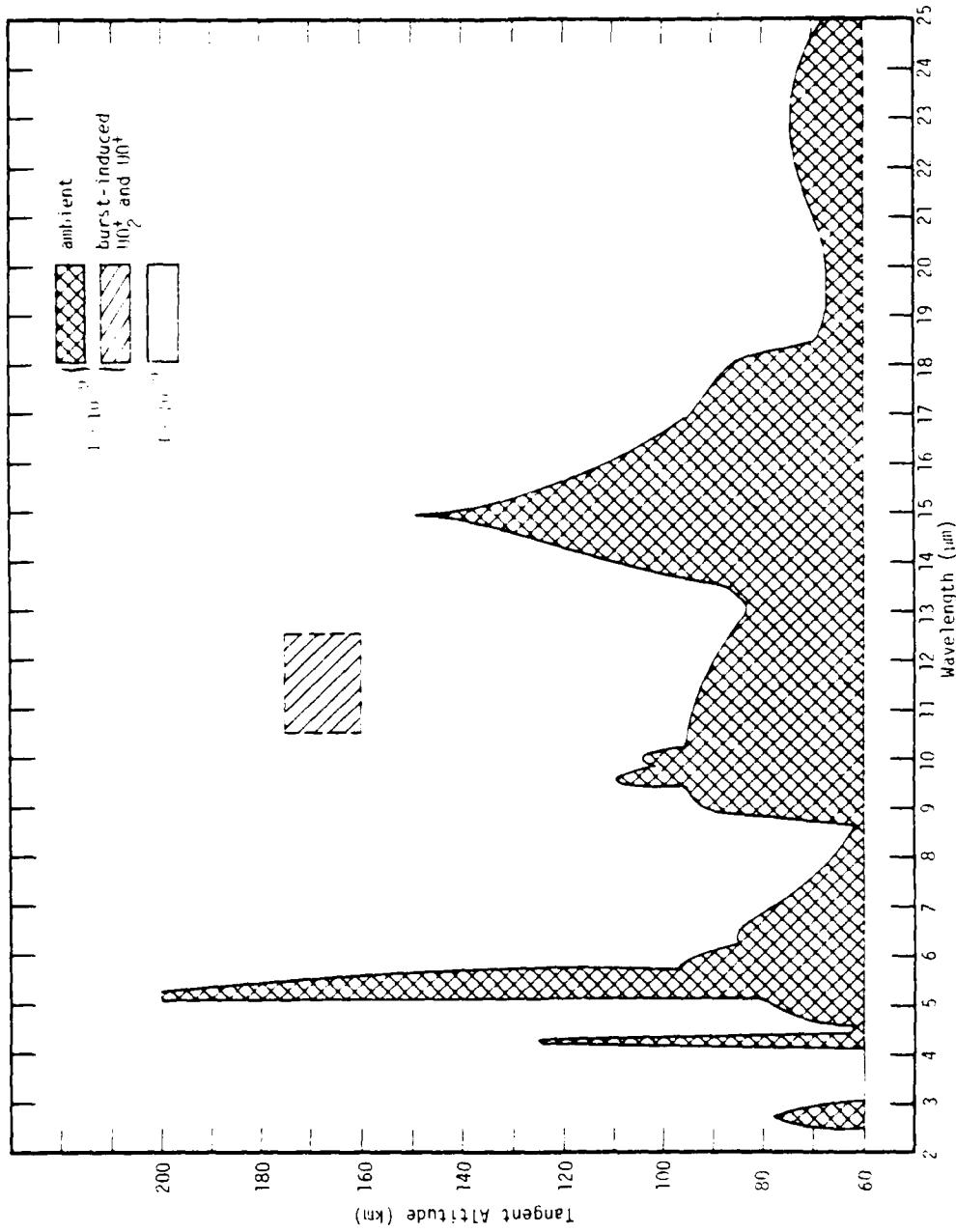
Figure 3-10. Possible effect on ambient nighttime limb-window radiance (10^{-9} watts cm^{-2} ster^{-1} μm^{-1}) of earthshine scatter from UO_2^+ and UO^+ formed following a megaton-class high-altitude burst.
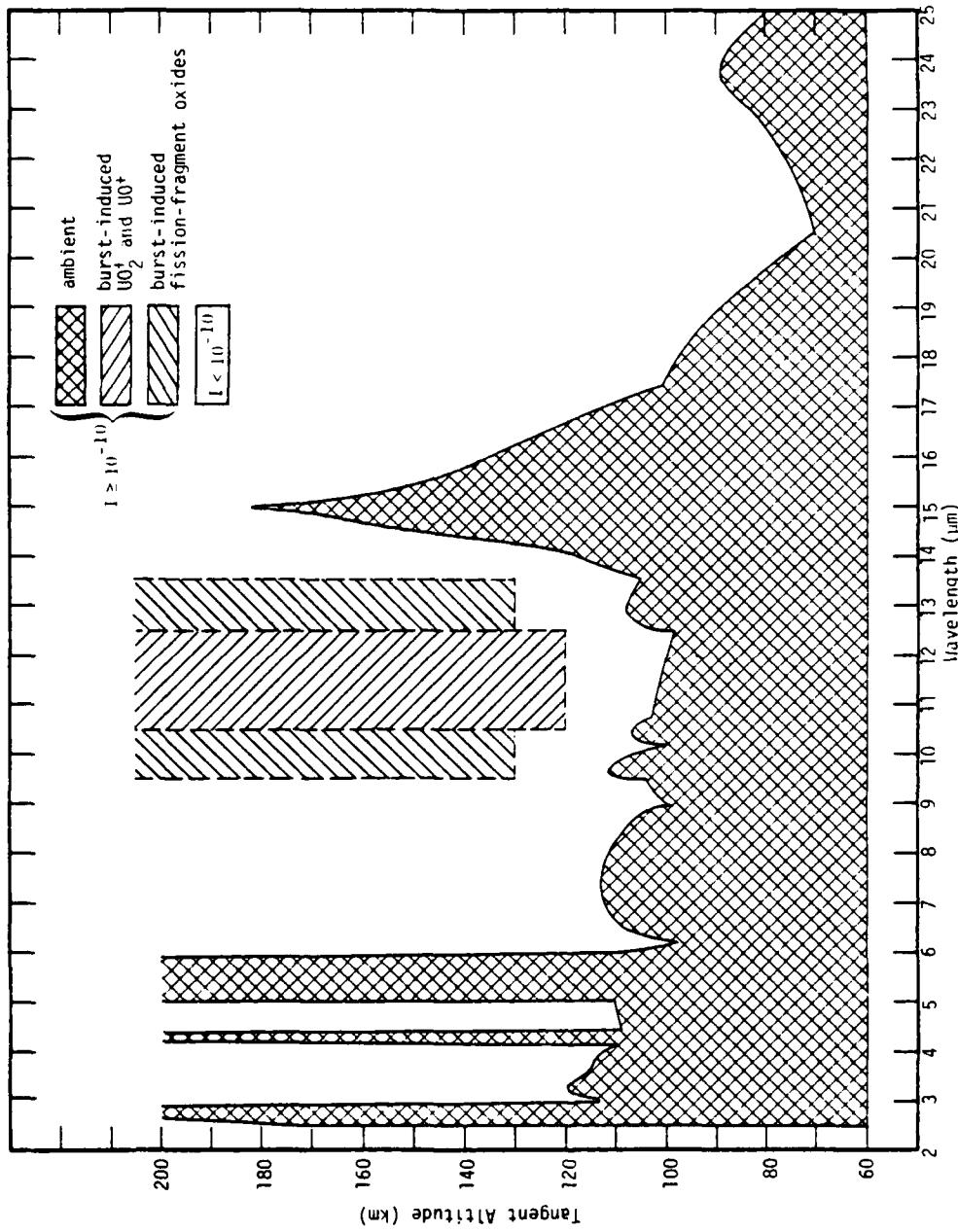
Figure 3-11. Possible effect on ambient daytime limb-window radiance (10^{-10} watts cm^{-2} $ster^{-1}$) of solar and earthshine scatter from UO_2^+ and UO^+ and from fission-fragment oxides formed following megaton-class high-altitude burst.
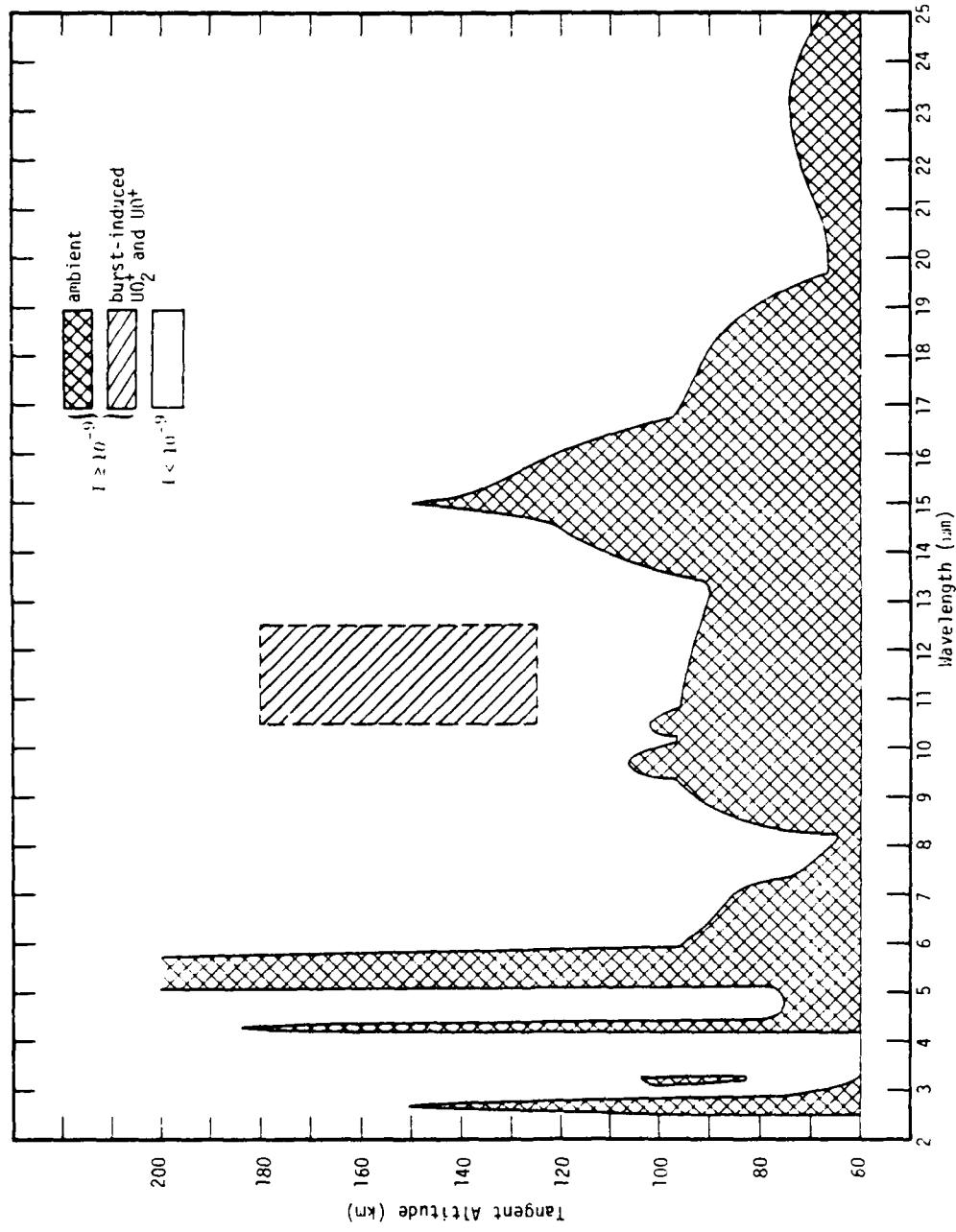
Figure 3-12. Possible effect on ambient daytime limb-window radiance (10^{-9} watts cm^{-2} $ster^{-1}$) of solar and earthshine scatter from UO_2^+ and UO^+ formed following megaton-class high-altitude burst.
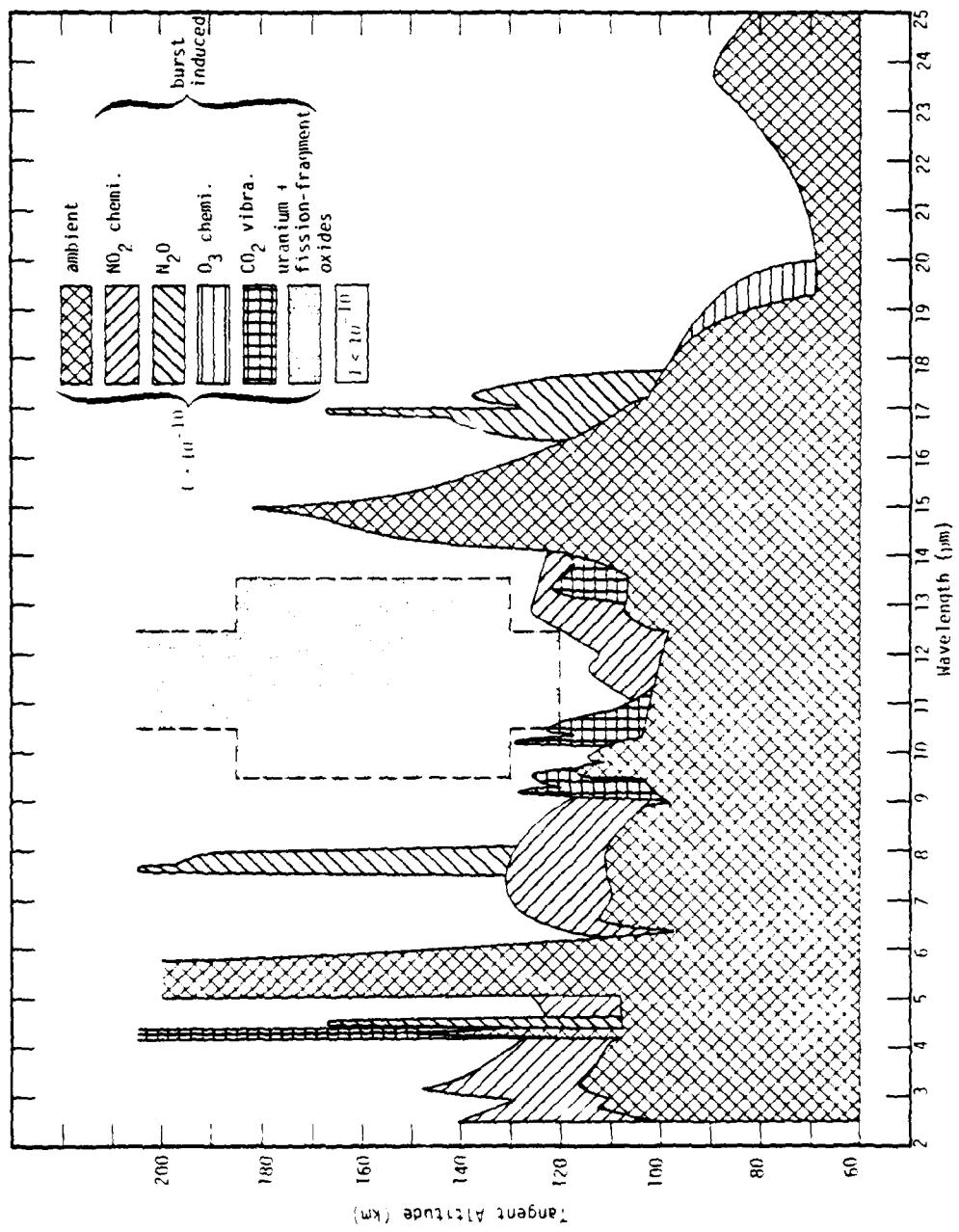
Figure 3-13. Estimated effect on ambient nighttime limb-window radiance (10^{-10} watts cm^{-2} $ster^{-1}$ μm^{-1}) from molecular radiation induced by megaton-class high-altitude burst.

56
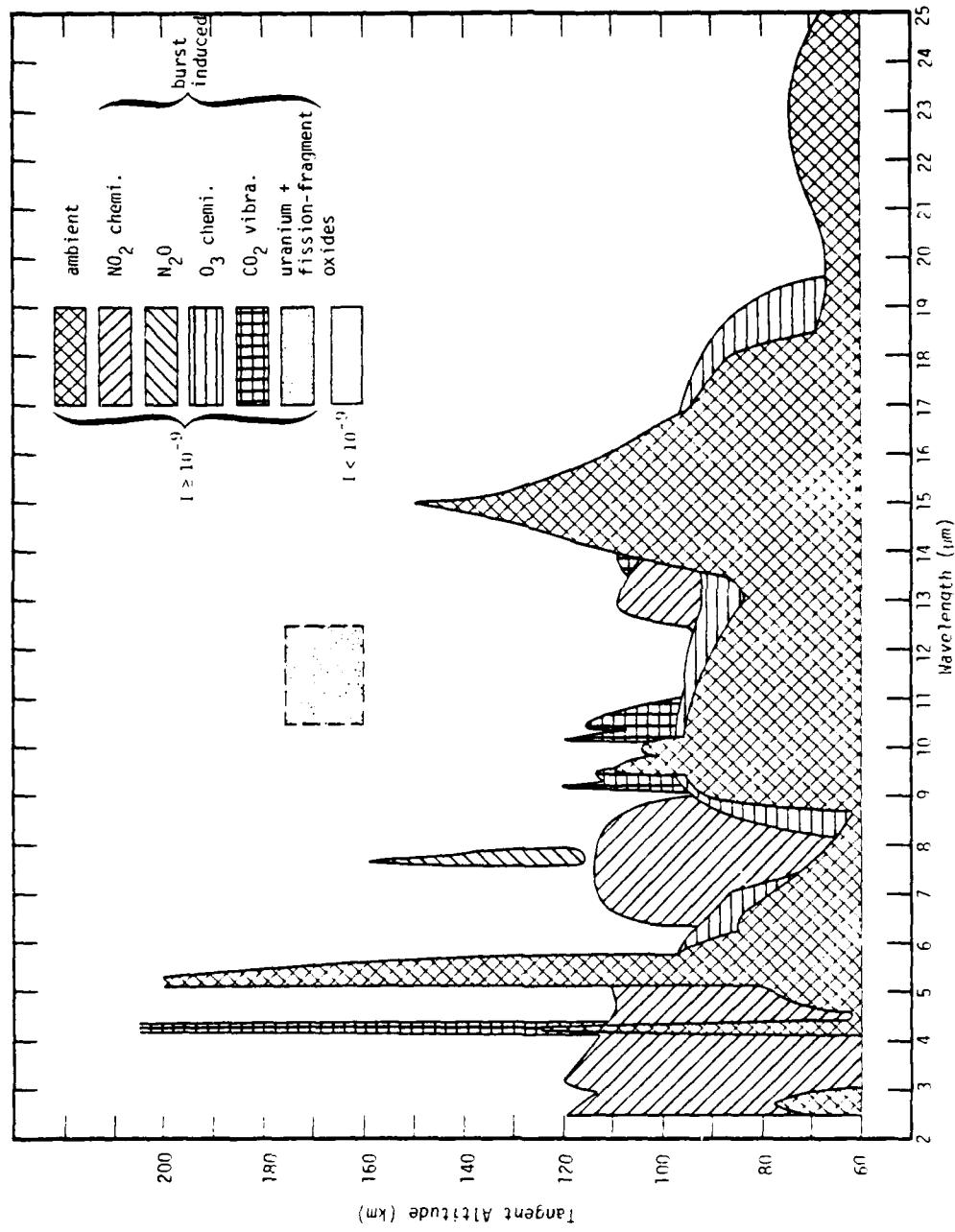
Figure 3-14. Estimated effect on ambient nighttime limb-window radiance (10^{-9} watts cm^{-2} $ster^{-1}$ μm^{-1}) from molecular radiation induced by megaton-class high-altitude burst.

57

Uncertainties

Apart, again, from uncertainties in the phenomenology relating to debris deposition and atmospheric heave, the major uncertainties involved in an accurate prediction of the LWIR emission from uranium and fission-fragment oxide ions relate to the spectroscopic properties of the ions. To our knowledge, the band strengths (or f numbers) for neither the vibration-rotation (V-R) transitions nor the electronic transitions are known for any of the ions. These quantities are required for a calculation of the IR emission rate by earthshine and sunlight absorption. Our assumed values for these rates, based on the rates for $A\ell O$, could well be in error by at least an order of magnitude. Furthermore, the band positions of the fission-fragment oxide ions are not well known nor, indeed, is that of UO^+, although the positions of the neutral oxides are known except for the fission fragments Sm and Nd. If the LWIR sensor is broad banded, then the exact positions of the oxide bands may not be too important, but we cannot at present be assured of that.

Recommendations

In view of the potential importance of uranium and fission-fragment oxide ions in a nuclear environment, we recommend that experiments be performed to determine:

1. The absorption oscillator strengths (f numbers) for the fundamental V-R bands of UO_2^+, UO^+, and selected fission-fragment oxide ions from among the group: ZrO_x^+, LaO_x^+, SmO_x^+, NdO_x^+, YO_x^+, CeO_x^+, PrO_x^+ $(x = 1,2)$.

2. The f number(s) for permitted electronic transitions connected to the ground state, for the same species listed under Item 1 above.

If Items 1 and 2 are performed successfully, the LWIR excitation rates of the species by earthshine and sunshine scattering can be computed. If these rates turn out to be sufficiently small to render the species unimportant in a nuclear environment, then obviously no further work is required. If, however, the rates are comparable to, or greater than, those for AℓO, then we recommend further work to determine:

3. The wavelength positions of the fundamental V-R bands of UO^+ and the fission-fragment oxide ions listed in Item 1 above, especially SmO_x^+ and NdO_x^+ $(x = 1,2)$.

ELECTRONS (PLASMA RADIATION)

Role in Nuclear Environment

We consider here the emission from plasma in the plume of a megaton-class, high-altitude burst. Included is continuum radiation resulting from free-free and free-bound collisions between electrons and ions as well as line radiation from bound-bound transitions that may occur following radiative-collisional recombination in an O^+/N^+ plasma. The potential importance of this radiation for an LWIR system is twofold. First, there is the relatively large dimension of the fireball plume that extends to altitudes of several hundred kilometers. Second, there is the fact that after a few tens of seconds the plasma will be striated along the magnetic field lines with the result that the infrared radiation that arises will be structured. In this section we attempt to estimate the magnitude and the spatial and temporal extent of the mean plasma radiance by utilizing MELT-code results of electron density and temperature in the fireball plume. These results can then be compared with the results presented above for molecular radiation so as to establish the relative importance of each.

59

The volume emission rate due to free-free (ff) + free-bound (fb) collisions of electrons with ions can be written as the frequency (ν)-independent expression (Reference 3-16)

$$J_\nu(ff+fb) = \frac{8\pi^{1/2}}{3\sqrt{6}} \left(\frac{g}{g_+}\right) \frac{e^6}{m^{3/2}c^3} \frac{N_+N_e}{(kT_e)^{1/2}} \quad (\text{ergs cm}^{-3}\text{ sec}^{-1}\text{ ster}^{-1}(\Delta\nu)^{-1})$$

(3-22)

Here, e and m are the electron charge and mass, respectively, N_e and N_+ are the electron and positive ion concentrations, respectively, T_e is the electron temperature (°K), k is Boltzmann's constant, and g/g_+ is the ratio of statistical weights of the ground states of the neutral and ion species. For hydrogen-like ions, which we assume here, $g/g_+ = 2$. Alternatively, with $N_+ = N_e$, and with a change of units, Equation 3-22 becomes

$$J_\nu(ff+fb) = 5.39 \times 10^{-46} N_e^2 T_e^{-1/2} \quad (\text{watts cm}^{-3}\text{ ster}^{-1}(\Delta\nu)^{-1})$$

(3-23)

or,

$$J_{\lambda_\mu}(ff+fb) = 1.62 \times 10^{-31} \frac{N_e^2 T_e^{-1/2}}{\lambda_\mu^2} \quad (\text{watts cm}^{-3}\text{ ster}^{-1}\text{ }\mu m^{-1})$$

(3-24)

where λ_μ is the wavelength in micrometers.

For the volume emission rate due to bound-bound (bb) transitions we have used the approximate expression (Reference 3-17)

$$J_{\lambda_\mu}(bb) = 2.65 \times 10^{-20} \frac{\alpha N_e^2}{T^{0.2145}\lambda_\mu^{1.97}} \quad (\text{watts cm}^{-3}\text{ ster}^{-1}\text{ }\mu m^{-1})$$

(3-25)

where α, the radiative-collisional recombination coefficient, is determined by

$$\alpha \approx 5.75 \times 10^{-13} N_e^{-0.1} \left(\frac{T_e}{11606}\right)^{[-0.0501(\log_{10}N_e)^2+0.4641\log_{10}N_e-1.913255]}$$

(3-26)

and T is the neutral temperature (°K).

The maximum plasma limb radiance, as a function of tangent altitude for the geometrical arrangement depicted in Figure 3-15, was computed by integration of the volume emission rate (determined from Equations 3-24 and 3-25) along sight paths through the fireball plume. The results, for times of 224 and 630 sec, are shown in Figure 3-16 along with corresponding results for the ambient ionosphere. The burst-induced radiance is seen to decrease rather slowly with increasing tangent altitude so that, for example, even at 630 sec, and for wavelengths up to 10 μm, the limb radiance exceeds 10^{-10} for altitudes to at least 450 km. However, it should be pointed out that we have chosen sight paths nearly parallel to the earth's field so as to maximize the path lengths through the brightest part of the plume. For sight paths more normal to the magnetic field the intensity would not be so large.

Figures 3-17 and 3-18 present the results in our "window" format, showing the regions in altitude-wavelength space where the limb radiance exceeds 10^{-10} and 10^{-9} watts cm^{-2} $ster^{-1}$ $μm^{-1}$, respectively. Included for comparison in these figures is the effect due to ambient nighttime molecular emission. It is clear that the plasma radiation can be very effective in wiping out the window regions, especially the 10^{-10} window (Figure 3-17), to high altitudes. For example, at a time of 224 sec, the limb radiance exceeds 10^{-10} for wavelengths to 12 μm at tangent altitudes to 500 km, and for wavelengths to 26 μm at tangent altitudes to 200 km. In fact, if one compares Figures 3-13 and 3-17, it appears that the nuclear-induced plasma radiation can be much more effective than the nuclear-induced molecular emissions in causing degradation of LWIR window regions, particularly 10^{-10} (and smaller) windows, for times to several hundred seconds after the burst. This point is further amplified by the fact that the plasma is striated, unlike the molecular species (with the exception of the uranium and fission-fragment oxides), so that the emission is structured accordingly. However, it is not entirely fair to compare Figures 3-13 and 3-17 directly because they refer to different geometrical arrangements. Figure 3-13 refers to the

61
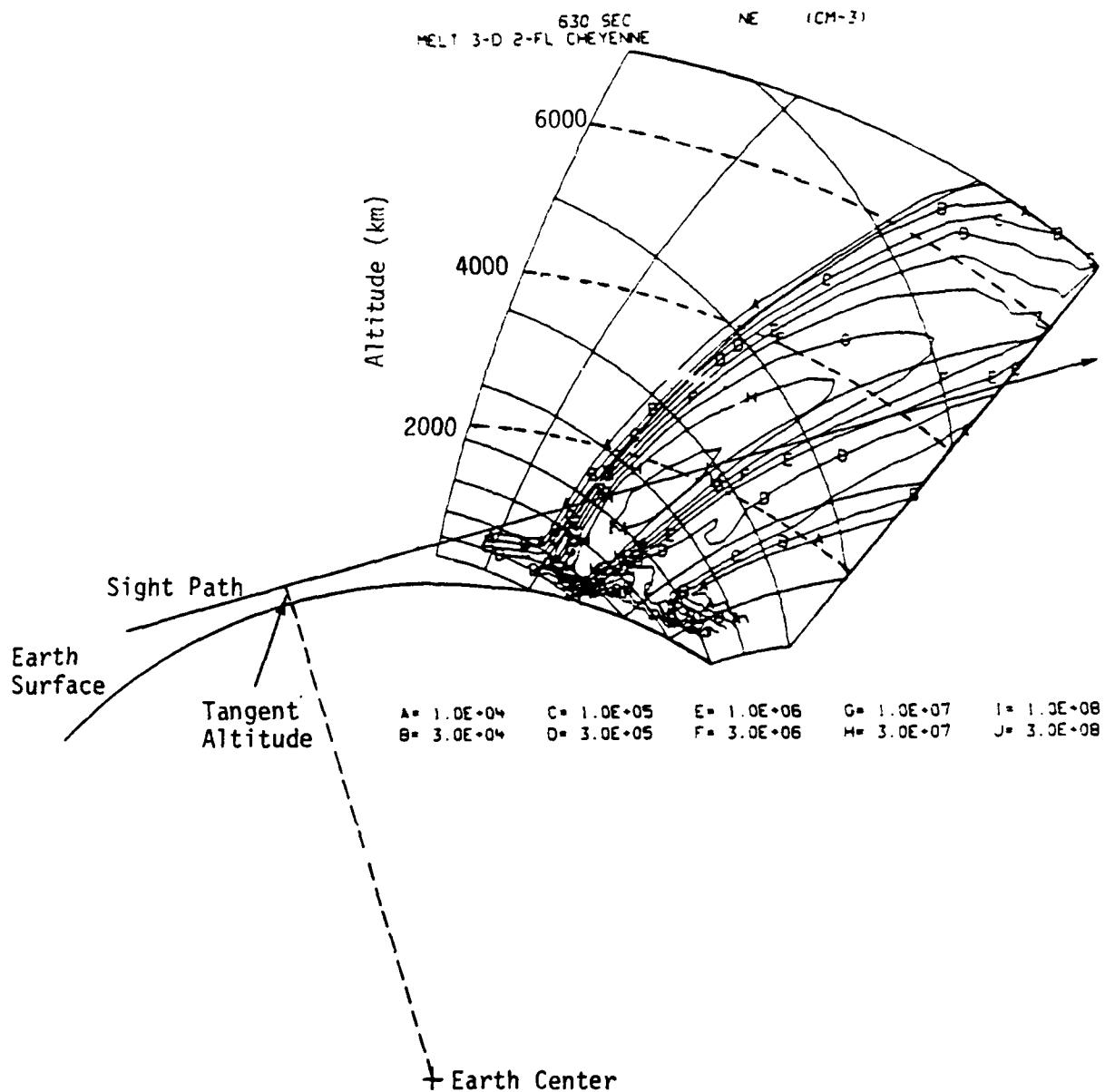
Figure 3-15. Contours of electron density (cm^{-3}) at 630 sec after
megaton class high-altitude burst showing typical
sight path for plasma radiation calculation.
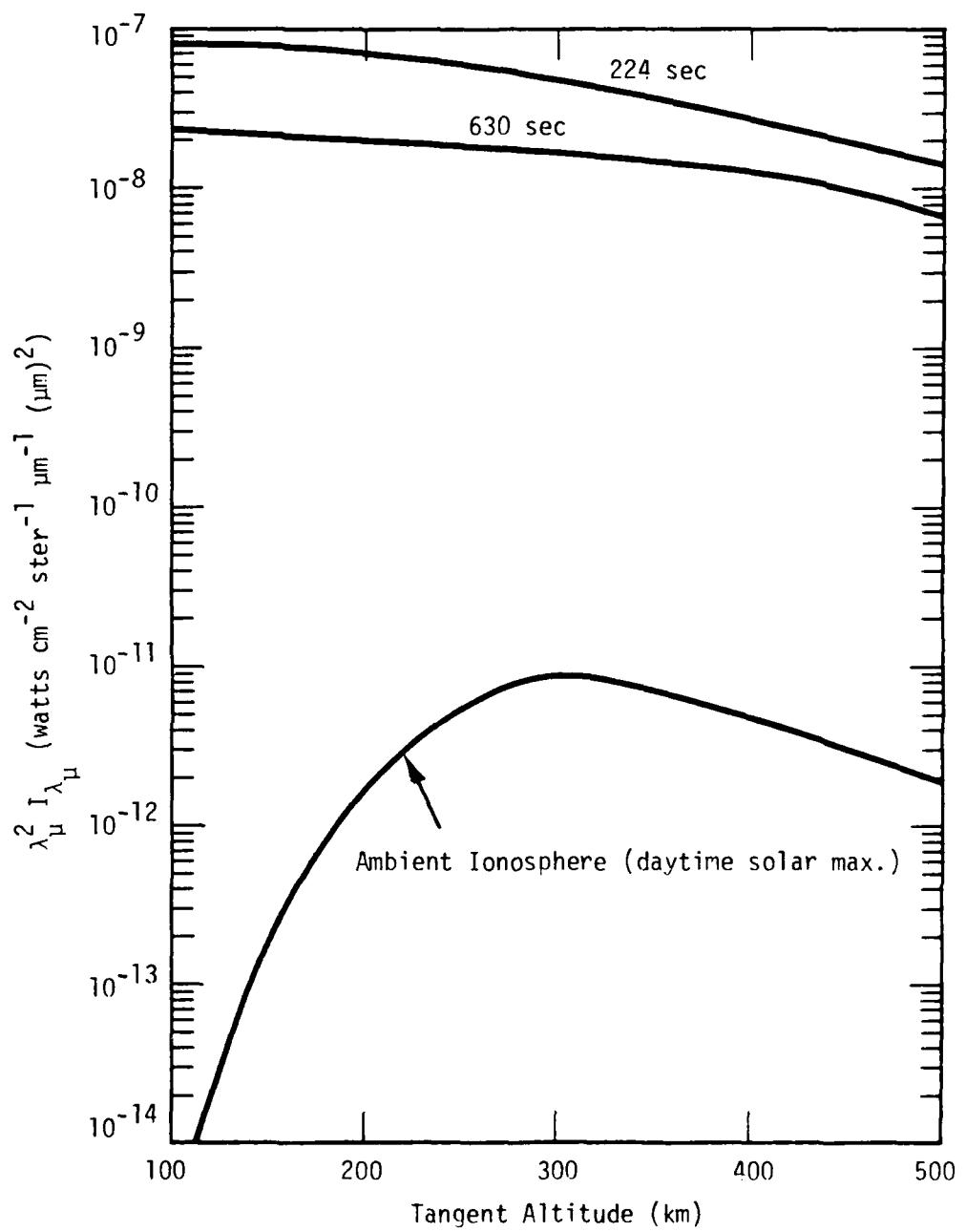
Figure 3-16. Calculated plasma limb radiance (free-free + free-bound + bound-bound) from plume of a megaton-class high-altitude burst for sight paths similar to that shown in Figure 3-15.
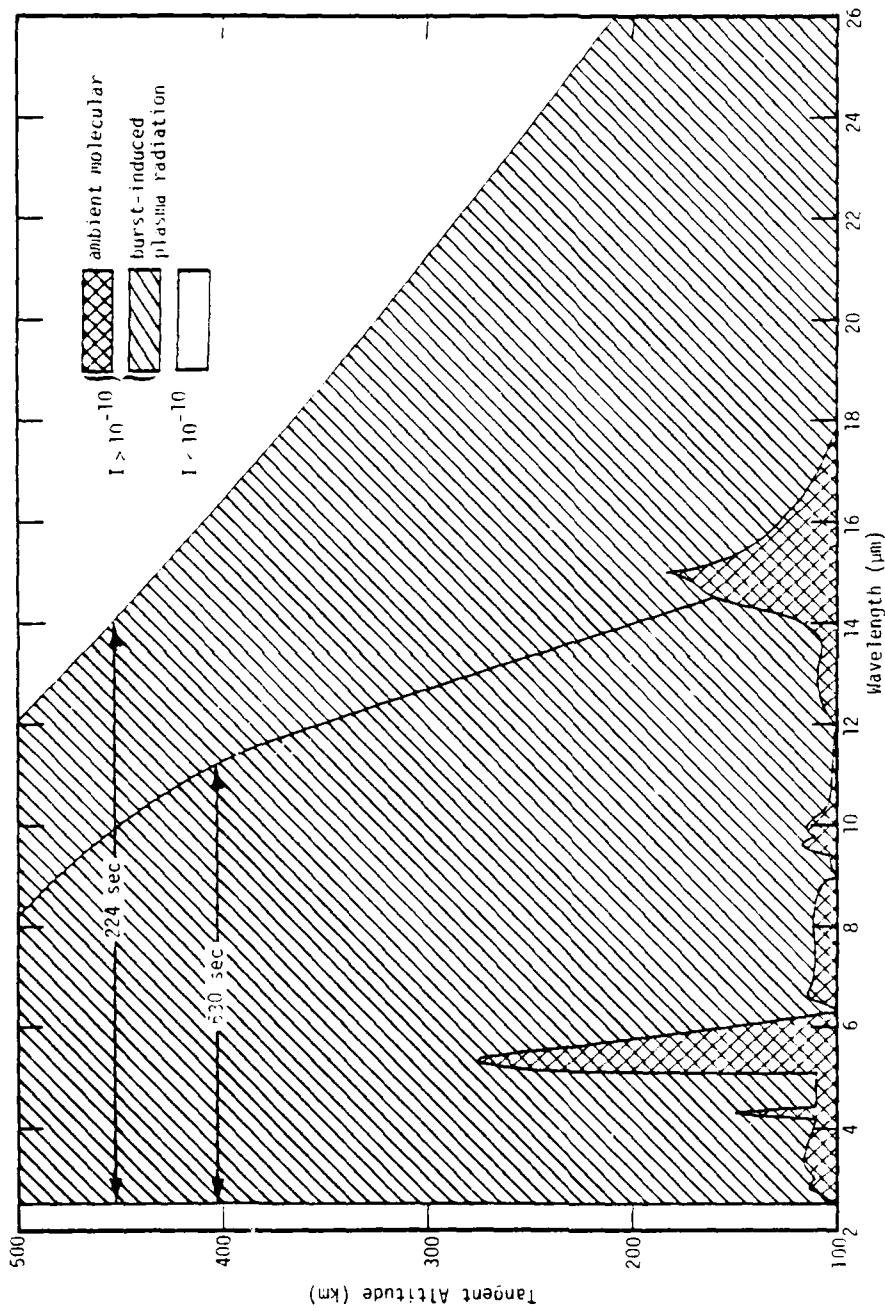
Figure 3-17. Possible effect on ambient nighttime limb-window radiance (10^{-10} watts cm^{-2} $ster^{-1}$ μm^{-1}) from plasma radiation induced by a megaton-class high-altitude burst.
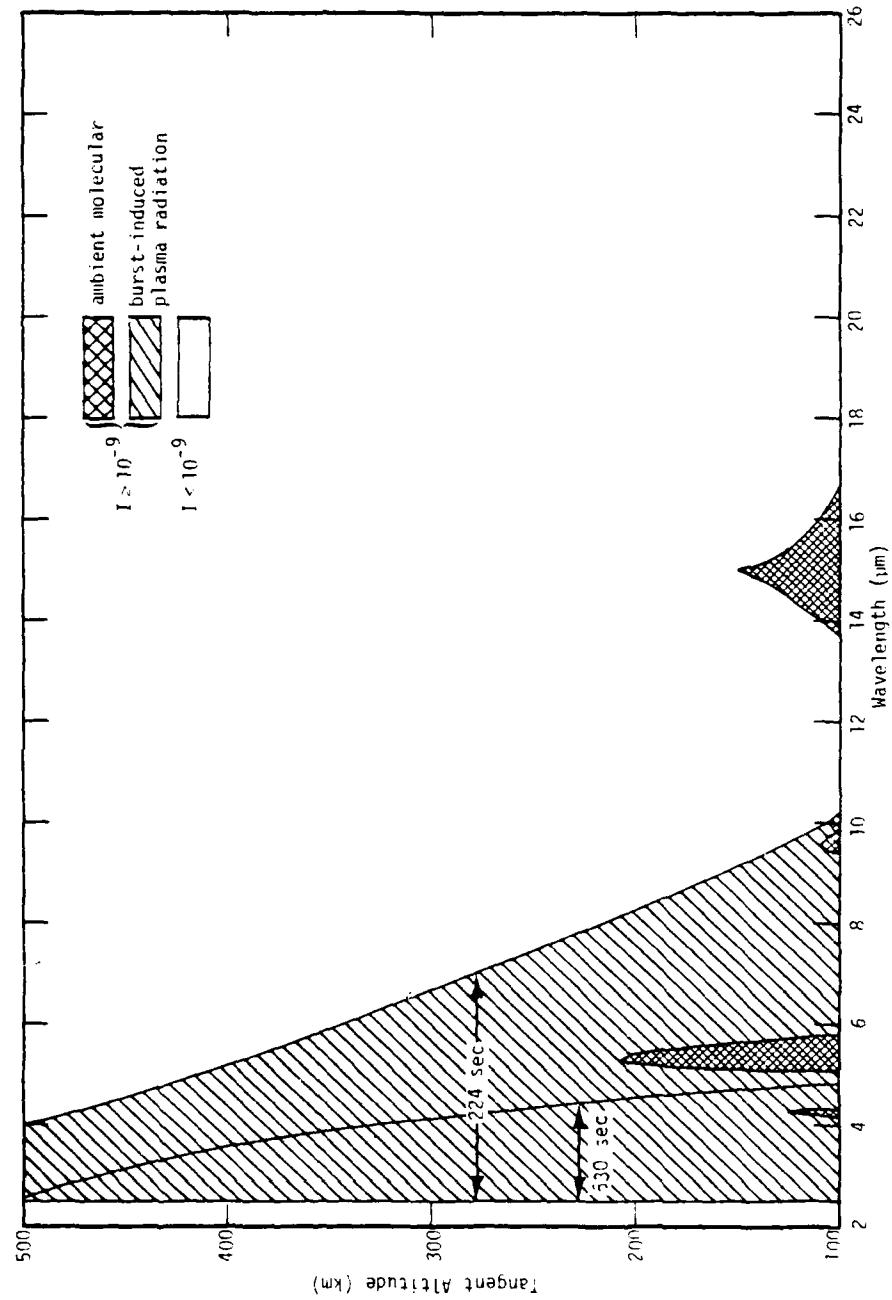
Figure 3-18. Possible effect on ambient nighttime limb-window radiance
(10^{-9} watts cm^{-2} $ster^{-1}$ μm^{-1}) from plasma radiation induced
by a megaton-class high-altitude burst.

radiance along tangent paths whose nadir is directly below the burst point.
Figure 3-17 refers to the radiance along tangent paths whose nadir is dis-
placed by about 4000 km from the sub-burst point (as in Figure 3-15). Thus,
in the representation of Figure 3-13, the plasma radiance would be negligible
at tangent altitudes below about 500 km, but would exceed 10^{-10} for tangent
altitudes from about 600 or 700 km to at least 1500 km for times to several
hundred seconds. The molecular emissions would be important in selected
bands to perhaps 200- or 300-km altitude and the plasma radiation important
over a large region above about 500 km. There would presumably be a "window"
at all wavelengths in the tangent altitude region from perhaps 300 to 500 km.

Uncertainties

Apart from uncertainties related to a determination of the electron
density and temperature distribution in the fireball plume, the largest
uncertainty associated with a prediction of the mean plasma radiance is in
the calculation of the bound-bound emission. As far as the free-free +
free-bound continuum is concerned, the Kramers-Unsold formula (Equation 3-22)
is on fairly solid theoretical ground and there is no good reason to suspect
much error in it. However, accurate prediction of the LWIR bound-bound line
emission requires good knowledge of the population of energy levels near the
ionization limit of O and N atoms, their energy separation, and transition
rates between the levels. None of these quantities is known with much
precision. Theoretical models have been developed (References 3-17 to 3-20)
to describe this radiation, but experimental data to corroborate them are
scarce. Nevertheless, since LWIR systems are likely to be broad banded
(to maximize the intensity of the received signal), the exact positions of
the LWIR lines from recombining plasma are probably not critical. Further-
more, the low-resolution formula 3-25 yields values for the bound-bound
contribution that are generally comparable to those from the free-free +
free-bound mechanism over much of the fireball plume. It is our present
judgement that the best current models (not necessarily Equation 3-25) for

66

bound-bound emission, when integrated over a band of a few micrometers in width, are probably good to a factor of about 2 or 3.

Recommendations

Because of the importance of LWIR plasma radiation in a high-altitude nuclear environment, experimental verification of the theoretical models is certainly desirable. We would assign medium priority to this task, but would downgrade the necessity for it if a reasonably inexpensive method of verification cannot be found.

SECTION 4
SUMMARY AND RECOMMENDATIONS

This report attempts to provide a basis for establishing a priority listing of recommended work needed to improve our prediction capability for LWIR radiation in a nuclear environment. Based on the assumption that LWIR systems will operate mainly at tangent altitudes above about 110 km, so as to avoid natural earth-limb obscuration, we have concentrated our efforts on estimating the spectral radiance induced by a single megaton-class high-altitude burst. The results are based largely on previous MHD/chemistry-code calculations performed at MRC. Included in the study is emission from O_3 and NO_2 chemiluminescence, from N_2O formed by the $N_2(A^3\Sigma) + O_2 \rightarrow N_2O + O$ reaction and excited by earthshine scatter, from CO_2 vibraluminescence, from uranium and fission-fragment oxides, and from plasma in the fireball plume. The extent to which the radiation from each species serves to degrade the ambient limb windows is first determined, and the associated uncertainties are noted. The relative importance of each species in affecting the limb-window regions is then determined. This information is used, in conjunction with the known uncertainties related to the emission properties of the species, to assign priorities to the uncertainties so that the required listing of recommended experiments, or other work, can be established.

Although this report deals only with the magnitude of the nuclear-induced limb radiance, any structure inherent in the emitting regions is of potential importance, especially to scanning systems. This fact is implicit in our ordering of the priorities that gives a relatively high rating to uncertainties associated with emission from ionized species that are likely to be striated along the earth's magnetic field. This does not necessarily

68

mean that spatial and/or temporal structure in the radiation from neutral species is unimportant; only that widespread structure, with scale sizes important to systems ($\lesssim 1$ km), has yet to be observed or theoretically proven to exist.

The most important single source of LWIR radiation in a high-altitude nuclear environment appears to be plasma emission from the fireball plume. In fact, for certain viewing aspects, the plasma limb radiance can completely dominate that from all molecular sources, at tangent altitudes above about 100 km, for tens of minutes after the burst. Furthermore, the emission should be structured, due to the striated nature of the plasma, and the outage region to systems may extend to altitudes of 2000 km or more. In the recommendations below, the only reason why top priority is not given to experiments related to plasma radiation is our belief that the uncertainties associated with its calculation are relatively minor compared to those for certain of the molecular species whose contribution to the limb radiance may also be important, albeit to a lesser degree.

In this report, as in the earlier one dealing with the SWIR (Reference 1-1), we have restricted ourselves primarily to uncertainties related to the chemical and optical properties of the disturbed air. We again point out that uncertainties in the calculated emission, resulting from incomplete knowledge of the phenomenology of nuclear burst-air interactions may, in some cases, dominate those considered here.

Specific recommendations for research items, independent of the difficulty or feasibility of implementing them, are listed below in order of priority.

1. For the purpose of determining LWIR excitation rates by earthshine scatter, measure the absorption oscillator strengths (vibrational f numbers) for the fundamental V-R

69

bands of UO_2^+, UO^+, and selected fission-fragment oxide ions from among the group ZrO_x^+, LaO_x^+, SmO_x^+, NdO_x^+, YO_x^+, CeO_x^+, PrO_x^+ ($x = 1,2$).

2. For the purpose of determining LWIR excitation rates by the solar pumping mechanism, measure the f number(s) for permitted electronic transitions, connected to the ground state by visible light absorption, for the same species listed in Item 1 above.

3. Perform laboratory experiments to measure the quenching rate of $N_2(A^3\Sigma)$ by atomic oxygen. This information is needed for a good determination of the N_2O build up in a nuclear environment.

4. Measure the spectral yield of LWIR photons from the reactions

$$NO + O(+M) \longrightarrow NO_2(+M)$$

$$NO + O_3 \longrightarrow NO_2 + O_2$$
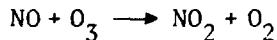
5. Provided a reasonably inexpensive method can be found, perform measurements to verify the theoretical models of bound-bound LWIR emission from a combining O^+/N^+ plasma.

6. Obtain laboratory confirmation of the tentative rate coefficient for the reaction $N_2(A^3\Sigma) + O_2 \rightarrow N_2O + O$.

7. Measure the wavelengths for the V-R bands of UO^+ and for the fission-fragment oxide ions listed in Item 1 above, especially for SmO_x^+ and NdO_x^+ ($x = 1,2$). This task would probably be accomplished as part of Item 1 above although the information is necessary only if the rates determined in Items 1 and 2 are significantly large, i.e., comparable to, or larger than, those for AℓO.

70

8. Using results of previous high-altitude multiburst calcula-
    tions, determine if burst-induced O_3 chemiluminescence and
    CO_2 vibraluminescence, at LWIR wavelengths, are ever
    important in a nuclear environment for limb-viewing systems
    at altitudes above 120 km.

9. The availability of spectroscopic data permitting, either
    (a) calculate the sunlight-pumping rate for the fundamental
    bands of N_2O or, (b) verify the unimportance of the process.

10. Perform sensitivity calculations to determine the uncertainty
    in the number of $N_2(A^3\Sigma)$ molecules formed per ion pair
    (following cascade), from electron bombardment, by utilizing
    the best current upper and lower limits on excitation cross
    sections for the relevant states of N_2, including $A^3\Sigma$, $B^3\Pi$,
    $C^3\Pi$, and $W^3\Delta$. This information is needed for a better
    assessment of the overall uncertainty in the N_2O emission
    prediction.

REFERENCES

1-1.   Archer, D. H., Requirements for Improved Infrared Prediction Capability, HAES Report No. 78, DNA 4585F, MRC-R-383, Mission Research Corporation, 30 April 1978.

2-1.   Degges, T. C., A High Altitude Infrared Radiance Model, AFCRL-TR-74-0606, Visidyne, Inc., 27 December 1974.

2-2.   Degges, T. C., and H. J. P. Smith, A High Altitude Infrared Radiance Model, AFGL-TR-77-0271, Visidyne, Inc., 30 November 1977.

2-3.   Proceedings of Second DNA Infrared Data Review Meeting, AFGL Technical Memorandum No. 17, Air Force Geophysics Laboratory, 10-12 April 1979.

2-4.   Nadile, R. M., Air Force Geophysics Laboratory, Private Communication, May 1980.

2-5.   CIRA 1972, Cospar International Reference Atmosphere, Akademie-Verlag, Berlin, 1972.

2-6.   Defense Nuclear Agency Reaction Rate Handbook (Second Edition), DNA 1948H, 30 April 1979.

2-7.   Park, J. H., Atlas of Infrared Absorption Lines, NASA Contractor Report 2925, November 1977.

3-1.   Zipf, E. C., AGU Transactions (EOS) 61, 325 (1980).

3-2.   Caledonia, G. E., HAES Infrared Data Review, AFGL-OP-TM-05, Vol. I, Meeting at Falmouth, Mass., 13-15 June 1977.

3-3.   Vallance Jones, A., and R. L. Gattinger, J. Geophys. Res. 81, 497 (1976).

3-4.   Dreyer, J. W., et al., J. Chem. Phys. 61, 3164 (1974).

3-5.   Kaufman, F., DNA-AFGL Nuclear Weapons Effects Chemistry Conference, 26 and 27 June 1980, Air Force Geophysics Laboratory.

3-6.   Hudson, R. D., Critical Review of Ultraviolet Photoabsorption Cross Sections for Molecules of Astrophysical and Aeronomic Interest, NSRDS-NBS 38, National Bureau of Standards, August 1971.

3-7.   Herzberg, G., Electronic Spectra of Polyatomic Molecules,
        Van Nostrand Reinhold Company, 1966.

3-8.   Cartwright, D. C., et al., Phys. Rev. A 16, 1041 (1977).

3-9.   Stair, A. T., et al., Proceedings of Second DNA Infrared Data
        Review Meeting, Volume III, AFGL-TM-18, Air Force Geophysics
        Laboratory, 10-12 April 1979.

3-10.   Kumer, J. B., HAES Infrared Data Review Meeting, AFGL-OP-TM-05,
        Vol. II, Meeting at Falmouth, Mass., 13-15 June 1977.

3-11.   James, T. C., Laboratory Investigation of Infrared Fluorescence
        of CO_2, HAES Report No. 69, DNA 4238F, Lockheed Palo Alto
        Research Laboratory, December 1976.

3-12.   James, T. C., and J. B. Kumer, J. Geophys. Res. 78, 8320 (1973).

3-13.   Kumer, J. B., Further Evaluation of ICECAP Auroral 4.3 µm Zenith
        Radiance, HAES Report No. 57, DNA 4260F, Lockheed Palo Alto
        Research Laboratory, October 1976.

3-14.   Kumer, J. B., J. Geophys. Res. 82, 2203 (1977).

3-15.   Gilmore, F. R., Proceedings of the DNA Infrared Program Meeting
        at the Naval Research Laboratory, 23-24 January 1980.

3-16.   Zel'dovich, Ya. B., and Yu. P. Raizer, Physics of Shock Waves and
        High Temperature Hydrodynamic Phenomena, Academic Press
        New York, 1966.

3-17.   Sappenfield, Dale, Radiation From a Recombining Oxygen Plasma,
        Los Alamos Scientific Laboratory, LA-4303 Supplement, April 1971.

3-18.   Sappenfield, Dale, Mission Research Corporation, Private
        Communication, July 1980.

3-19.   Oran, E. S., et al., Departure from LTE in an Oxygen Plasma I.
        Radiative Cascade Limit, Naval Research Laboratory Memorandum
        Report 2577, June 1973.

3-20.   Julienne, P. S., and J. Davis, Departure from LTE in an Oxygen
        Plasma II. Collisional-Radiative Model, Naval Research
        Laboratory Memorandum Report 2740, March 1974.

APPENDIX A
OZONE CHEMILUMINESCENCE IN NUCLEAR ENVIRONMENT

The chemiluminescent emission from ozone is based on the following considerations. We assume vibrational excitation of O_3 by the reaction

$$O + O_2 + M \xrightarrow{k_1} O_3^{\ddagger} + M \qquad , \qquad \text{(A-1)}$$
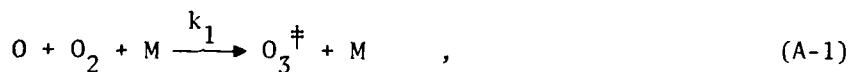
followed by radiative cascade

$$O_3^{\ddagger} \xrightarrow{A} O_3 + h\nu(\text{LWIR}) \qquad \text{(A-2)}$$
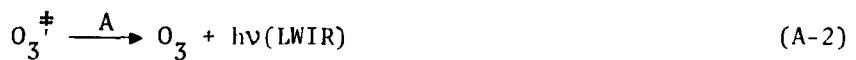
and quenching of the excited $O_3^{\ddagger}$ by

$$O_3^{\ddagger} + M \xrightarrow{k_q} O_3 + M \qquad . \qquad \text{(A-3)}$$

The spectral photon emission rate, $dI_\phi/d\ell$, at a wavelength λ_μ (micrometers), is then

$$\frac{dI_\phi}{d\ell} = Q\eta_{\lambda_\mu} k_1 [O][O_2](M) \qquad (\text{photons cm}^{-3} \text{ sec}^{-1} \text{ } \mu m^{-1}) \quad \text{(A-4)}$$

where Q is a quenching factor and η_{λ_μ} is the number of photons emitted per micrometer, at wavelength λ_μ, per reaction. Alternatively, the spectral volume emission rate can be expressed as

$$\left(\frac{dI_{\lambda_\mu}}{d\ell}\right)_{O_3} = 1.58 \times 10^{-20} \, Q \, \frac{\eta_{\lambda_\mu}}{\lambda_\mu} k_1 [O][O_2][M] \quad (\text{watts cm}^{-3} \text{ ster}^{-1} \text{ } \mu m^{-1}) \quad .$$

$$\text{(A-5)}$$

The spectral intensity (for optically thin radiation) is then just the line integral along the sight path:

$$I_{\lambda_\mu} = \int\limits_{\text{sight path}} \left(\frac{dI_{\lambda_\mu}}{d\ell}\right) d\ell \qquad \text{(watts cm}^{-2}\text{ ster}^{-1}\text{ }\mu\text{m}^{-1}) \quad . \qquad \text{(A-6)}$$

The quenching factor is taken to be

$$Q = \frac{A}{A + k_q [M]} \quad , \qquad \qquad \text{(A-7)}$$

where A is the radiative transition rate and k_q the quenching rate coefficient for Reaction A-3. For all relevant vibrational states of O_3 we have taken Q to be the same as that for the (101) state, which is obtained from Equation A-7 by setting $A = 15 \text{ sec}^{-1}$ (Reference A-1), $k_q = 2 \times 10^{-14} \text{ cm}^3 \text{ sec}^{-1}$ (Reference A-2), and replacing [M] by $([N_2] + [O_2])$. The nuclear burst calculations were performed using a rate coefficient for Reaction A-1 of $5.5 \times 10^{-34} (300/T)^{2.5} \text{ cm}^6 \text{ sec}^{-1}$.

The values assumed for η_{λ_μ} are shown in Figure A-1. They are those used in the WOE code (Reference A-3) for a temperature of 300 °K and are based largely on theoretical considerations of energy conservation augmented by very limited experimental data.

MHD/chemistry-code calculations have been used to calculate the limb radiance from O_3 chemiluminescence induced by a megaton-class, high-altitude burst. An example of the results, for certain peak values of the spectral limb radiance at 60 sec after burst, as functions of the tangent altitude of the sight path, is shown in Figure A-2.
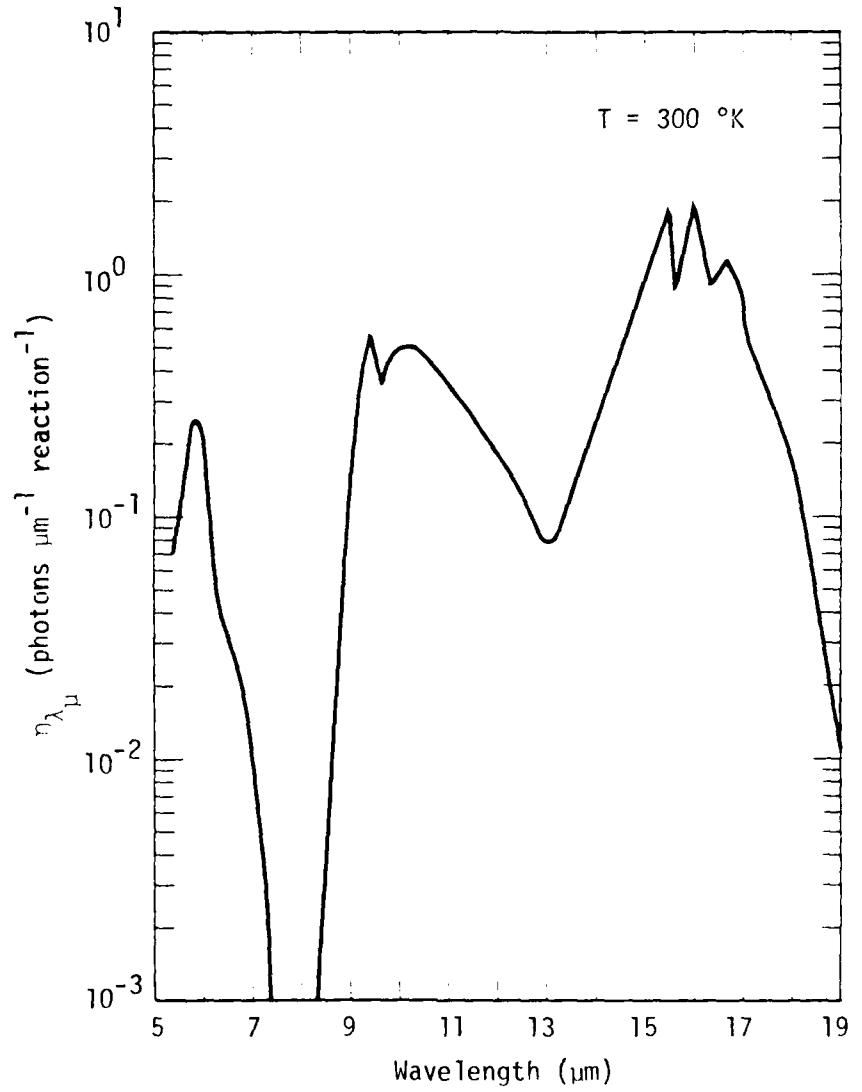
Figure A-1.   Assumed O_3 chemiluminescent spectrum from the
reaction $O + O_2 + M \rightarrow O_3 + M$ (as used by WOE code,
Reference A-3).
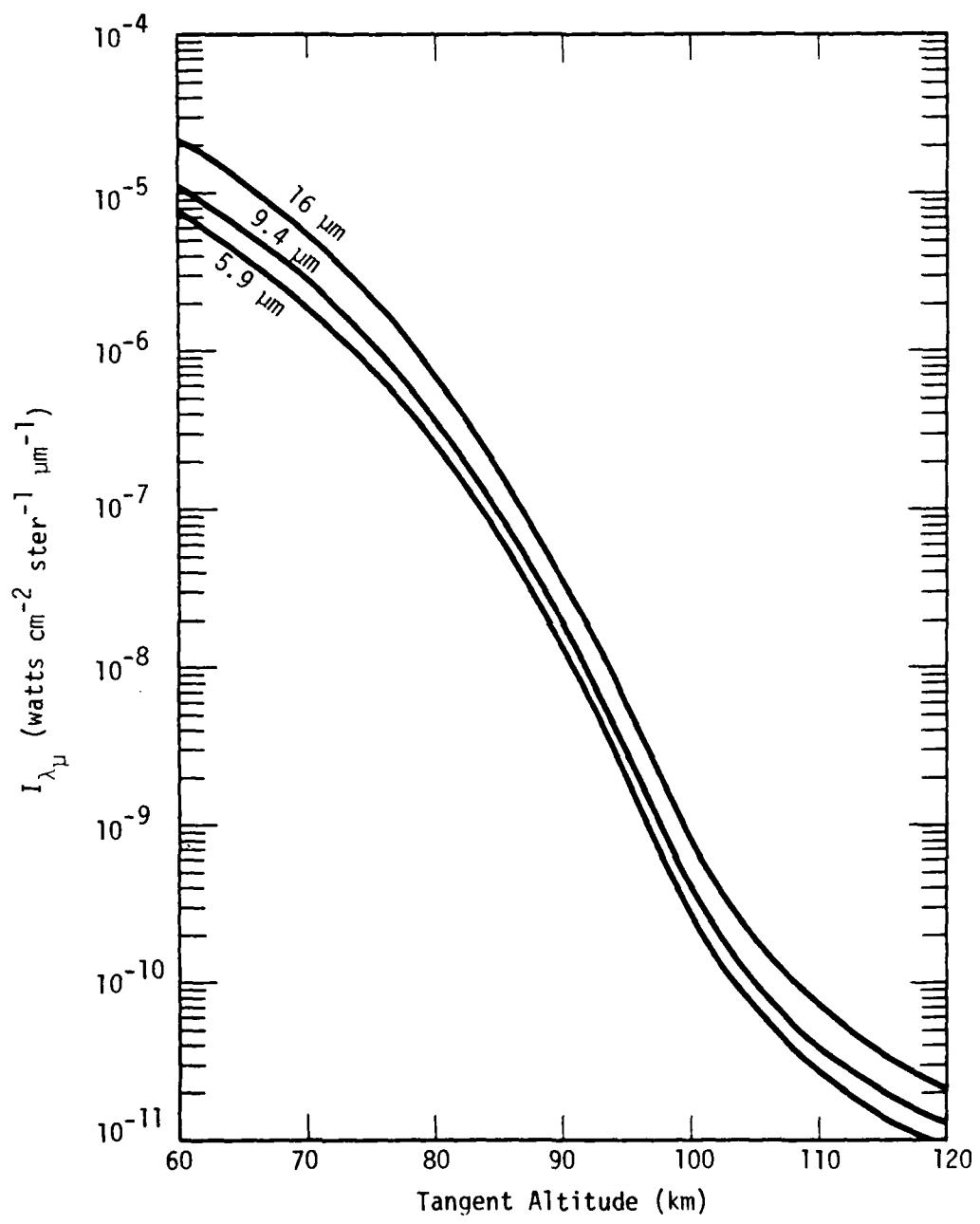
Figure A-2. Calculated peak spectral limb radiance from O_3 chemiluminescence induced at 60 sec after a megaton-class high-altitude burst.

APPENDIX B
NO$_2$ CHEMILUMINESCENCE IN NUCLEAR ENVIRONMENT

The chemiluminescent emission from NO$_2$ is assumed to be produced by the reactions

$$NO + O + M \xrightarrow{k_1} NO_2 + M \qquad (B-1)$$

$$NO + O \xrightarrow{k_2} NO_2 + h\nu \qquad (B-2)$$

$$NO + O_3 \xrightarrow{k_3} NO_2 + O_2 \quad . \qquad (B-3)$$
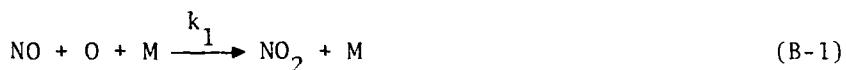
The spectral volume emission rate can thus be written (by analogy with Equation A-5 for the case of O$_3$) as

$$\left(\frac{dI_{\lambda_\mu}}{d\ell}\right)_{NO_2} = 1.58 \times 10^{-20} \frac{Q}{\lambda_\mu} \left\{ \eta_{\lambda_\mu}(1)k_1[NO][O][M] + \eta_{\lambda_\mu}(2)k_2[NO][O] \right.$$
$$\left. + \eta_{\lambda_\mu}(3)k_3[NO][O_3] \right\} \text{(watts cm}^{-3}\text{ ster}^{-1}\text{ }\mu\text{m}^{-1})$$
$$(B-4)$$

where $\eta_{\lambda_\mu}(1)$, $\eta_{\lambda_\mu}(2)$, $\eta_{\lambda_\mu}(3)$ and k_1, k_2, k_3 are the photon efficiencies and rate constants, respectively, for Reactions B-1, B-2, and B-3. It turns out that Reactions B-1 and B-2 dominate Reaction B-3 at altitudes above about 70 km, and Reaction B-2 dominates Reaction B-1 above about 90 km.

The quenching factor, Q, for all relevant vibrational states of NO$_2$ is assumed equal to that for the (101) state, which is obtained from

Equation A-7 by setting $A = 128 \, \text{sec}^{-1}$* (References B-1, B-2, B-3), and replacing $k_q[M]$ by $(10^{-13}[N_2] + 3 \times 10^{-13}[O_2] + 9.1 \times 10^{-12}[O])$ (Reference B-4).

Values adopted for the rate coefficients k_1, k_2, and k_3 are $1.6 \times 10^{-32} \, e^{584/T} \, \text{cm}^6 \, \text{sec}^{-1}$, $6.3 \times 10^{-17} \, (300/T)^{1.94} \, \text{cm}^3 \, \text{sec}^{-1}$, and $2.1 \times 10^{-12} \, e^{-1450/T} \, \text{cm}^3 \, \text{sec}^{-1}$, respectively, where T is the temperature in °K.

The values assumed for the photon efficiences are shown in Figure B-1. They are those used in the WOE code (Reference A-3) for a temperature of 300 °K and are based on theoretical considerations of energy conservation. No experimental data are known to us.

The spectral radiance along a sight path is determined from Equations A-6 and B-4.

MHD/chemistry-code calculations have been used to determine the limb radiance from NO_2 chemiluminescence induced by a megaton-class high-altitude burst. An example of the results, for certain peak values of the spectral limb radiance at 60 sec after burst, as functions of the tangent altitude of the sight path, is shown in Figure B-2.

---

* Sum of the A values for transitions (101-000), (101-001), (101-100).
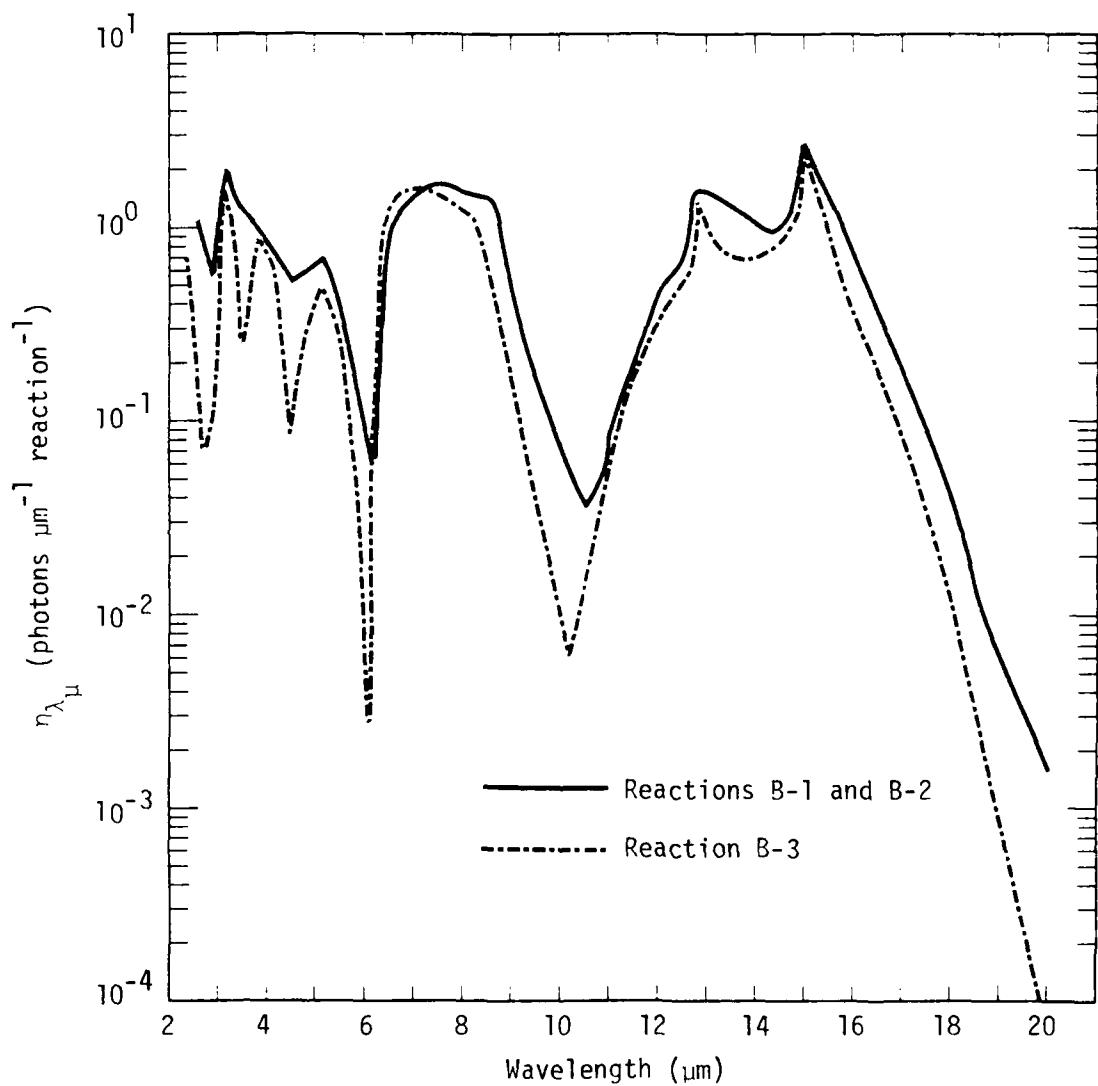
Figure B-1. Assumed NO_2 chemiluminescent spectrum from the reactions $NO + O(+M) \rightarrow NO_2(+M)$ and $NO + O_3 \rightarrow NO_2 + O_2$ (as used by WOE code, Reference A-3).
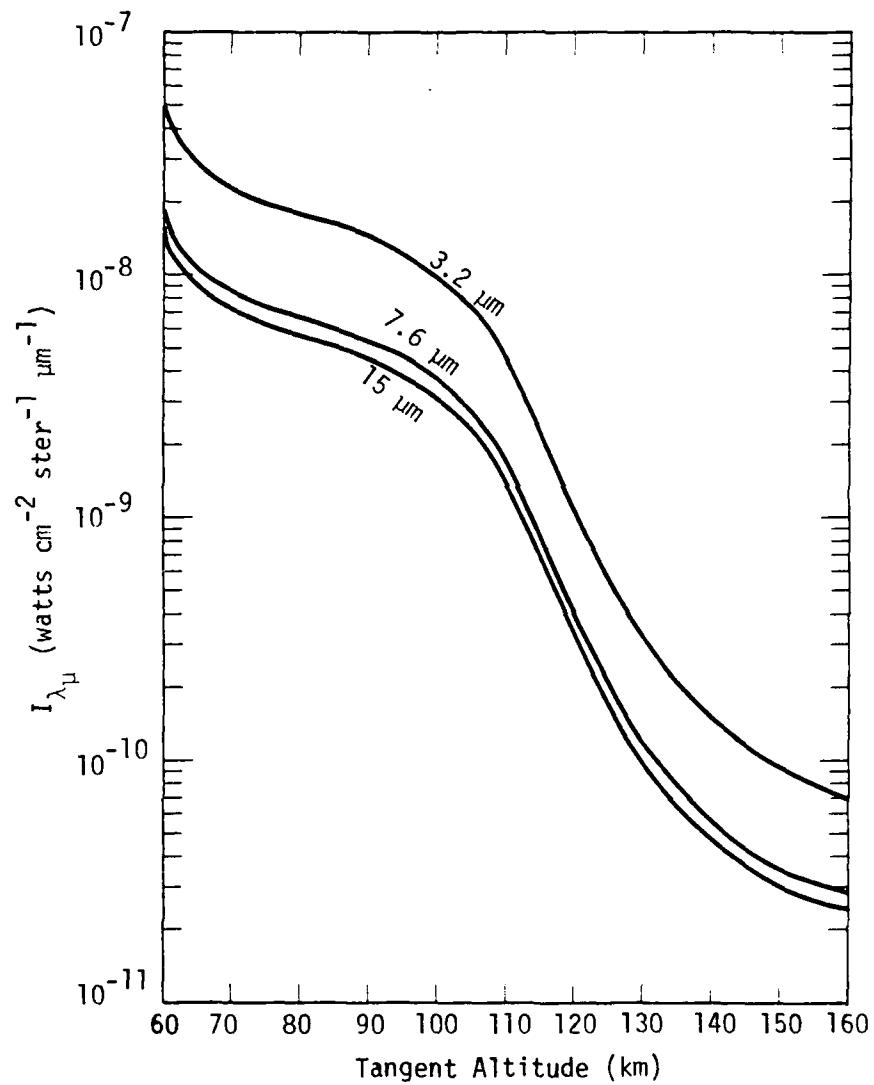
Figure B-2. Calculated peak spectral limb radiance from NO_2 chemiluminescence induced at 60 sec after a megaton-class high-altitude burst.

APPENDIX C

EARTHSHINE SCATTER EXCITATION OF N_2O FUNDAMENTAL BANDS IN A NUCLEAR ENVIRONMENT

In this appendix we develop the values for f_{λ_μ}, appearing in Equation 3-12, used for determining the spectral intensity of earthshine scatter from N_2O formed in a nuclear environment by the reaction $N_2(A^3\Sigma) + O_2 \rightarrow N_2O + O$. Also given is an example of the peak limb radiance calculated for a time of 3 sec following a megaton-class, high-altitude burst.

The quantity f, the number of photons emitted per molecule per sec per micrometer by earthshine scatter excitation, can be written as

$$f_{\lambda_\mu} = \xi_{\lambda_\mu} \dot{\phi}_e \quad , \tag{C-1}$$

where $\dot{\phi}_e$ is the photon emission rate per molecule for an entire V-R band, and ξ_{λ_μ} is a spectral shape factor that distributes the photons in wavelength over the band. For a molecule imbedded in a radiation field of energy density ρ_ν, $\dot{\phi}_e$ is given by (Reference C-1, p. 372)

$$\dot{\phi}_e = \frac{\pi e^2 f_{o1}}{mh\nu} \rho_\nu \tag{C-2}$$

where f_{o1} is the absorption oscillator strength, $h\nu$ is the photon energy, and e and m are the electron charge and mass, respectively. But ρ_ν is related to the intensity, I_ν, of the radiation field by

$$\rho_\nu = \frac{1}{c} \int I_\nu d\Omega \tag{C-3}$$

where the integral is taken over all solid angles. However, since earth-shine is only upwelling we have

$$\rho_\nu = \frac{2\pi}{c} I_\nu \qquad\qquad (C-4)$$

In terms of the wavelength, λ_μ, in micrometers, and the earthshine intensity, $I^e_{\lambda_\mu}$, in watts cm^{-2} $ster^{-1}$ μm^{-1}, Equations C-2 and C-4 can be combined to yield

$$\dot{\phi}_e = 2.8 \times 10^3 f_{o1} \lambda_\mu^3 I^e_{\lambda_\mu} \quad \text{(photons molecule}^{-1} \text{ sec}^{-1}) \qquad (C-5)$$

or, alternatively, in terms of the integrated band absorption coefficient, S_o, in units of cm^{-2} atm^{-1},

$$\dot{\phi}_e = 1.2 \times 10^{-4} S_o \lambda_\mu^3 I^e_{\lambda_\mu} \quad \text{(photons molecule}^{-1} \text{ sec}^{-1}) . \qquad (C-6)$$

The maximum intensity of upwelling earthshine radiation above 100-km altitude at the wavelengths of the ν_1, ν_2, and ν_3 bands of N_2O has been obtained from recent LOWTRAN 5 code calculations (Reference C-2). These results, together with values for S_o and λ_μ for the three funda-mentals of N_2O, and the calculated values for $\dot{\phi}_e$, are shown in Table C-1.

Table C-1. Calculated earthshine scatter rate for the three fundamentals of N_2O

BAND	λ_μ (μm)	S_o ($cm^{-2} atm^{-1}$)	$I^e_{\lambda_\mu}$ (watts cm^{-2} $ster^{-1}$ μm^{-1})	$\dot{\phi}_e$ (photons molecule^{-1} sec^{-1})
ν_1	7.8	268	5.1×10^{-4}	7.7×10^{-3}
ν_2	17.0	37	2.9×10^{-4}	6.3×10^{-3}
ν_3	4.5	1500	1.4×10^{-5}	2.3×10^{-4}

The band shape factors, ξ_{λ_μ}, appearing in Equation C-1 for a temperature of 300 °K, are shown in Figure C-1. They were obtained using data from References C-3 and C-4.

Figure C-2 shows the estimated column number of N_2O molecules along tangent paths at 3 sec following a megaton-class, high-altitude burst. These results are based on the assumption of one $N_2(A^3\Sigma)$ molecule formed per initial ion pair (except in the dissociated-fireball region) which probably yields an upper-limit estimate for the N_2O concentration since recent calculations (Reference C-5) give a value of about 0.4 A-state molecules formed per ion pair (including cascade effects) for the X-ray deposition region.*

Equation 3-12, together with the results shown in Table C-1 and Figures C-1 and C-2, were used to calculate the peak spectral limb radiance as a function of tangent altitude. The results, for the three N_2O fundamentals, are shown in Figure C-3.

---

* For the UV-deposition region, however, the value calculated in Reference C-6 is approximately 0.6.
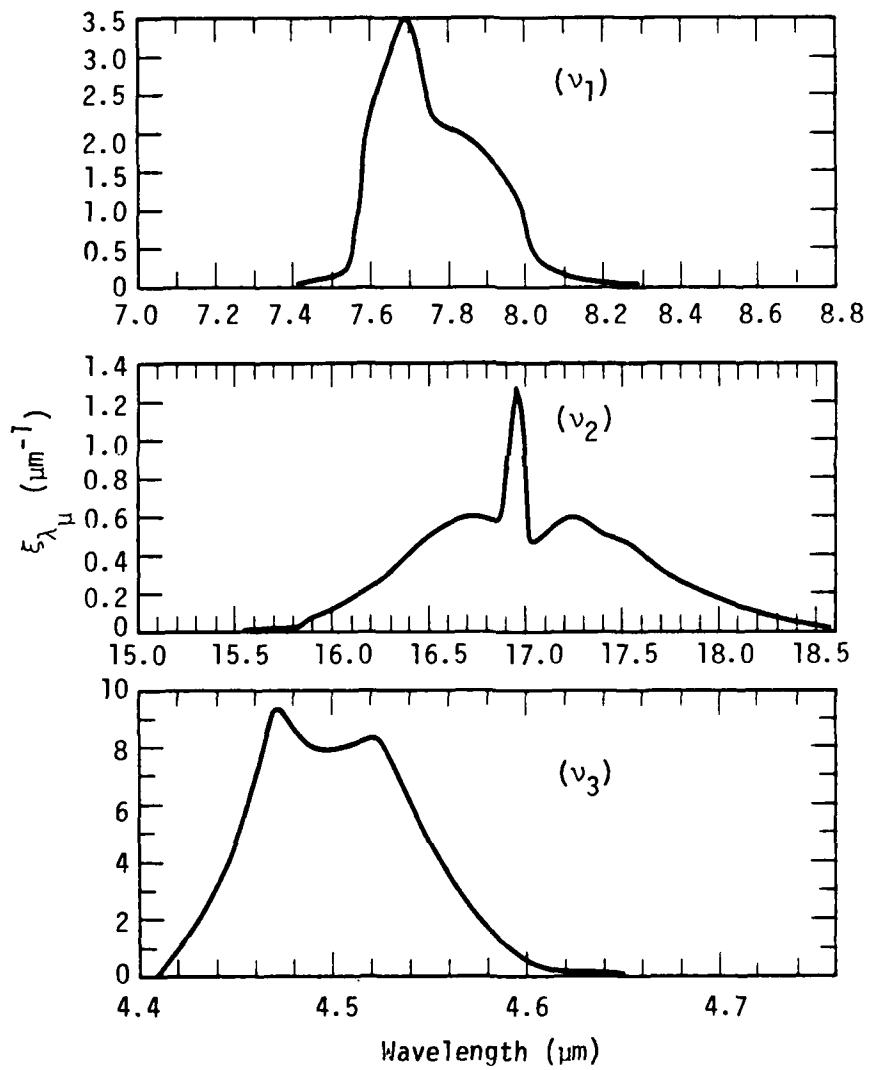
Figure C-1. Band shape factors at 300 °K for the three fundamentals of N_2O.
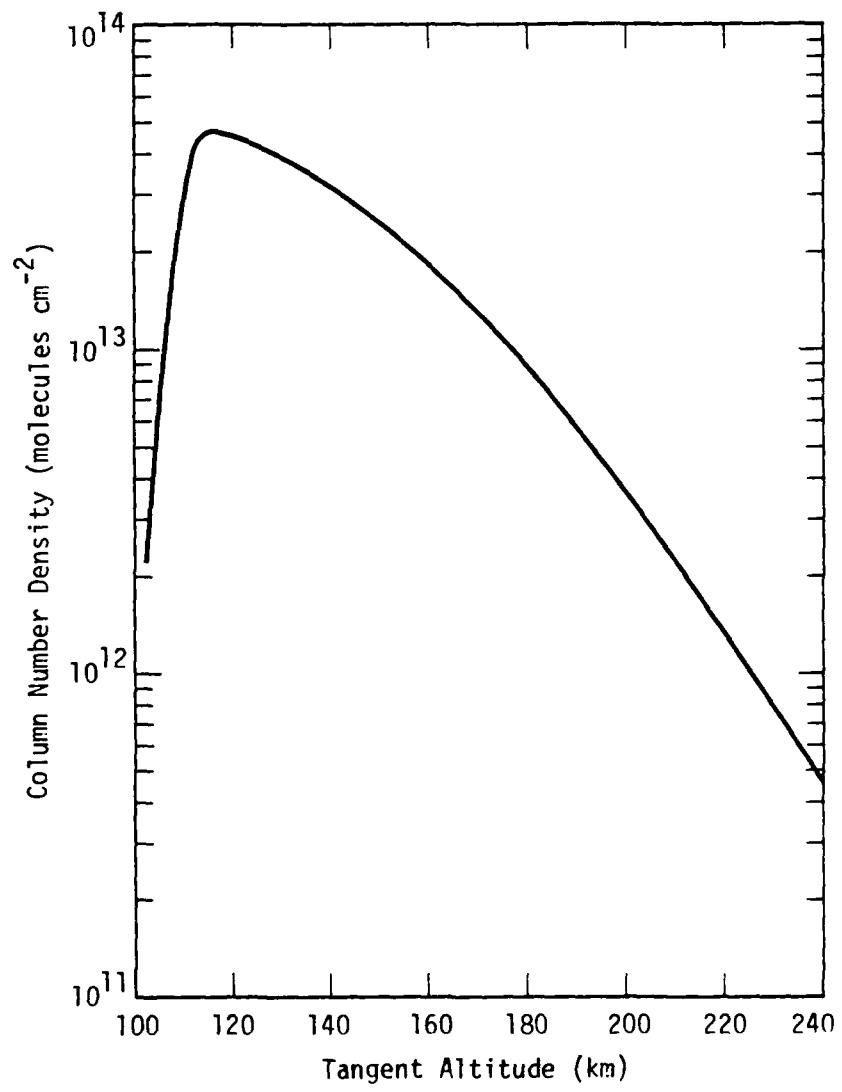
Figure C-2. Estimated column number density of N_2O molecules along tangent paths at 3 sec after a megaton-class high-altitude nuclear burst.
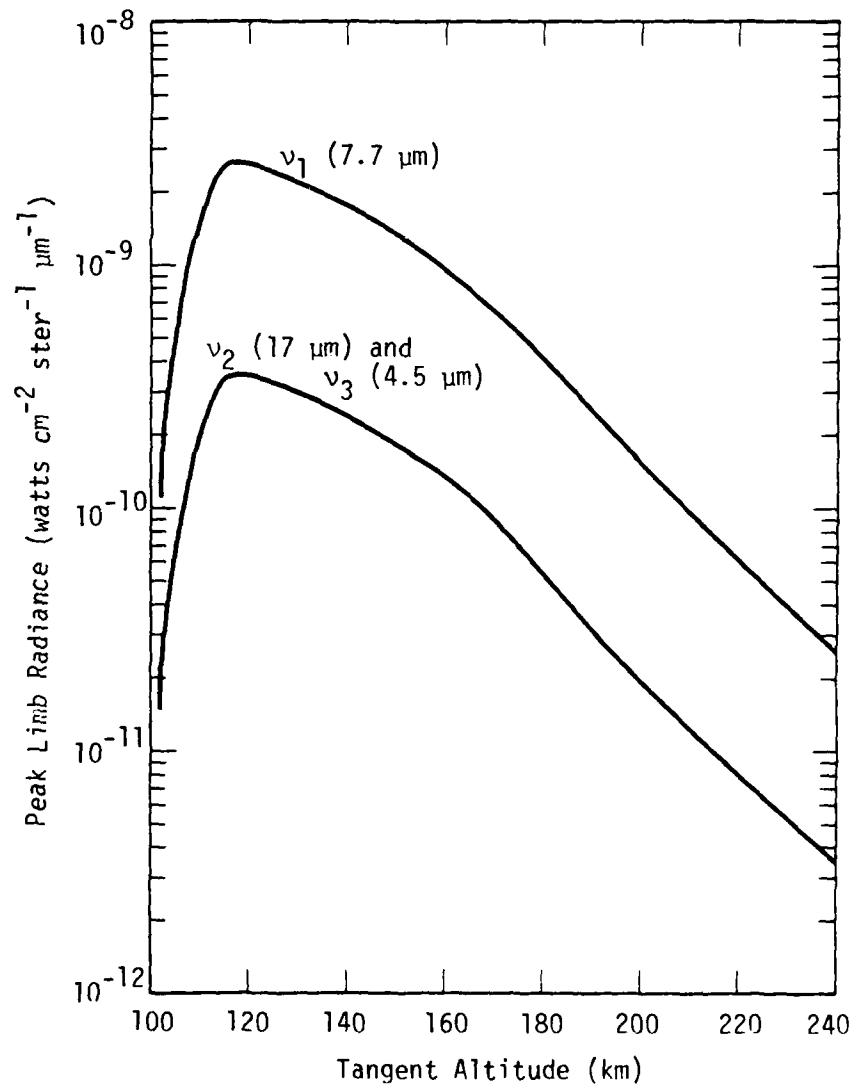
Figure C-3. Estimated peak spectral limb radiance in the ν_1, ν_2, and ν_3 bands of N_2O excited by earthshine scatter at 3 sec following a megaton-class high-altitude nuclear burst.

APPENDIX D
CO$_2$ VIBRALUMINESCENCE IN NUCLEAR ENVIRONMENT

In this appendix we describe the simple model used to determine the magnitude of CO$_2$ vibraluminescence above 100 km in a nuclear environment, and show estimates of the peak limb radiance at 60 sec following a megaton-class high-altitude burst.

The vibrational transitions in CO$_2$ that give rise to the bands of interest here are shown in Figure D-1. Also shown is the v = 1 state of
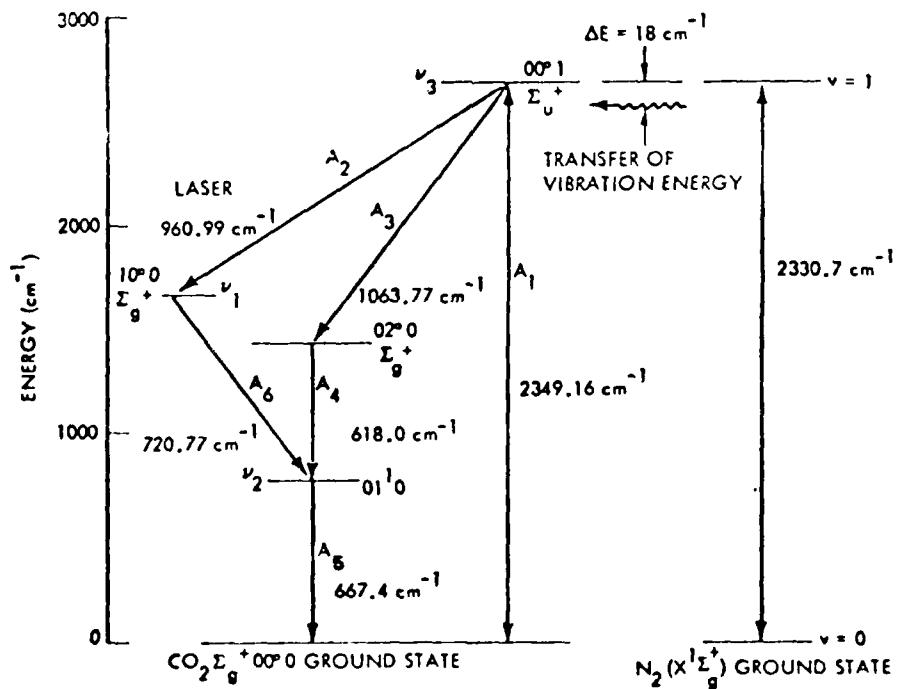
Figure D-1. Lower vibrational level scheme for CO$_2$ and N$_2$ molecules.

N_2 that is nearly energy resonant with the $00^\circ1$ state of CO_2 which can readily be excited by the vibrational transfer reaction

$$N_2(1) + CO_2(00^\circ0) \xrightarrow[k_1']{k_1} N_2(0) + CO_2(00^\circ1) \quad . \qquad \text{(D-1)}$$
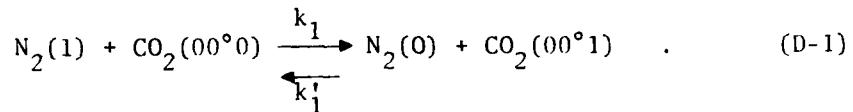
N_2 is vibrationally excited directly by the primary and secondary photo-electrons following X-ray and UV-energy deposition and also by certain chemical reactions. After energy transfer to CO_2 has occurred, the $(00^\circ1)$ state of CO_2 can decay by radiation to the $(00^\circ0)$, $(10^\circ0)$, and $(02^\circ0)$ states with emission of bands at 4.3, 10.4, and 9.4 μm, respectively. The corresponding transition probabilities are designated A_1, A_2, and A_3. Subsequent cascade from the $(10^\circ0)$ and $(02^\circ0)$ states leads to radiation at 13.8, 16.2 and 15 μm.

A quasi equilibrium between excitation and deexcitation is rapidly established so that the $CO_2(00^\circ1)$ concentration is given by

$$[CO_2(00^\circ1)] \approx \frac{k_1 [CO_2][N_2(1)]}{A_1 + A_2 + A_3 + k_1'[N_2]} \qquad \text{(D-2)}$$

where k_1 and k_1' (approximately equal) are, respectively, the rate coefficients for the forward and reverse Reactions D-1. The volume emission rate, $dI_{4.3}/d\ell$, integrated over the entire 4.3-μm band, is determined by

$$\frac{dI_{4.3}}{d\ell} = 3.7 \times 10^{-21} A_1 [CO_2(00^\circ1)] \quad \text{(watts cm}^{-3}\text{ ster}^{-1}\text{)} \quad \text{(D-3)}$$

and the band intensity, $I_{4.3}$, is given by the line integral

$$I_{4.3} = \int_{\text{sight path}} \left(\frac{dI_{4.3}}{d\ell}\right) d\ell \qquad \text{(watts cm}^{-2}\text{ ster}^{-1}\text{)} \quad . \quad \text{(D-4)}$$

The spectral intensity, I_{λ_μ}, for any wavelength, λ_μ, can readily be shown to be determined from the equation

$$I_{\lambda_\mu} = \frac{4.3}{\lambda_\mu} \eta_{\lambda_\mu} I_{4.3} \qquad \text{(watts cm}^{-2}\text{ ster}^{-1}\text{ }\mu\text{m}^{-1}) \qquad \text{(D-5)}$$

where η_{λ_μ} is the number of photons emitted per Reaction D-1 per micrometer at wavelength λ_μ.

Figures D-2a and D-2b show values for η_{λ_μ}, adopted from the WOE code (Reference A-3), that include contributions from the 6 bands of CO_2 mentioned above. The values are given for temperatures of 300 °K and 3000 °K although only the 300 °K results have been used in this report. Collisional quenching of the excited states, not included in these results, is not significant at altitudes above about 100 km, where our main interest lies.

MHD/chemistry-code calculations were used to calculate the quantity $I_{4.3}$ along limb paths following a megaton-class, high-altitude burst. An example of the results, for a time of 60 sec, is shown in Figure D-3. The results in Figures D-2 and D-3 have been used in Equation D-5 to determine the peak spectral limb radiance at 60 sec as a function of the tangent altitude of the sight path. The results are shown in Figure D-4.
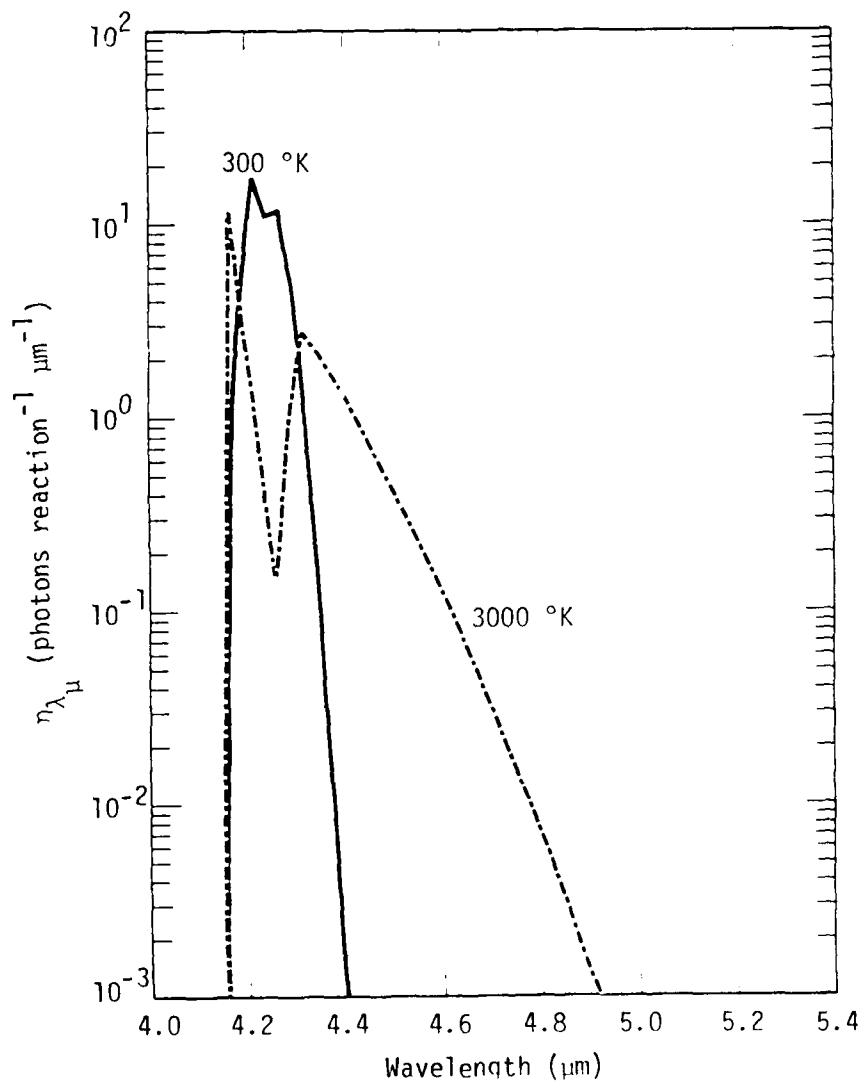
Figure D-2a. Assumed CO_2 vibraluminescence spectrum (as used by WOE code, Reference A-3).
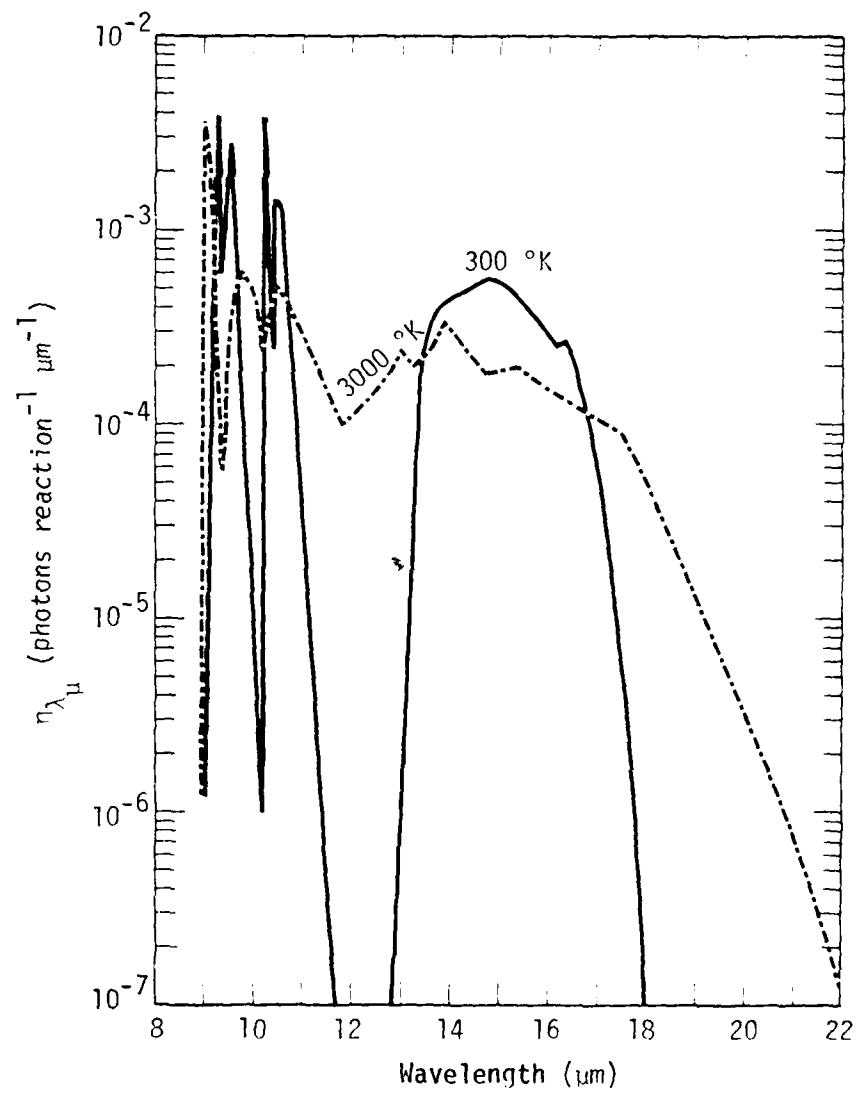
Figure D-2b. Assumed CO_2 vibraluminescence spectrum (as used by WOE code, Reference A-3).
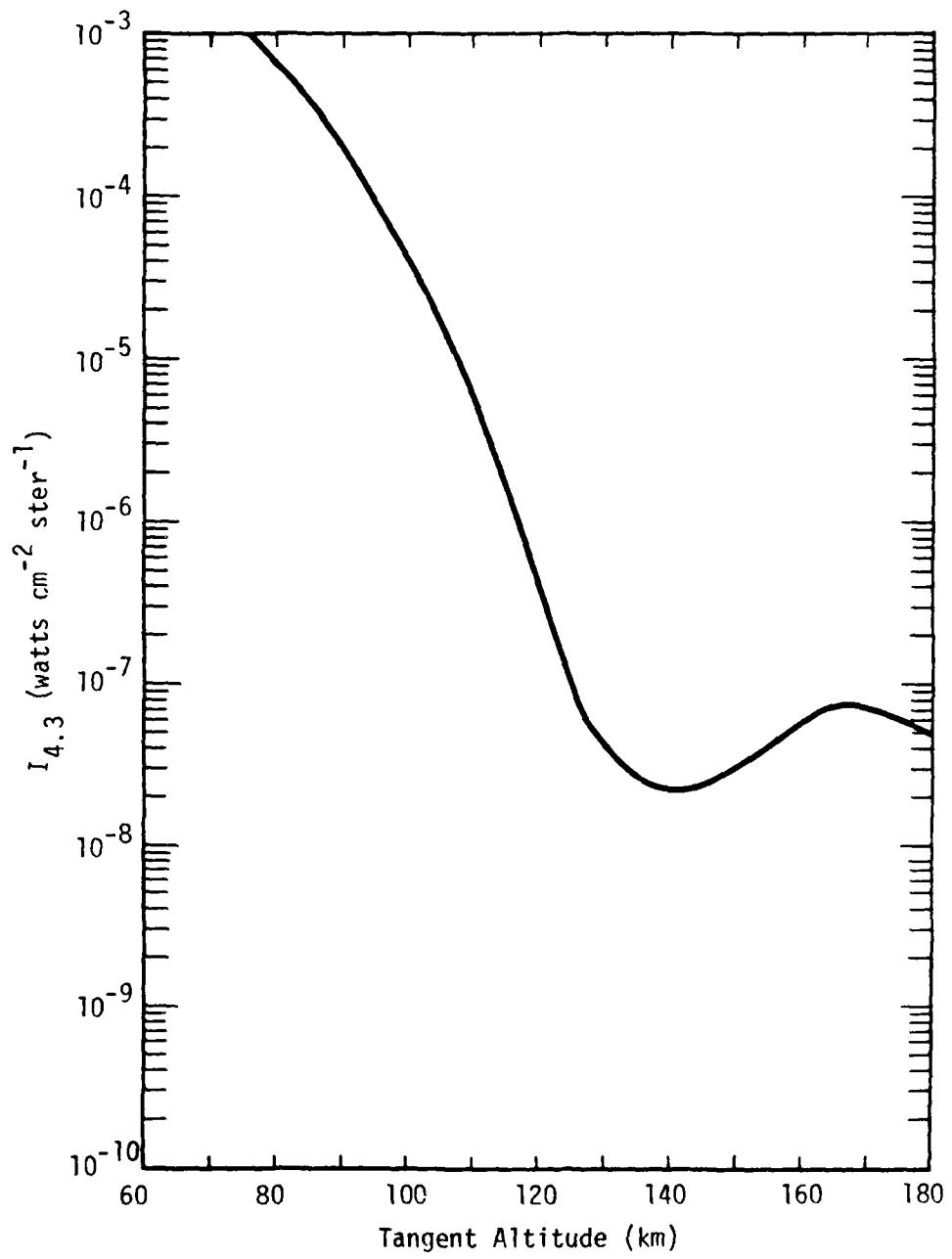
Figure D-3. Calculated limb radiance in 4.3-μm band from CO_2 vibraluminescence at 60 sec after a megaton-class high-altitude burst.
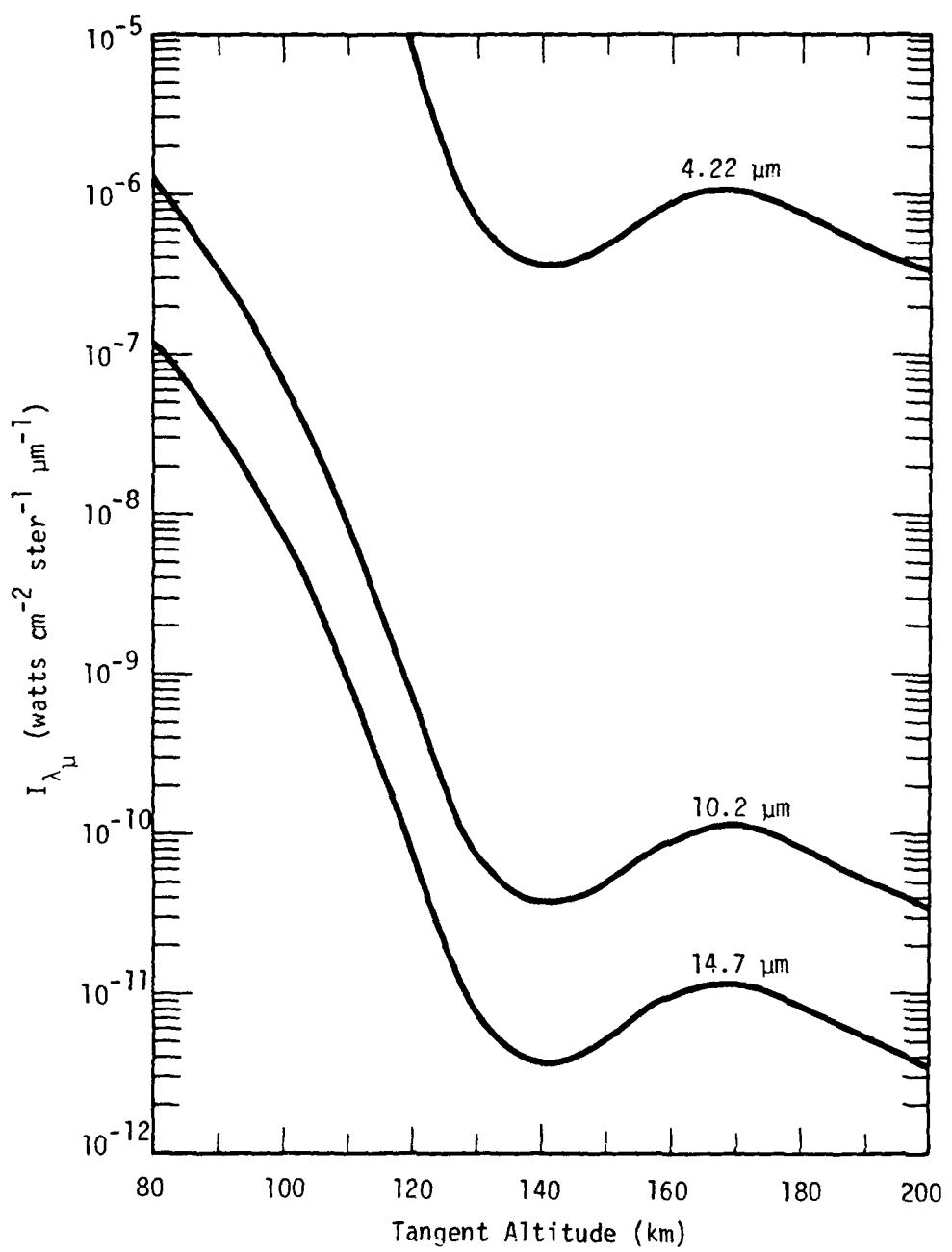
Figure D-4. Calculated peak spectral limb radiance from CO_2 vibraluminescence at 60 sec after a megaton-class high-altitude burst.

APPENDIX E

LWIR RADIATION FROM URANIUM- AND FISSION-FRAGMENT OXIDE IONS IN A NUCLEAR ENVIRONMENT

In this appendix we estimate the limb radiance from the fundamental bands of oxide ions of uranium and certain fission fragments formed following a megaton-class, high-altitude burst and excited by earthshine and sunlight scatter. Although the calculation is fraught with considerable uncertainty, particularly with respect to the photon excitation rates of the oxide ions, the results should serve to point up the potential importance of these sources of LWIR radiation and the need for additional experimental data.

The oxide ions specifically included are UO^+, UO_2^+, and fission-fragment (FF) oxides FFO^+, FFO_2^+ where FF includes the species Zr, La, Sm, Nd, Y, Ce, and Pr. The atomic ions for each of these species can react rapidly with O_2 to form oxide ions, the reactions being considerably exothermic. We will use the shorthand MeO_x^+ to refer to these oxide ions (x = 1,2).

EXCITATION AND RADIANCE CONSIDERATIONS

Once formed, the fundamental vibration-rotation (V-R) bands of MeO_x^+ can be continuously excited by earthshine scatter and, possibly, by solar pumping in the daytime. Let $\dot{\phi}_e$ and $\dot{\phi}_s$ be the rates for these two processes, respectively. The limb radiance (in the rectangular-band approximation) can then be expressed as

$$I_{\lambda_\mu} = 1.58 \times 10^{-20} \frac{(\dot{\phi}_e + \dot{\phi}_s)}{\lambda_\mu \Delta\lambda_\mu} \int_{\text{sight path}} [MeO_x^+] d\ell \qquad \text{(watts cm}^{-2}\text{ ster}^{-1}\text{ }\mu\text{m}^{-1}) \qquad \text{(E-1)}$$

97

where $\Delta\lambda_\mu$ is the effective bandwidth of the radiation. At nighttime, $\dot{\phi}_s = 0$. The rates $\dot{\phi}_e$ and $\dot{\phi}_s$ for MeO_x^+ are not known. However, for calculational purposes, we will assume values for them equal to those for AℓO, which will now be considered.

Earthshine Excitation Rate ($\dot{\phi}_e$) for AℓO

$\dot{\phi}_e$ can be determined from Equation C-5. For the fundamental band of AℓO, $S_o = 1650$ (Reference E-1), $\lambda_\mu = 10.4$, and $I_{\lambda_\mu}^e \approx 9.2 \times 10^{-4}$ (Reference C-2). Equation C-5 then leads to the result

$$\dot{\phi}_e(AℓO) = 0.2 \quad \text{(photons molecule}^{-1} \text{ sec}^{-1}) \tag{E-2}$$

Solar Pumping Rate ($\dot{\phi}_s$) for AℓO

The mechanism here is one whereby a molecule in its ground electronic and vibrational state is first raised to an excited electronic state by visible light absorption. Subsequently, following radiative cascade back to the ground electronic state with emission of a visible photon, the molecule will generally be left in a vibrationally excited state which may then be deexcited by the emission of LWIR photons. Specifically, for AℓO, the process can be described by the sequence

$$AℓO(X^2\Sigma^+; 0) + h\nu(\approx 4800\overset{\circ}{A}) \longrightarrow AℓO(B^2\Sigma^+; v') \longrightarrow AℓO(X^2\Sigma^+; v'') + h\nu(\sim 1800\overset{\circ}{A})$$

$$AℓO(X^2\Sigma^+; v'') \longrightarrow AℓO(X^2\Sigma^+; v'' -1) + h\nu(10.4 \ \mu m)$$
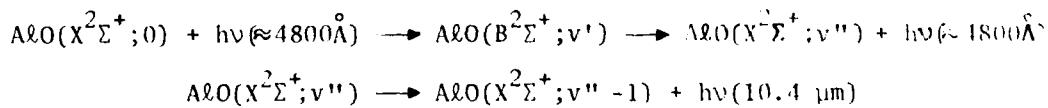
which involves excitation of the $B^2\Sigma^+$ state by absorption (and subsequent reemission) of $4800\overset{\circ}{A}$ solar photons.

It can be shown (Reference C-1, p. 382) that

$$\dot{\phi}_s = \frac{\pi e^2}{mc} \eta \mathscr{I}_\nu f_{X \to B} \tag{E-3}$$

98

where η is the number of IR photons emitted per visible photon absorbed, $\mathscr{F}_\nu$ is the photon flux (photons cm^{-2} sec^{-1} $(\Delta\nu)^{-1}$), and $f_{x\to B}$ is the f number for the electronic transition. For AℓO, we have $f_{x\to B} = 3 \times 10^{-2}$ (Reference E-2), and at 4800Å the solar flux is $\mathscr{F}_\nu \approx 400$. Thus, from Equation E-3,

$$\dot{\phi}_s/\eta \approx 0.32 \quad . \tag{E-4}$$

A value for η can be determined in terms of the Franck-Condon factors, $q_{v'v''}$, that give the relative transition probabilities between vibrational states of the upper and lower electronic states. To the extent that one allows only $\Delta v = 1$ transitions to occur (i.e., ignores overtone emission), so that a molecule left in the v'' state will emit (after cascade) v'' fundamental photons, then

$$\eta \approx \sum_{v'v''} v'' q_{ov'} q_{v'v''} \tag{E-5}$$

where v' and v'' are vibrational quantum numbers of the $B^2\Sigma^+$ and $X^2\Sigma^+$ electronic states, respectively. Equation E-5, with values for $q_{v'v''}$ from Reference E-3*, yields $\eta \approx 0.63$. From Equation E-4 we then obtain

$$\dot{\phi}_s(AℓO) \approx 0.2 \quad \text{(photons molecule}^{-1} \text{ sec}^{-1}) \quad , \tag{E-6}$$

which is the same as the emission rate $\dot{\phi}_e$ from earthshine.

For each fundamental band of the uranium and fission-fragment oxide ions there will be a value for $\dot{\phi}_e$ and for $\dot{\phi}_s$. If, for example, $\dot{\phi}_e^{ij}$ and $\dot{\phi}_s^{ij}$ are the values for the ith band of species j, whose

---

* In some of the older literature the $B^2\Sigma^+$ state of AℓO was designated as $A^2\Sigma^+$.

concentration is $[MeO_x^+]_j$, then, more accurately, Equation E-1 should be written as

$$I_{\lambda_\mu} = 1.58 \times 10^{-20} \sum_{i,j} \frac{(\dot{\phi}_e^{ij} + \dot{\phi}_s^{ij})}{\lambda_\mu^{ij} \Delta\lambda_\mu^{ij}} \int_{\text{sight path}} [MeO_x^+]_j \, d\ell \qquad \text{(E-7)}$$

where $\Delta\lambda_\mu^{ij}$ is the bandwidth of the ith fundamental of species j and λ_μ^{ij} is its mean wavelength. However, for simplicity, and lack of better knowledge, we will continue to use Equation E-1 and assume that 0.2 photons by night and 0.4 photons by day, of mean wavelength 11.5 μm, are emitted per sec from each UO_x^+ ion, uniformly over a band of width $\Delta\lambda_\mu = 2$ μm and, from each FFO_x^+ ion, uniformly over a band of width $\Delta\lambda_\mu = 4$ μm.

INITIAL VERTICAL DISTRIBUTION OF DEBRIS IONS

As explained in Section 3, we assume that the burst releases 7×10^{26} U^+ ions and 3×10^{26} fission-fragment ions (capable of forming oxide ions by reaction with O_2) in the downward hemisphere with the common velocity of 2×10^8 cm sec^{-1}. After interaction with the air ions (by means of the earth's magnetic field) these ions will have lost a considerable fraction of their initial kinetic energy and will be left with a distribution of velocities. An initial vertical distribution of debris-ion concentration will thus be established; the fastest moving ions being deposited at the lowest altitude possible; the slower ones, at the higher altitudes. The actual initial vertical distribution will depend directly on their velocity distribution immediately following their energy loss to the air ions. Two different cases have been considered: one where the initial velocity distribution, $N(v)$, varies as v^{-2}, and the other where the distribution is independent of v.

Case 1 (Distribution $\propto v^{-2}$)

In this case we have

$$N(v) = Kv^{-2} \tag{E-8}$$

where the constant K remains to be determined. To determine K, we assume we know both the total kinetic energy, $\mathscr{E}$, of the debris ions after the debris-air interaction has occurred, and also the total number, N, of debris ions. Thus, if v_o is the initial (and maximum) velocity of the ions, and v_{min} the minimum velocity,

$$\mathscr{E} = \int_{v_{min}}^{v_o} \frac{1}{2} Mv^2 N(v)dv = \frac{KM}{2}(v_o - v_{min}) \tag{E-9}$$

and

$$N = \int_{v_{min}}^{v_o} N(v)dv = K\left(\frac{1}{v_{min}} - \frac{1}{v_o}\right) \quad , \tag{E-10}$$

where M is the ion mass. Equations E-9 and E-10 can be solved for the unknowns K and v_{min} to yield the result

$$v_{min} = fv_o \tag{E-11}$$

$$K = Nv_o f/(1-f) \quad ; \qquad (0 < f < 1) \tag{E-12}$$

where f, given by

$$f = \mathscr{E}\Big/\left(\frac{1}{2} MNv_o^2\right) \quad , \tag{E-13}$$

is the fraction of the original kinetic energy that is retained by the debris ions. Thus,

$$N(v) = Nv_o \frac{f}{(1-f)} v^{-2} \quad . \tag{E-14}$$

In our calculations, we will consider cases where $f = 0.1$ and $1/3$.

Case 2 (Distribution Independent of v)

In this case,

$$N(v) = K_1 \tag{E-15}$$

Proceeding as in Case 1 above, we find

$$\mathscr{E} = \frac{K_1 M}{6} (v_o^3 - v_{min}^3) \tag{E-16}$$

and

$$N = K_1(v_o - v_{min}) \tag{E-17}$$

It turns out that a real solution for K_1 and v_{min}, with $v_{min} \geq 0$, exists only for values of $f \geq 1/3$. When $f = 1/3$, we obtain

$$v_{min} = 0 \tag{E-18}$$

$$N(v) = N/v_o \tag{E-19}$$

The initial vertical distribution, $N_i(z)$, of the atomic debris ions can be found in these two cases by considering the stopping altitude, z, in the atmosphere as a function of particle velocity, v. Specifically,

$$N_i(z) = N(v) \left| \frac{dv}{dz} \right| \tag{E-20}$$

The relationship between v and z for various debris ions has been reported in Reference E-4 and is graphically illustrated in Figure E-1. We have used the results in Figure E-1 to determine $v(z)$ for U^+ and $A\ell^+$ ions (although the results for $A\ell^+$ are not used here), assuming magnetic dip and pitch angles of 75° and 45°, respectively. The results, shown in Figure E-2, can be expressed analytically as

$$v \approx \exp(a_o + a_1 z + a_2 z^2) \qquad (cm\ sec^{-1}) \tag{E-21}$$
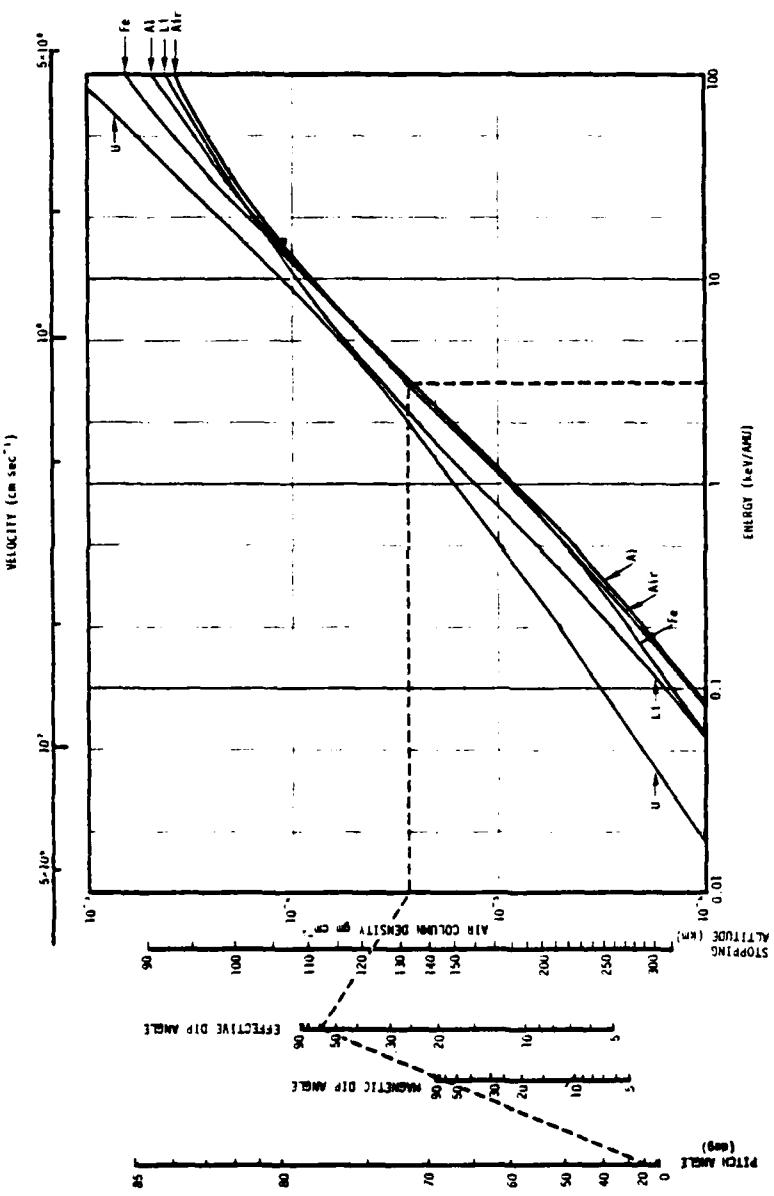
Figure E-1. Ranges for various particles in air. CIRA Model 5, Hour 8 atmosphere used to correlate stopping altitude with air column density (from Reference E-4).

103
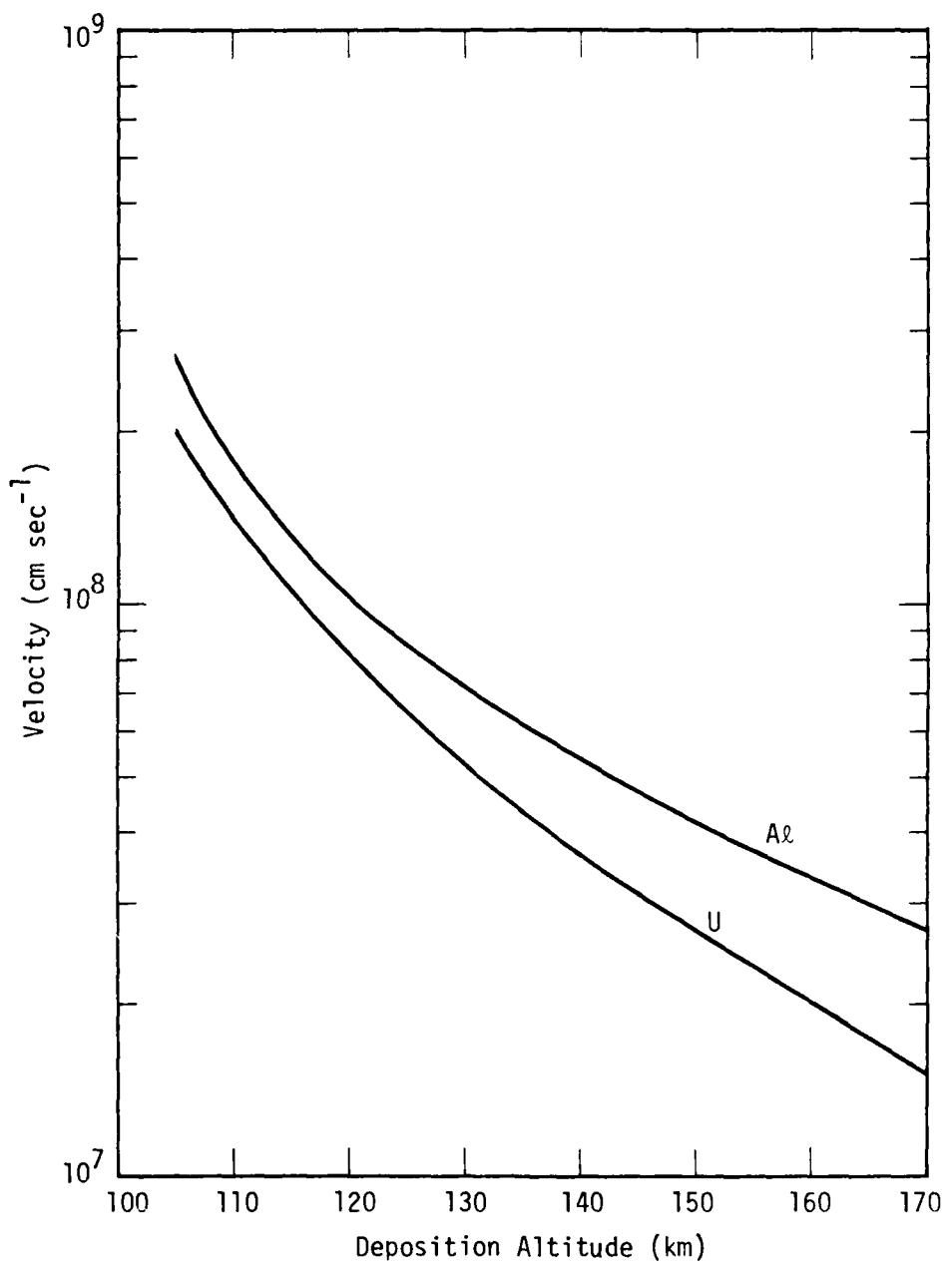
Figure E-2. Deposition altitude as a function of particle velocity.

where z is the altitude in km. Equations E-20 and E-21 then lead to the results

$$[N_i(z)]_{case\ 1} = \frac{Nv_o f}{(1-f)}\ \left|a_1 + 2a_2 z\right| \exp[-(a_o + a_1 z + a_2 z^2)]\qquad(E-22)$$

and

$$[N_i(z)]_{case\ 2} = \frac{N}{v_o}\ \left|a_1 + 2a_2 z\right| \exp(a_o + a_1 z + a_2 z^2)\qquad(E-23)$$

where, for uranium, $a_o = 30.24$, $a_1 = -0.148$, $a_2 = 4 \times 10^{-4}$.

Figure E-3 shows the Case 1 results for $f = 0.1$ and $f = 1/3$. The lowest altitude reached is 105 km, which is attained by those uranium ions with the peak velocity of 2×10^8 cm sec^{-1} (see Figure E-2). The highest altitude of deposition occurs for those ions with $v = v_{min} = fv_o$. These altitudes are about 160 km and 125 km for $f = 0.1$ and $1/3$, respectively. The peak in the distributions is seen to occur at or near the top of the layer.

Figure E-4 shows the Case 2 results for $f = 1/3$. Since $v_{max} = v_o$, the lowest altitude is again 105 km. However, since $v_{min} = 0$, there is no maximum altitude for the distribution in Case 2 as there is in Case 1, but rather a monotonic decrease in the vertical distribution with increasing altitude from the peak at the lower boundary of the layer.

LATER VERTICAL DISTRIBUTION OF DEBRIS IONS

The vertical distributions shown in Figures E-3 and E-4 will be altered in time due to heave that results from atmospheric heating above about 100 km by deposition of the air-ion kinetic energy. Specifically, if z_1 is the altitude at time t of an air parcel that was initially at altitude z, then the vertical distribution, $N(z_1,t)$, at time t is

$$N(z_1,t) = N_i(z)\ \left(\frac{dz}{dz_1}\right)_t \qquad . \qquad(E-24)$$
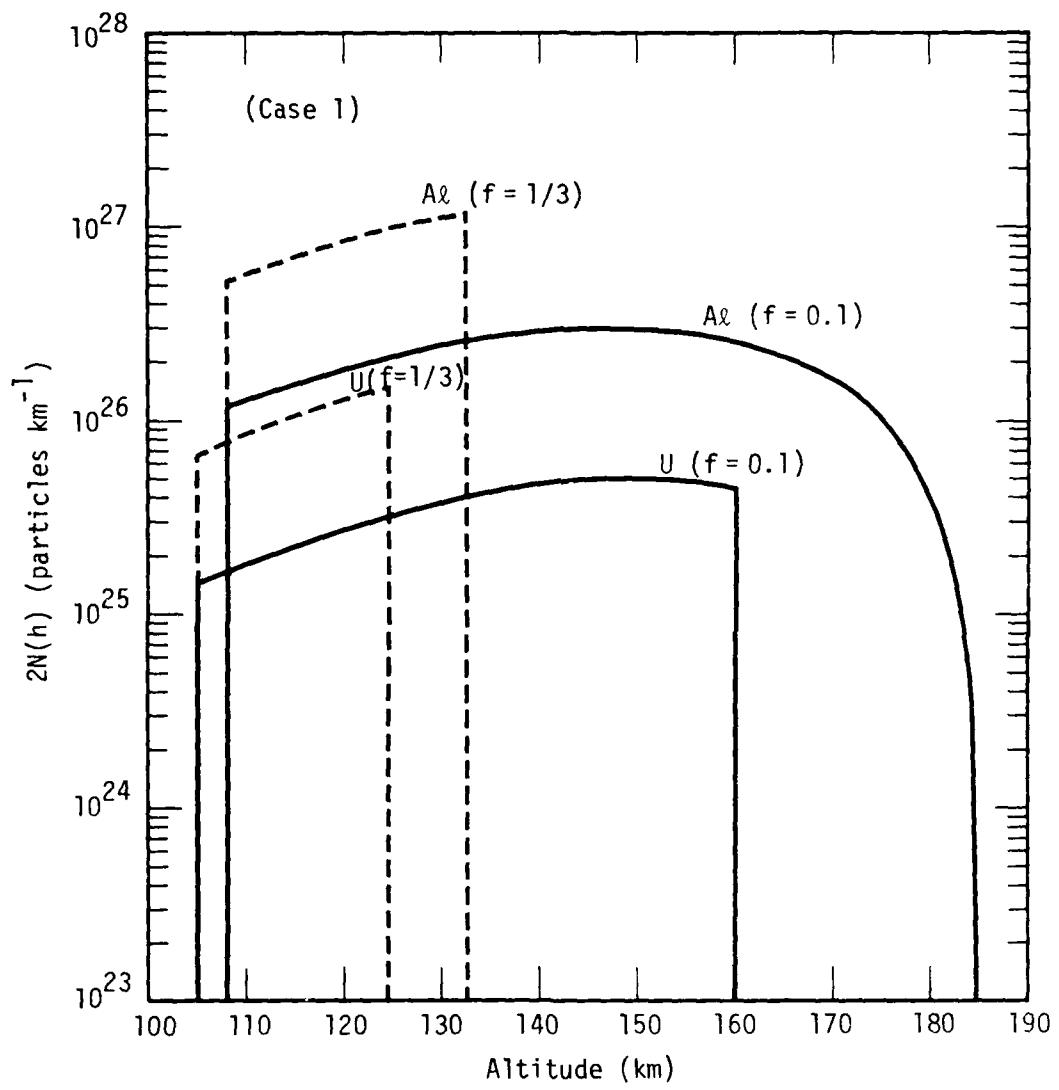
Figure E-3. "Initial" distribution of debris particles for case where
$N(v) \propto v^{-2}$ and $v_0 = 2 \times 10^8$ cm sec^{-1}, $N(U) = 7 \times 10^{26}$,
$N(A\ell) = 10^{28}$. Results shown for cases where fraction,
f, of original particle energy left is 0.1 and 1/3.

106
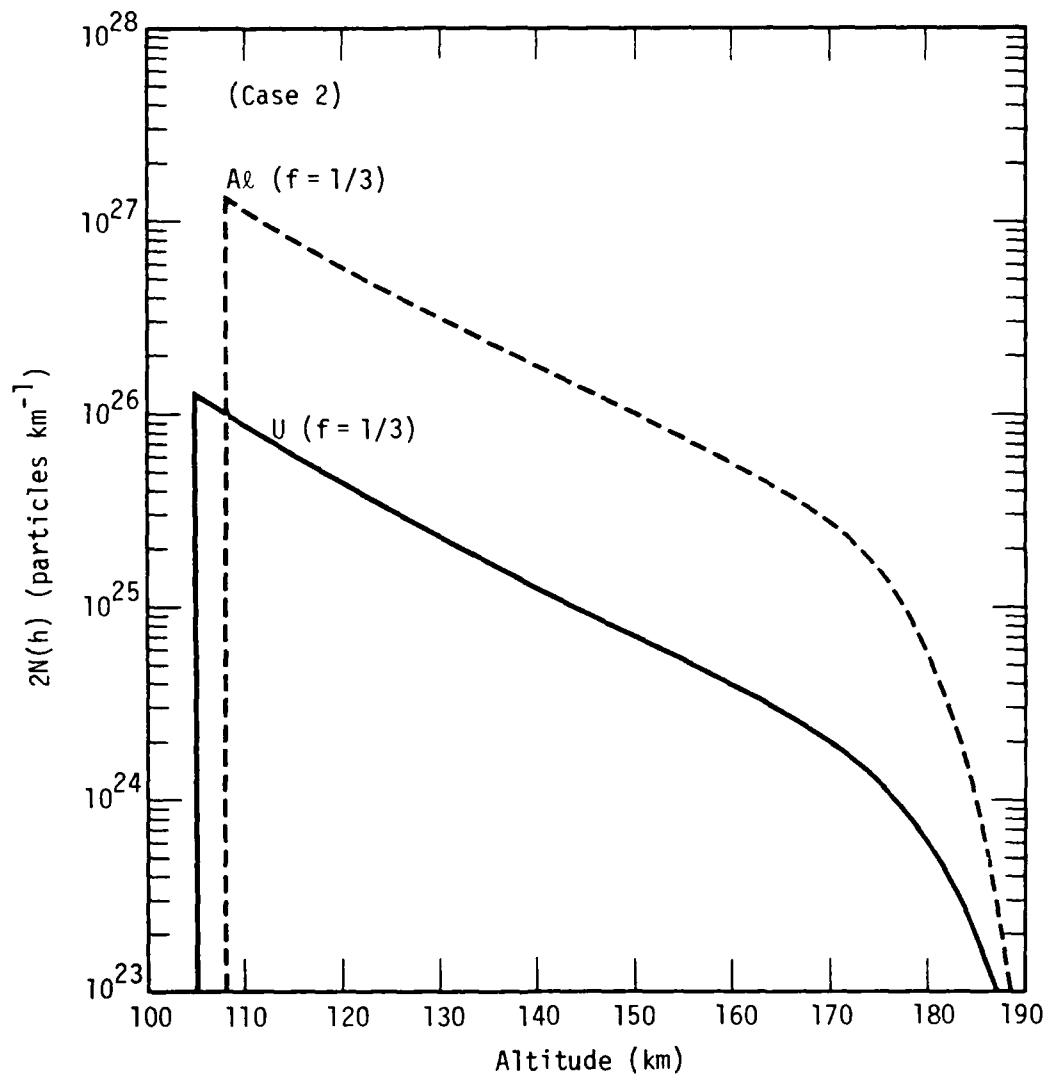
Figure E-4. "Initial distribution of debris particles for case where
$N(v)$ = constant and $v_0 = 2 \times 10^8$ cm sec^{-1}, $N(U) = 7 \times 10^{26}$,
$N(A\ell) = 10^{28}$, $f = 1/3$.

Values for $(dz/dz_1)_t$ have been obtained from the Lagrangian representation of MICE-code results, at selected times, for the case of a megaton-class, high-altitude burst. These values, together with Equations E-22 and E-23, have been used in Equation E-24 to obtain vertical distributions at later times.

In partitioning the ions between atomic and oxide species, account must be taken of the fact that oxide ions will form only in regions where O_2 is not dissociated. In fact, because of the fast rate of oxide ion formation (see, for example, Reactions 3-17 and 3-18), and the large dissociation energies for the ions (≈ 8 eV), we assume that an atomic uranium or (appropriate) fission-fragment ion will form an oxide ion, and so remain, if at any time it finds itself in a region where O_2 is not dissociated. Such regions are indicated in Figure E-5 that shows the MICE-code computed altitude of the dissociation boundary, as a function of time, along vertical paths displaced by 0, 50, and 100 km from the burst point. Points above the curves correspond to regions inside the fireball plume where O_2 is dissociated.

The foregoing considerations have been applied in determining the vertical distributions of atomic uranium ions and uranium oxide ions (assumed to be mainly UO_2^+) at times of 60, 210, 420, and 540 sec after burst. The results for Case 1 ($f = 0.1$) and Case 2 ($f = 1/3$) are shown in Figures E-6 and E-7, respectively.* In Figure E-6, we see that at each time there are essentially two layers formed; one, peaking at altitudes below about 300 km, consists of oxide ions; the other, peaking at higher altitudes, consists of U^+ ions. At 540 sec the debris is beginning to fall back down and, by compression, produces a narrow, high concentration layer of UO_2^+ near 170 km.

---

* The values in Figures E-6 and E-7 are given in terms of concentrations by assuming that the debris is distributed in a cylinder of diameter equal to 200 km. Any lateral variation in the concentration is unimportant for determination of the limb radiance since it is only the total number of oxide ions in a horizontal column that matters.
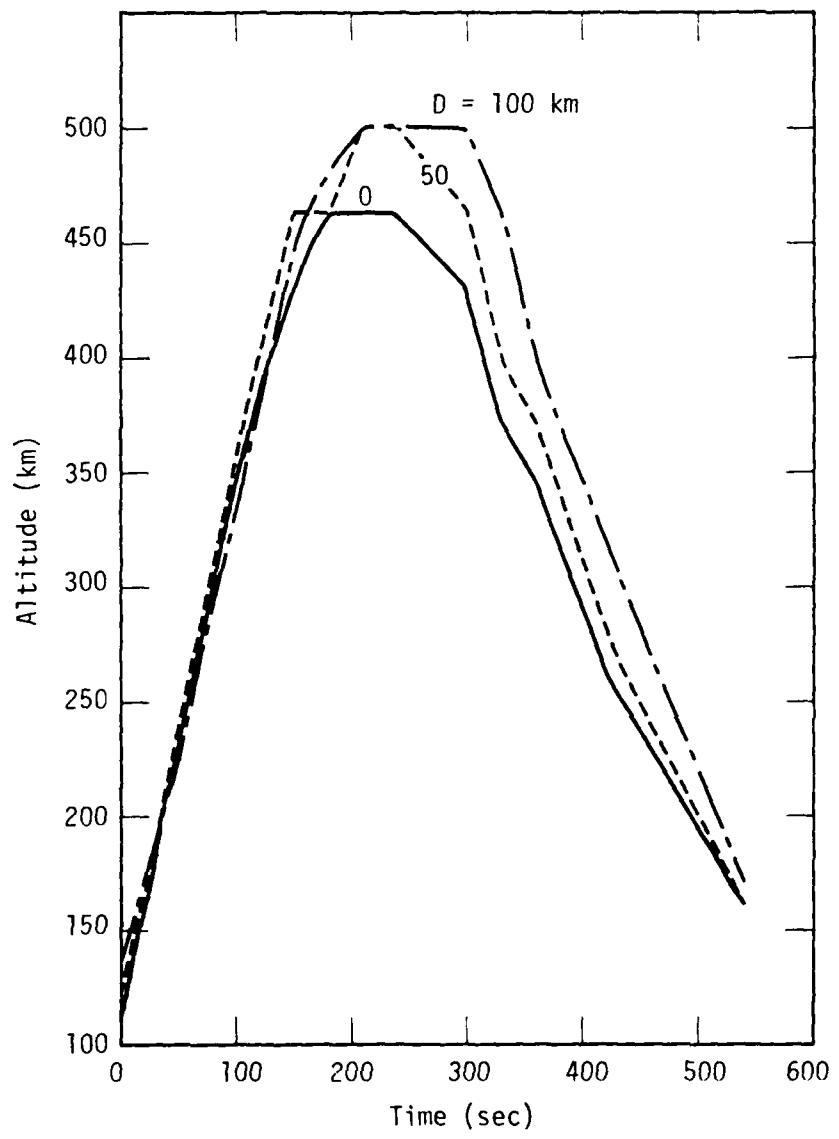
Figure E-5. Altitude of O_2 dissociation boundary for three radial
distances, D, from megaton-class high-altitude
burst point.
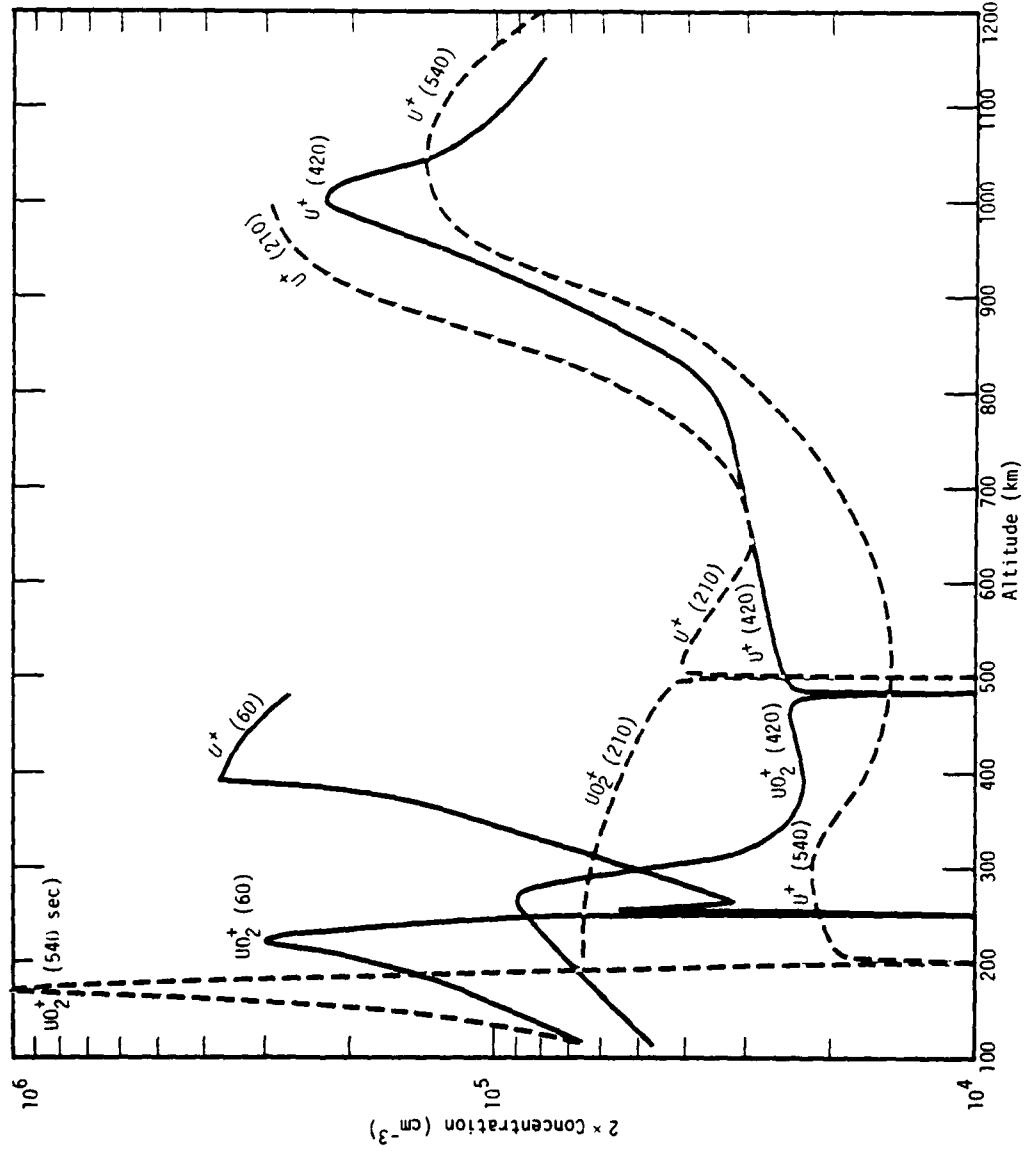
Figure E-6. Estimated concentration profiles of U^+ and UO_2^+ at selected times following a megaton-class high-altitude burst (Case 1; $f = 0.1$).

110
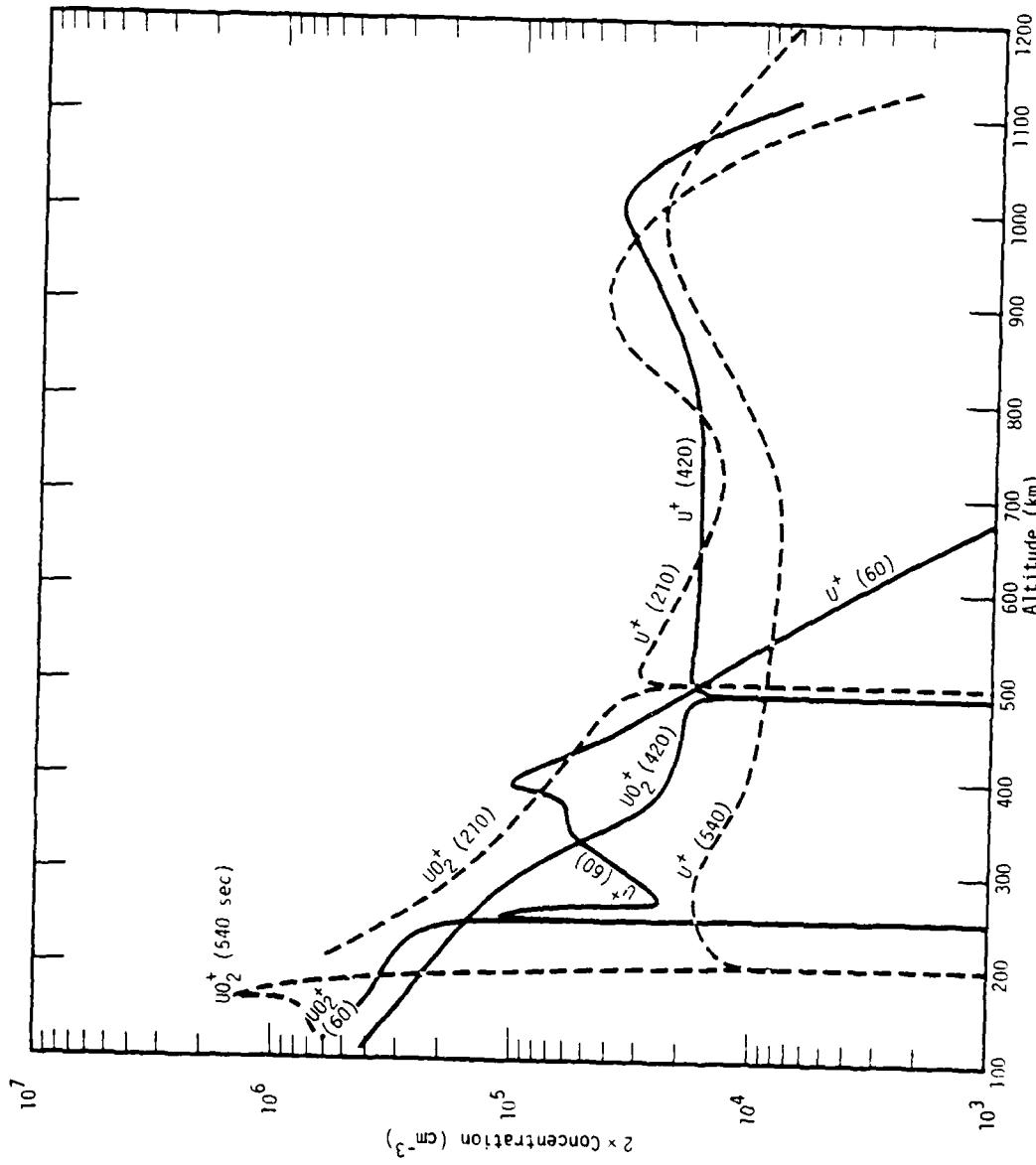
Figure E-7. Estimated concentration profiles of U^+ AND UO_2^+ at selected times following a megaton-class high-altitude burst (Case 2; $f = 1/3$).

111

Figure E-7, for Case 2, shows a generally similar behavior to that for Case 1, although the concentration in the high-altitude U^+ layer i now less than it was in Case 2, and the peak in the oxide ion layer tends to occur at the lowest altitude in the layer (except at 540 sec where again the downward compression produces a narrow, high concentration layer near 170 km).

LIMB-RADIANCE RESULTS

Uranium Oxide Ions

Equation E-1, together with the results shown in Figures E-6 and E-7, has been used to compute the limb radiance from uranium oxide ions. In so doing, we have assumed that the radiation is emitted uniformly over the wavelength interval from 10.5 to 12.5 μm.* The results for Case 1, under nighttime and daytime conditions, are shown in Figures E-8 and E-9, respectively. The corresponding results for Case 2 are shown in Figures E-10 and E-11.

From Figure E-9 we see that for Case 1 in the day, at times of 60, 210, 420, and 540 sec, the radiance exceeds 10^{-10} watts cm^{-2} $ster^{-1}$ $μm^{-1}$ for altitudes to about 250, 500, 300, and 200 km, respectively. Similarly, from Figure E-11 we see that, although the radiance curves differ in detail from those in Figure E-9 for Case 1, the altitude regions and times for which the radiance exceeds 10^{-10} are nearly the same in both cases. From this it appears that the answer to the question of whether or not debris-oxide emission will adversely affect LWIR systems, does not depend critically on the form assumed for the velocity distribution function of the debris ions.

---

* The $ν_1$ and $ν_3$ absorption peaks of UO_2^+ have tentatively been identified as occurring at 12.0 and 11.2 μm, respectively (Reference E-5). Rotational spreading of these bands should provide emission approximately over the indicated interval, albeit not uniformly.
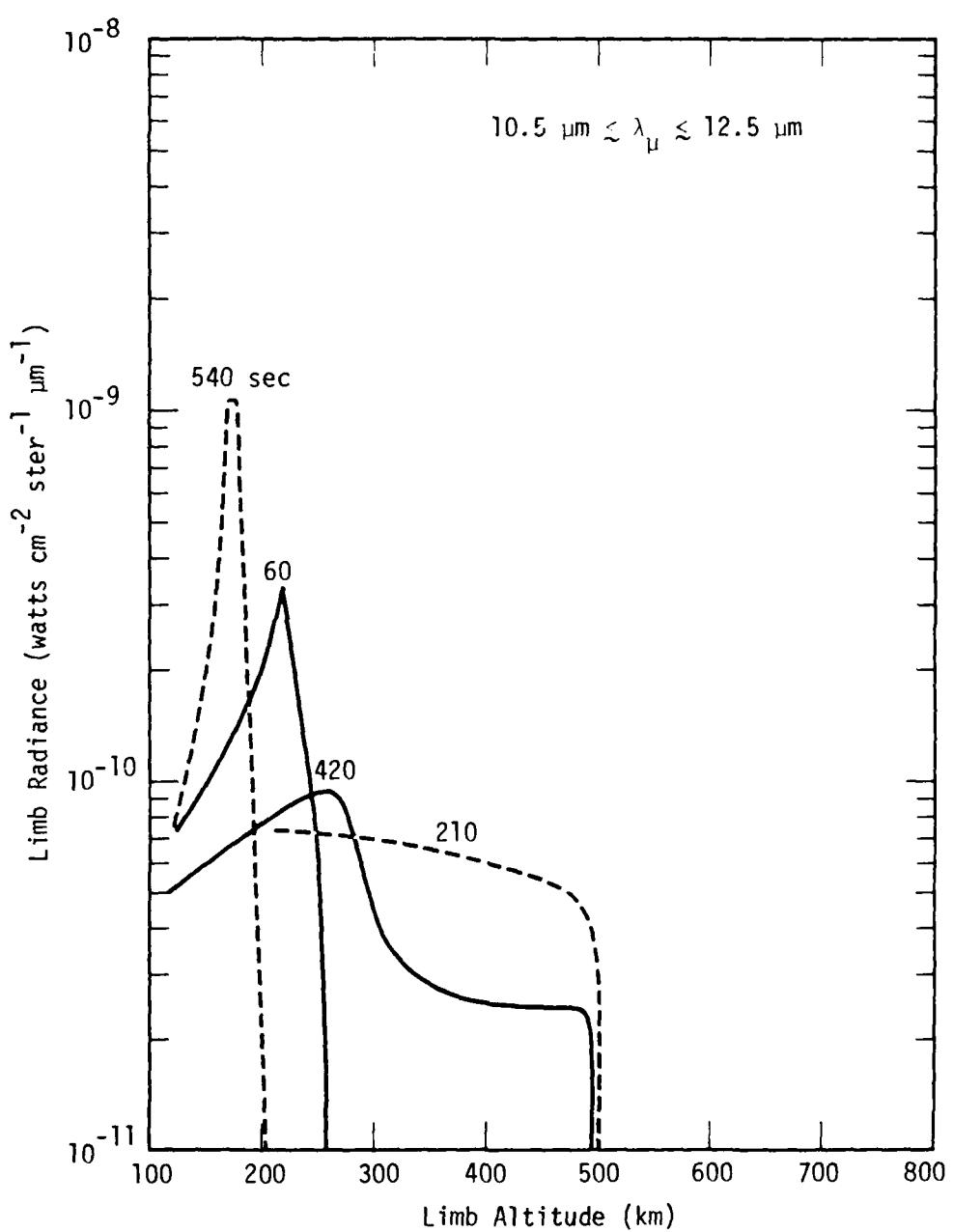
Figure E-8. Estimated nighttime limb radiance from UO_2^+ at selected times following a megaton-class high-altitude burst (Case 1; f = 0.1).

113
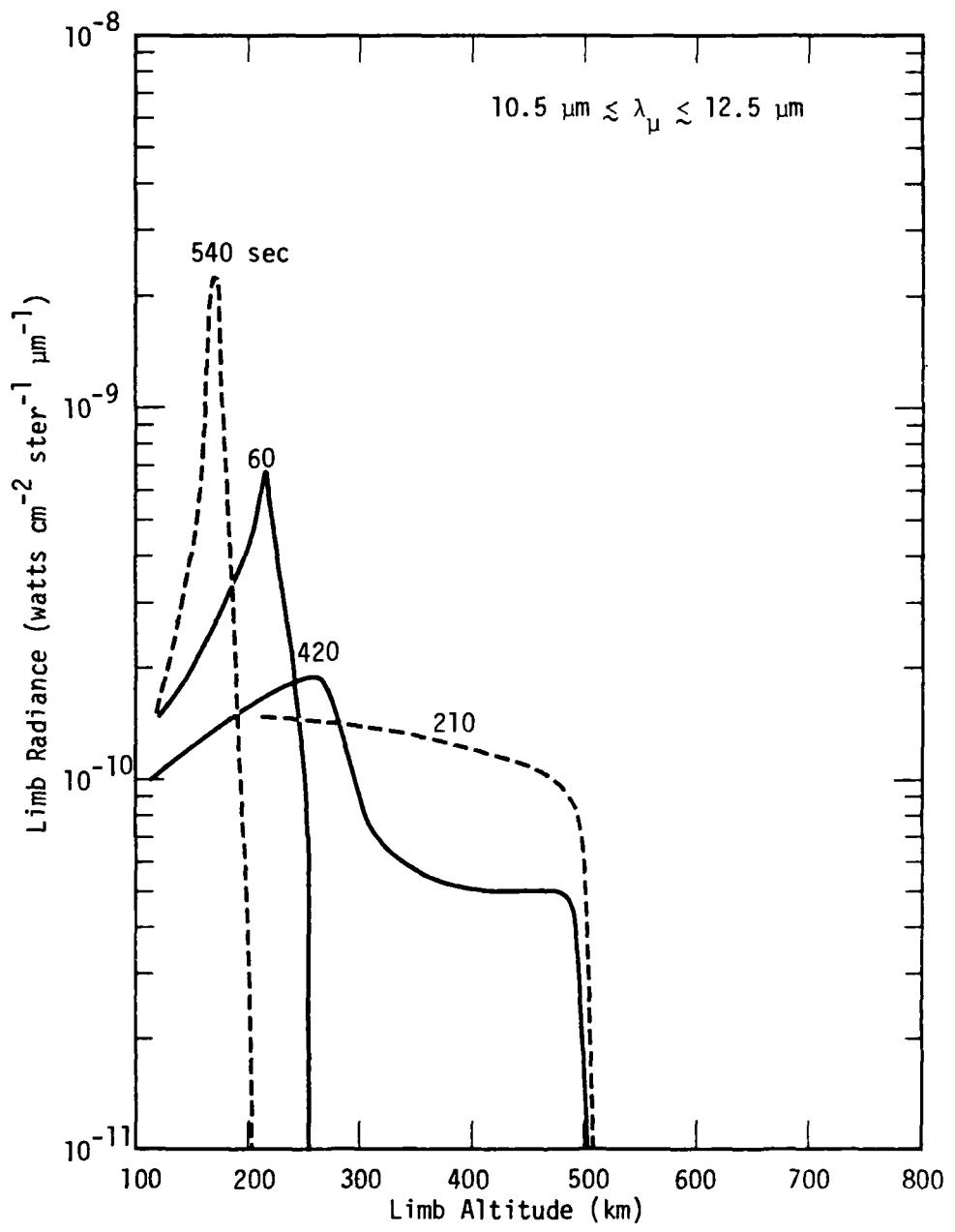
Figure E-9. Estimated daytime limb radiance from UO_2^+ at selected times following a megaton-class high-altitude burst (Case 1; $f = 0.1$).
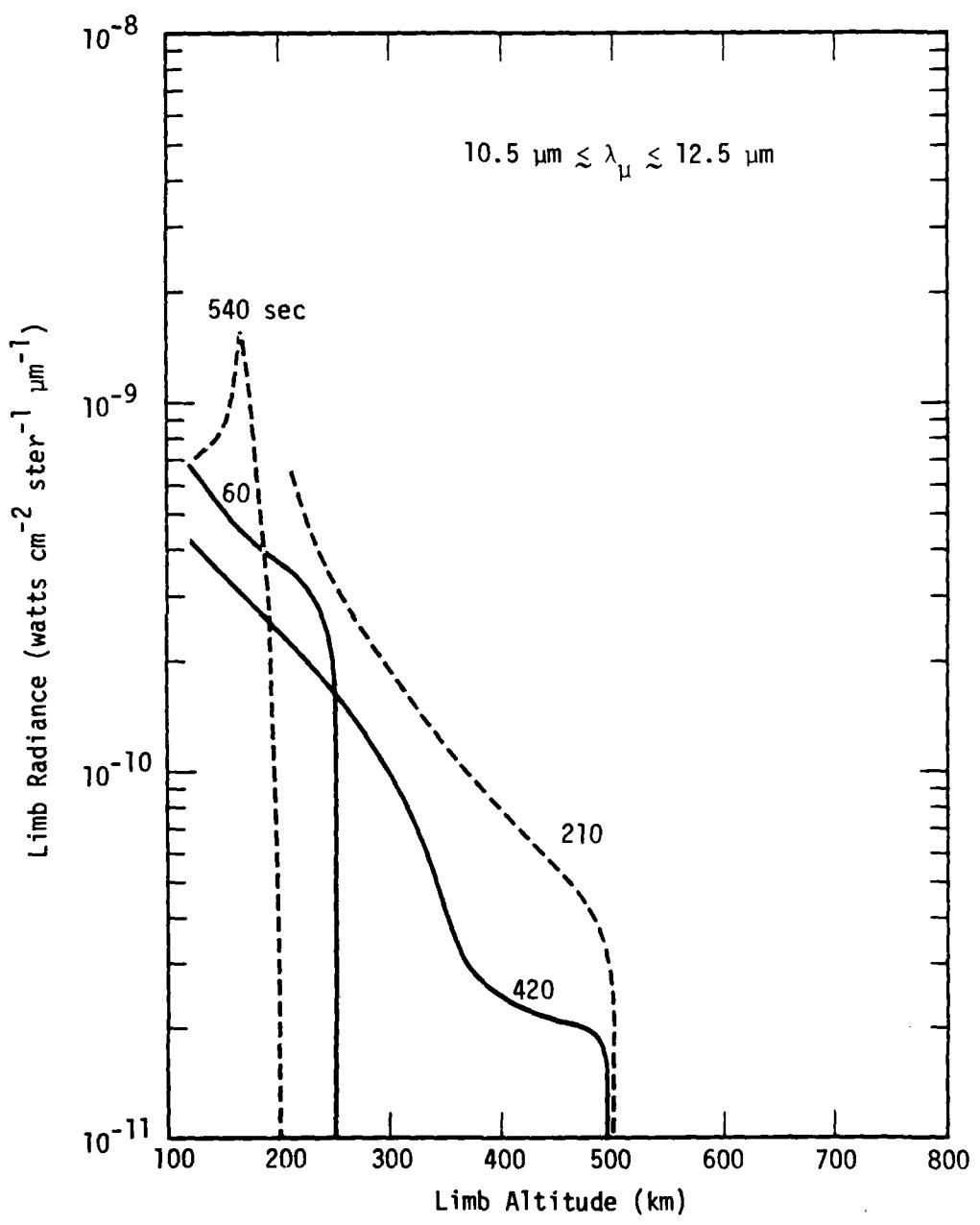
Figure E-10. Estimated nighttime limb radiance from UO_2^+ at selected times following a megaton-class high-altitude burst (Case 2; f = 1/3).
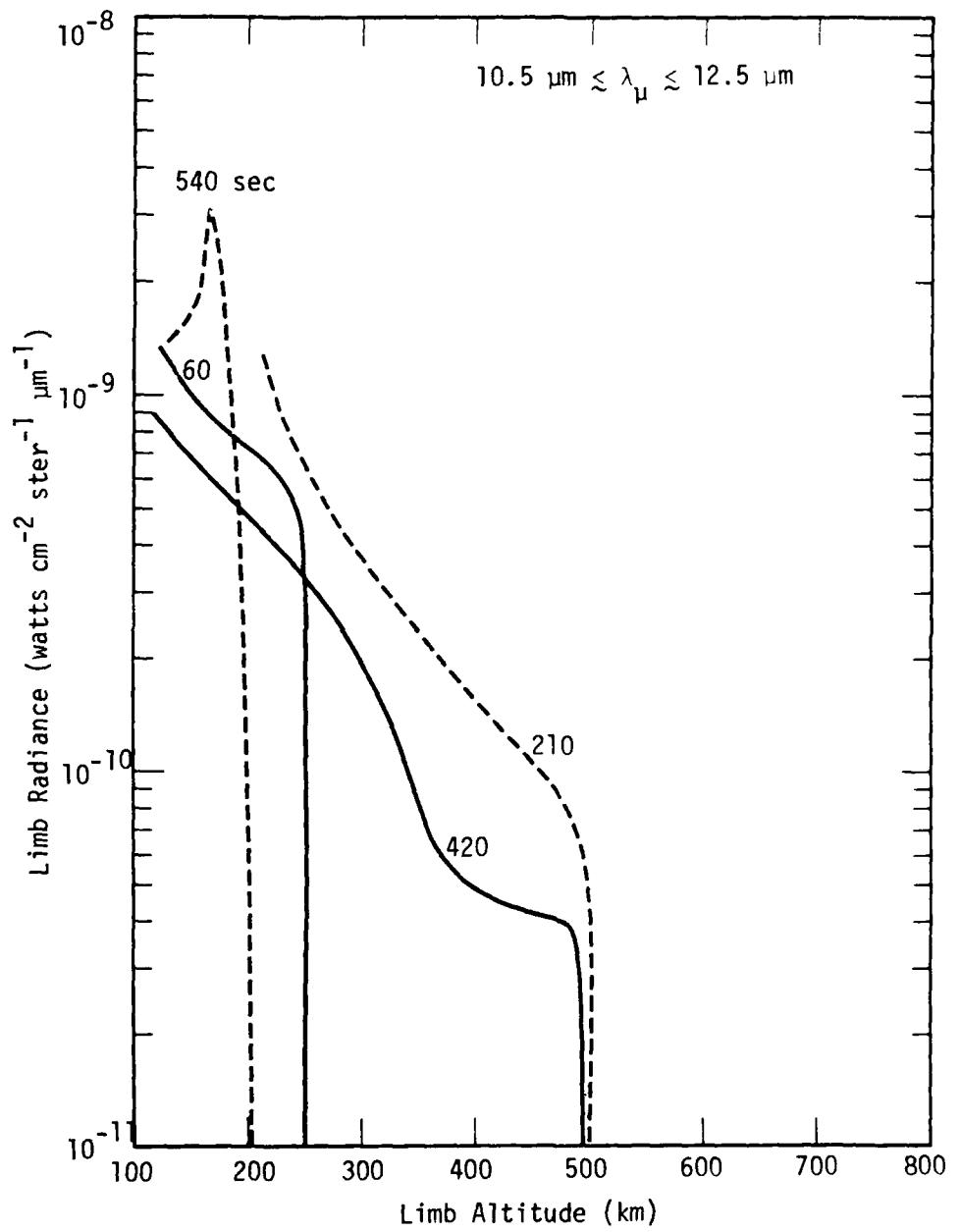
Figure E-11. Estimated daytime limb radiance from UO_2^+ at selected times following a megaton-class high-altitude burst (Case 2; f = 1/3).

Fission-Fragment Oxide Ions

As indicated above, certain of the fission-fragment ions behave like U^+ in that they can react with O_2 to form stable oxide ions. The ones that we have found, representing about 40 percent of the mass yield from the fission of U^{235}, are Zr, La, Sm, Nd, Y, Ce, and Pr. To our knowledge, the wavelengths of the fundamentals of their oxide ions are not known, although the band positions for the neutral monoxides are known for all except SmO and NdO. Figure E-12 shows the approximate emission regions for four of the known bands of these oxides at a temperature of 1000 °K. (The position of the PrO fundamental is nearly the same as that for LaO.) From this figure, and for lack of more definitive information, we assume that the fission-fragment oxide ions radiate uniformly over the spectral region from 9.5 to 13.5 μm.

The limb radiance from the fission-fragment oxide ions has been estimated by scaling the UO_2^+ results (shown in Figures E-8 through E-11), allowing for the different number of particles involved and the different assumed bandwidth. The results are shown in Figures E-13 through E-16. The curves are similar to those shown in Figures E-8 through E-11 for UO_2^+ except that the magnitude of the emission is somewhat lower because of the smaller number of fission fragments involved and the larger bandwidth assumed for the emission.

Not reflected in Figures E-13 to E-16 is the fact that, initially, the lower boundary of the fission-fragment layer will be somewhat higher that that for the uranium layer because the uranium ions, being heavier, can penetrate to lower altitudes. However, allowance for this has been made in the representations shown in Figures 3-9 to 3-13.

117
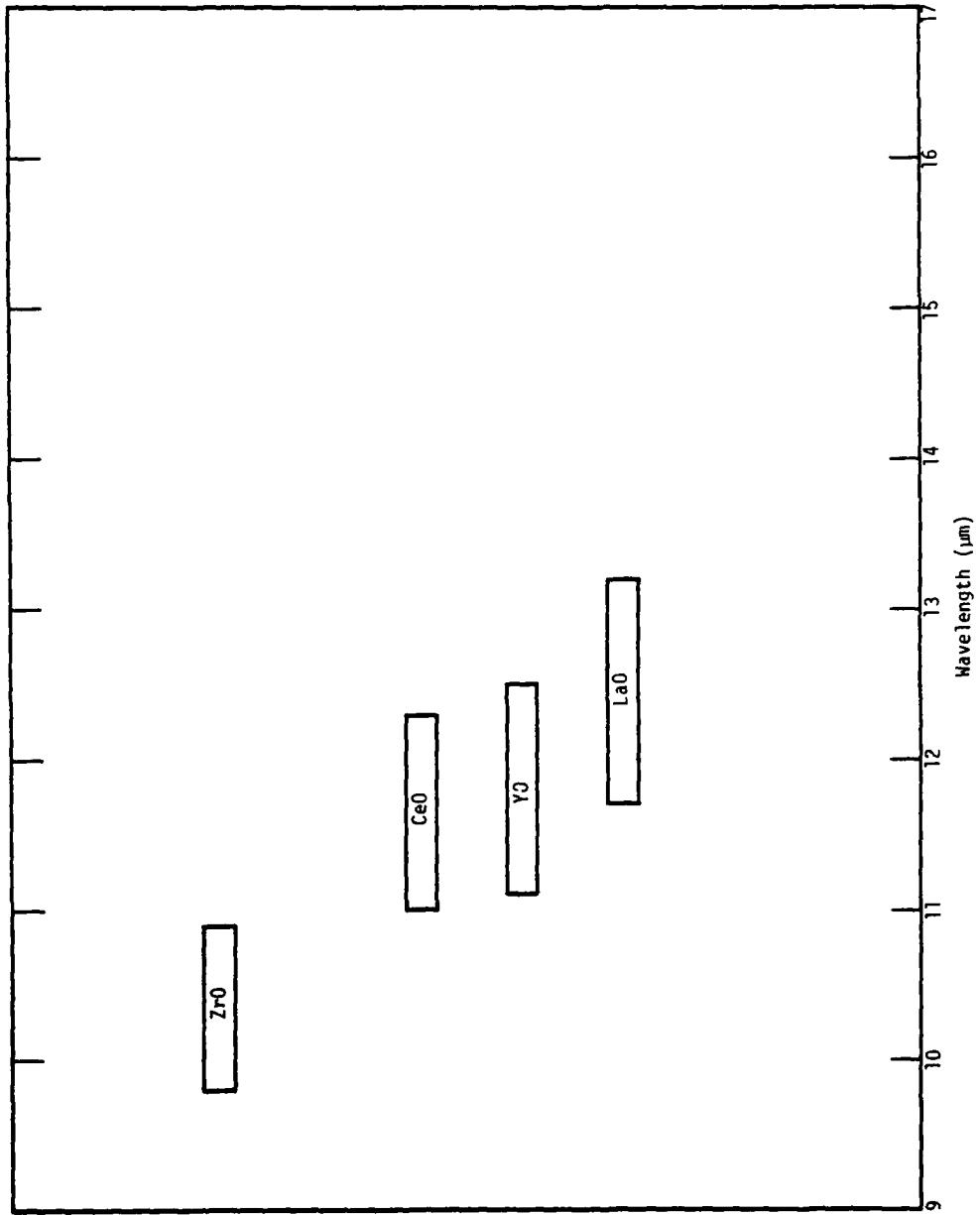
Figure E-12. Position of (1,0) bands of some fission-fragment oxides at 1000°K.
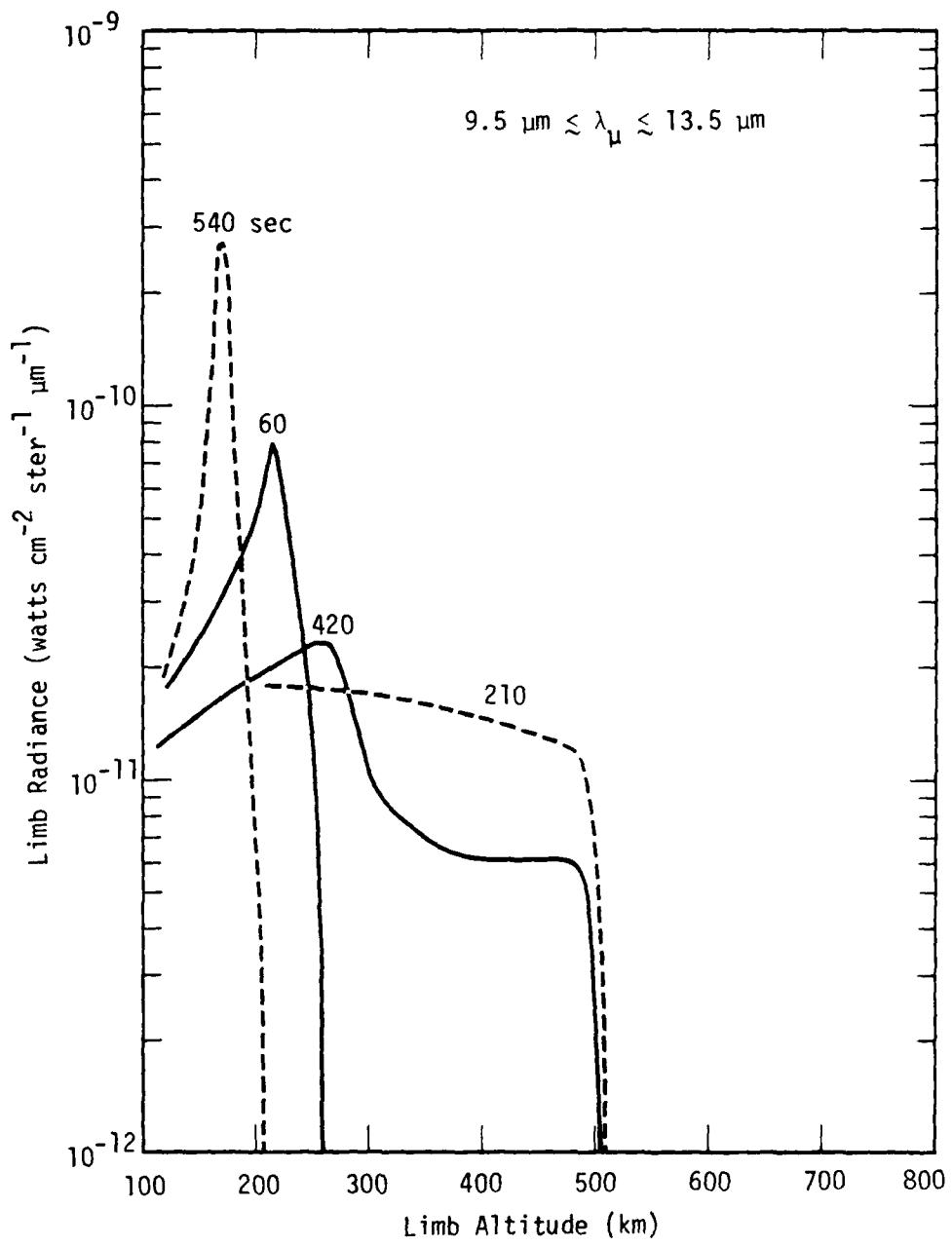
Figure E-13. Estimated nighttime limb radiance from fission-fragment oxides at selected times following a megaton-class high-altitude burst (Case 1; f = 0.1).

119
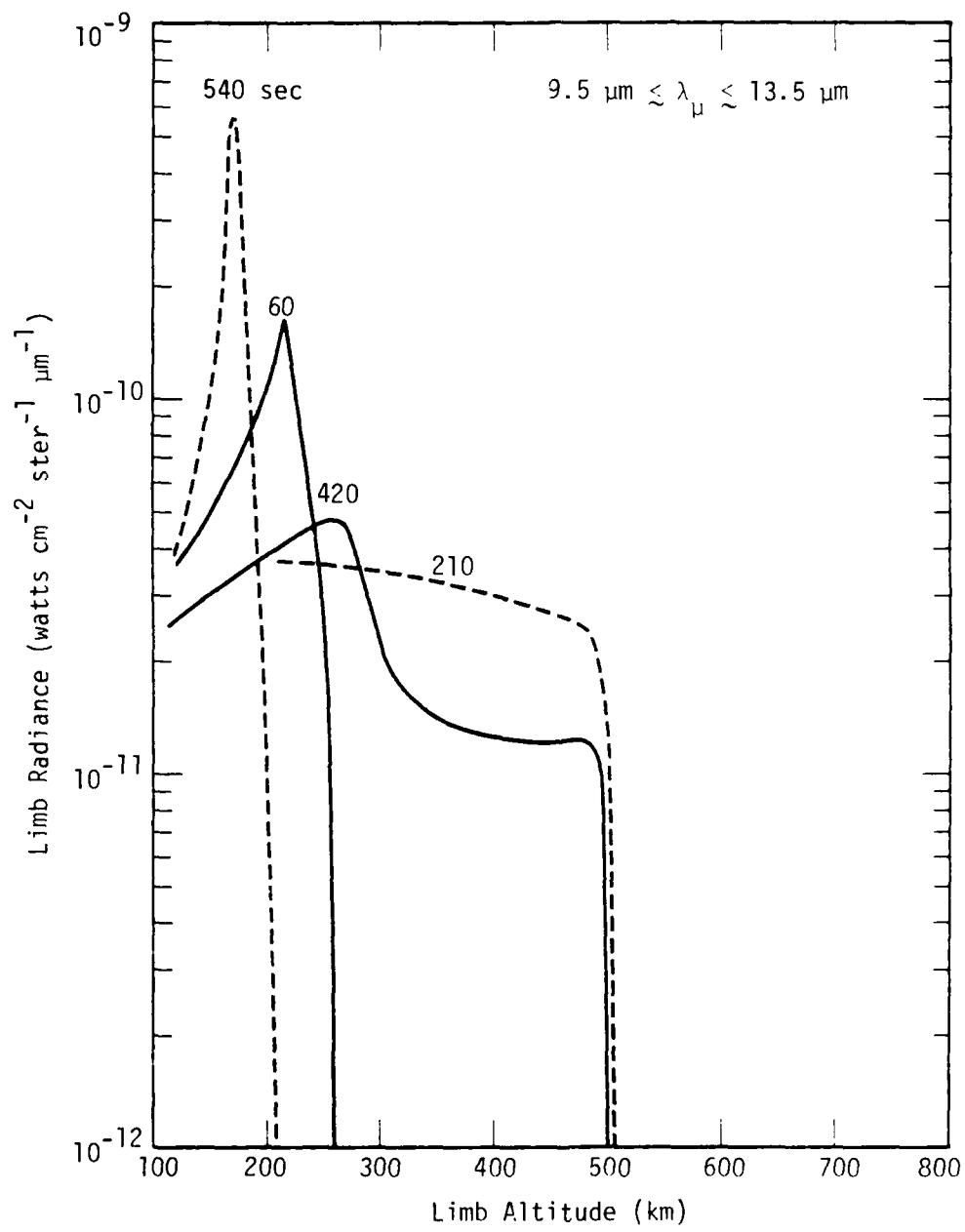
Figure E-14. Estimated daytime limb radiance from fission-fragment oxides at selected times following a megaton-class high-altitude burst (Case 1; f = 0.1).

120
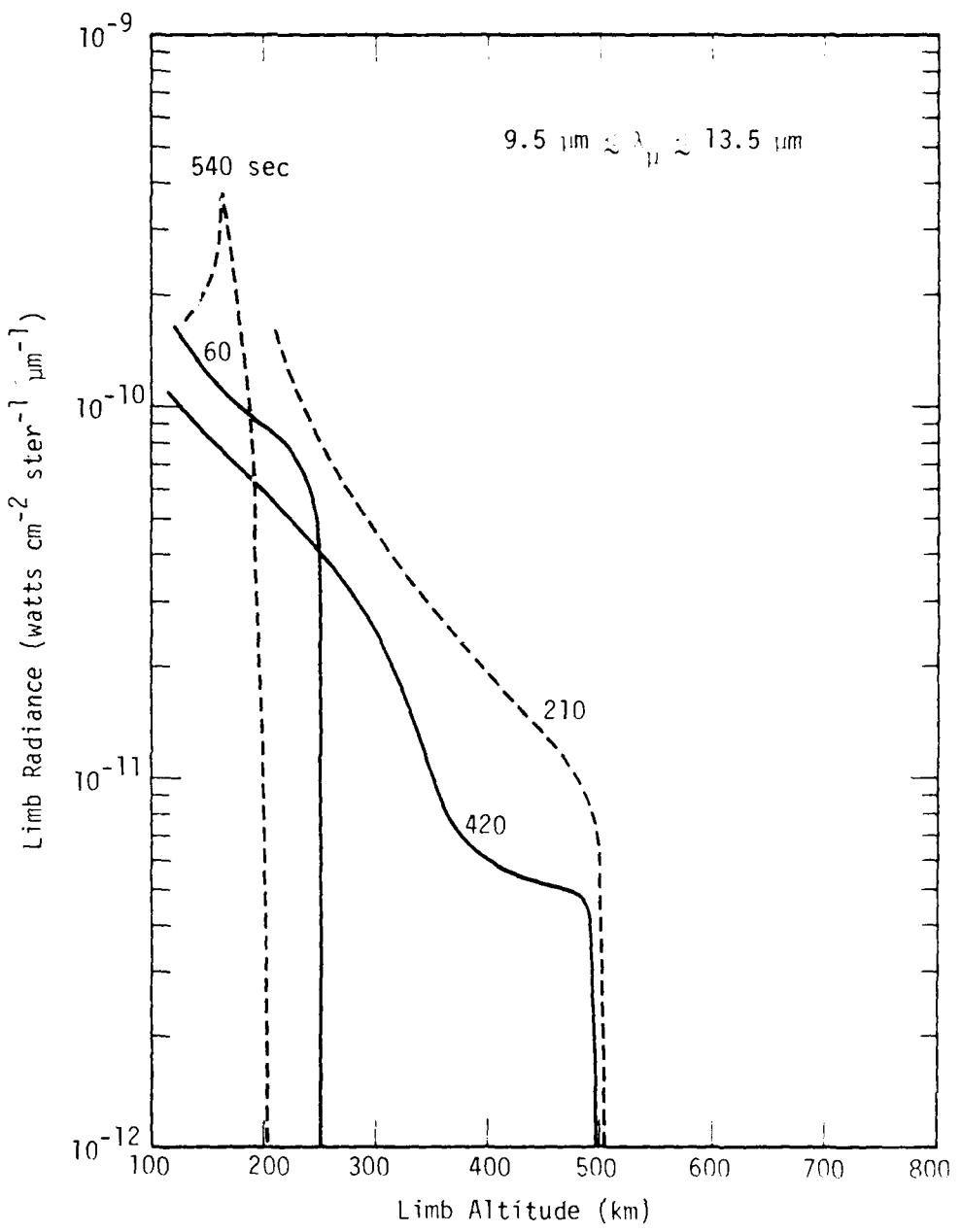
Figure E-15. Estimated nighttime limb radiance from fission-fragment oxides at selected times following a megaton-class high-altitude burst (Case 2; f = 1/3).
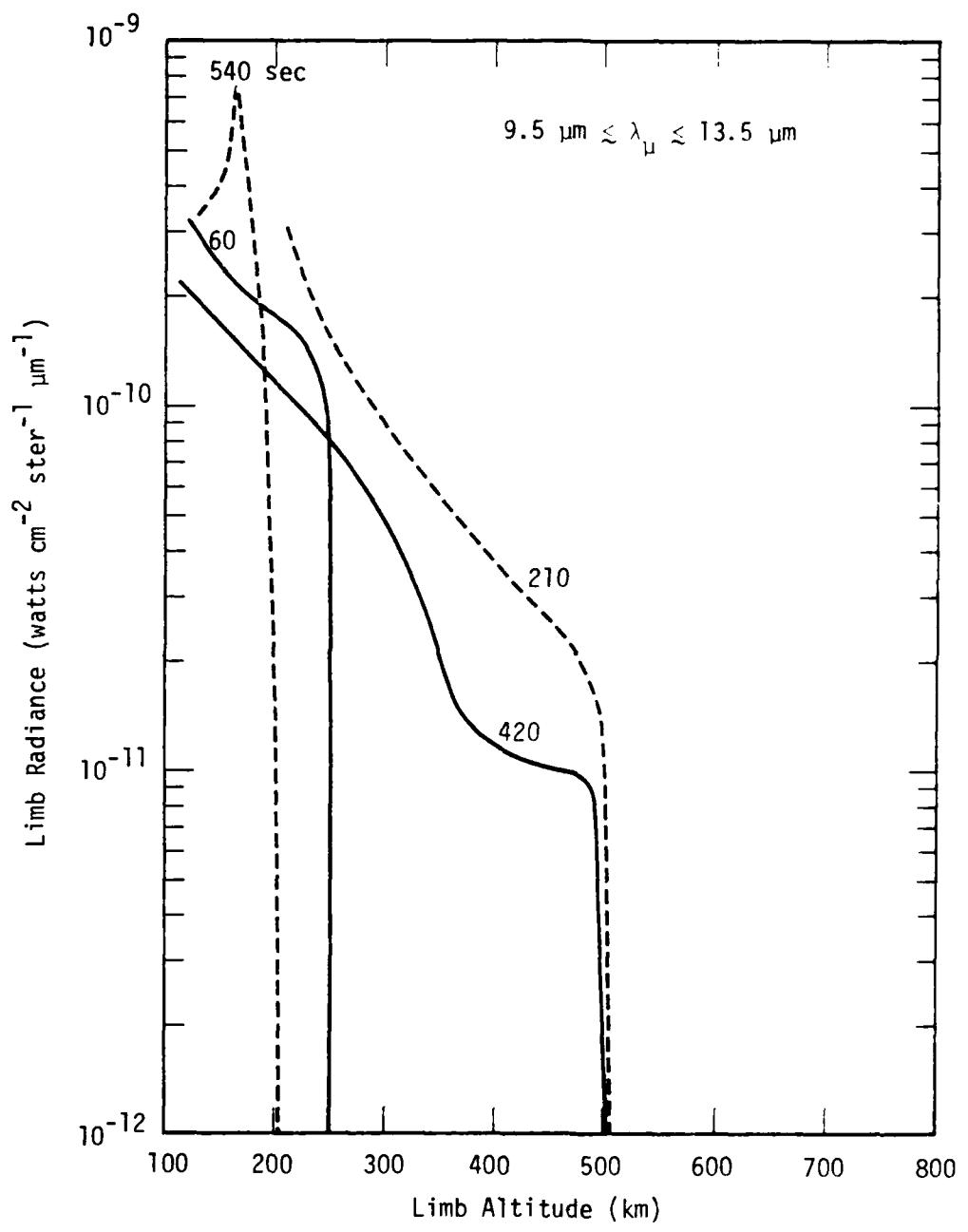
Figure E-16. Estimated daytime limb radiance from fission-fragment oxides
at selected times following a megaton-class high-altitude
burst (Case 2; f = 1/3).

REFERENCES (APPENDICES)

A-1.   McCaa, D. J., and J. H. Shaw, J. Mol. Spectr. 25, 374 (1968).

A-2.   Rosen, D. I., and T. A. Cool, J. Chem. Phys. 59, 6097 (1973).

A-3.   Stephens, T. L., General Electric-TEMPO, Private Communication 1979.

B-1.   Guttman, A., J. Quant. Spectr. Rad. Transf. 2, 1 (1962).

B-2.   Shafer, J. H., and C. Young, App. Opt. 15, 2551 (1976).

B-3.   Goldman, A., et al., J. Quant. Spectr. Rad. Transfer 15, 107 (1975).

B-4.   Golde, M. F., and F. Kaufman, Chem. Phys. Lett. 29, 480 (1974).

C-1.   Physics of High-Altitude Nuclear Burst Effects, Ch. 7, DNA 4501F, MRC-R-30, Mission Research Corporation, December 1977.

C-2.   Kneizys, F. X., et al., Atmospheric Transmittance/Radiance: Computer Code LOWTRAN 5, AFGL-TR-80-0067, Air Force Geophysics Laboratory, 21 February 1980.

C-3.   Kunitomo, T., et al., J. Quant. Spectr. Radiative Transfer, 18, 405 (1977).

C-4.   Burch, D., and D. Williams, App. Optics 1, 474 (1962).

C-5.   Gilmore, Forrest, R & D Associates, Private Communication, September 1980.

C-6.   Myers, B. F., and M. R. Schoonover, UV Photon and Electron Deposition in the Atmosphere, DNA 4068F, Science Applications, Inc., 2 August 1976.

E-1.   Dunn, M. G., et al., Radiation Studies of Metal-Oxygen Mixtures, DNA 3624F, Calspan Corporation, 1 August 1975.

E-2.   Johnson, S. E., et al., J. Chem. Phys. 56, 663 (1972).

E-3.   Sharma, A., J. Quant. Spectr. Rad. Transfer 7, 289 (1967).

E-4.   Physics of High-Altitude Nuclear Burst Effects, Ch.4. p.222, DNA 4501F, MRC-R-30, Mission Research Corporation, December 1977.

E-5.   Green, D. W., et al., J. Chem. Phys. 64, 1697 (1976).

DISTRIBUTION LIST

DEPARTMENT OF DEFENSE

Assistant to the Secretary of Defense
Atomic Energy
    ATTN: Executive Assistant

Defense Nuclear Agency
    ATTN: RAAE, H. Fitz, Jr
    ATTN: RAAE, P. Lunn
    ATTN: RAAE, W. McKechney
4 cy ATTN: TITL

Defense Technical Information Center
12 cy ATTN: DD

Field Command
Defense Nuclear Agency
    ATTN: FCPR

Field Command
Defense Nuclear Agency
Livermore Branch
    ATTN: FCPRL

Undersecretary of Def for Rsch & Engrg
    ATTN: Strategic & Space Sys (OS)
    ATTN: Defensive Systems

DEPARTMENT OF THE ARMY

Atmospheric Sciences Laboratory
U.S. Army Electronics R&D Command
3 cy ATTN: DELAS-EO, F. Niles

BMD Advanced Technology Center
Department of the Army
    ATTN: ATC-O, W. Davies
    ATTN: ATC-T, M. Capps

BMD Systems Command
Department of the Army
2 cy ATTN: BMDSC-HW

Deputy Chief of Staff for Rsch Dev & Acq
Department of the Army
    ATTN: DAMA-WSZ-C
    ATTN: DAMA-CSZ-C
    ATTN: DAMA-CSS-N

Electronics Tech & Devices Lab
U.S. Army Electronics R&D Command
    ATTN: Wpns Effects Section
    ATTN: DELET-R, S. Kronenberg
5 cy ATTN: DRSEL

Harry Diamond Laboratories
Department of the Army
2 cy ATTN: DELHD-N-P

U.S. Army Ballistic Research Labs
    ATTN: DRDAR-TSB-S
    ATTN: DRDAR-BLB, J. Mester

U.S. Army Foreign Science & Tech Ctr
    ATTN: DRXST-SD

DEPARTMENT OF THE ARMY (Continued)

U.S. Army Nuclear & Chemical Agency
    ATTN: Library

U.S. Army Research Office
2 cy ATTN: R. Mace

DEPARTMENT OF THE NAVY

Naval Electronic Systems Command
    ATTN: PME 117-20

Naval Intelligence Support Ctr
    ATTN: Document Control

Naval Ocean Systems Center
    ATTN: Code 5324, W. Moler

Naval Postgraduate School
    ATTN: Code 1424 Library

Naval Research Laboratory
    ATTN: Code 7175, J. Johnson
    ATTN: Code 2627
    ATTN: Code 4700, T. Coffey
    ATTN: Code 6750, D. Strobel
    ATTN: Code 7550, J. Davis
    ATTN: Code 6780, J. Fedder
    ATTN: Code 4780, S. Ossakow
    ATTN: Code 4709, W. Ali
    ATTN: Code 4701, J. Brown
    ATTN: Code 7122, D. McNutt

Naval Surface Weapons Center
    ATTN: Code F31
    ATTN: Code X211

DEPARTMENT OF THE AIR FORCE

Aeronautical Systems Division
Air Force Systems Command
    ATTN: ASD/YH-YEF, Capt Guice

Air Force Geophysics Laboratory
2 cy ATTN: OPR, J. Kennealy
2 cy ATTN: OPR, R. Murphy
2 cy ATTN: LKB, K. Champion
2 cy ATTN: LKD, R. Narcisi
2 cy ATTN: LKO, R. Huffman
4 cy ATTN: OPR, A. Stair

Air Force Office of Scientific Research
    ATTN: AFO, S. Rinc

Air Force Systems Command
    ATTN: DLAE
    ATTN: DLXP
    ATTN: Technical Library
    ATTN: DLTW
    ATTN: SDR
    ATTN: DLS

Air Force Weapons Laboratory
Air Force Systems Command
    ATTN: SUL

DEPARTMENT OF THE AIR FORCE (Continued)

Air Force Technical Applications Center
    ATTN: TF
    ATTN: Technical Library
    ATTN: TD

Air University Library
Department of the Air Force
    ATTN: AUL -LSE

Ballistic Missile Office
Air Force Systems Command
    ATTN: MNRTE

Deputy Chief of Staff
Research, Development, & Acq
Department of the Air Force
    ATTN: AFRDS

Headquarters Space Division
Air Force Systems Command
 3 cy ATTN: WE

Headquarters Space Division
Air Force Systems Command
    ATTN: SZJ, L. Doan

Headquarters Space Division
Air Force Systems Command
    ATTN: YN, P. Sivgals

Rome Air Development Center
Air Force Systems Command
    ATTN: OCSA, J. Simons

DEPARTMENT OF ENERGY

Department of Energy
    ATTN: OMA

OTHER GOVERNMENT AGENCIES

Central Intelligence Agency
    ATTN: OSWR/NED

Department of Commerce
National Bureau of Standards
    ATTN: A. Phelps

Department of Commerce
National Bureau of Standards
    ATTN: Sec Ofc for M. Krauss
    ATTN: Sec Ofc for J. Devoe
    ATTN: Sec Ofc for R. Levine
    ATTN: Sec Ofc for S. Abramowitz

Department of Commerce
National Oceanic & Atmospheric Admin
 3 cy ATTN: F. Fehsenfeld
 3 cy ATTN: E. Ferguson

Institute for Telecommunications Sciences
    ATTN: G. Falcon
    ATTN: W. Utlaut

OTHER GOVERNMENT AGENCIES (Continued)

NASA
Goddard Space Flight Center
    ATTN: Code 6801, A. Tempkin
    ATTN: Code 900, J. Siry
    ATTN: Technical Library
 3 cy ATTN: A. Aiken

NASA
George C. Marshall Space Flight Center
    ATTN: J. Watts
    ATTN: C. Balcher
    ATTN: W. Roberts
    ATTN: N. Stone
    ATTN: W. Oran

NASA
    ATTN: P. Kurzhals
    ATTN: A. Schardt
    ATTN: ST-5, D. Cauffman
    ATTN: J. Haughey

NASA
Langley Research Center
    ATTN: MS-168, C. Schexnayder

NASA
Ames Research Center
    ATTN: N-245-3, R. Whitten

NASA
Wallops Flight Center
    ATTN: J. Gray

DEPARTMENT OF ENERGY CONTRACTORS

Lawrence Livermore National Laboratory
    ATTN: L-262, D. Wuebbles
    ATTN: L-262, W. Duewer
    ATTN: L-10, H. Kruger
    ATTN: L-71, J. Chang
    ATTN: L-48, E. Woodward
    ATTN: L-325, G. Haugan

Los Alamos National Scientific Laboratory
    ATTN: H. Argo
    ATTN: G. Barrasch
    ATTN: M. Sandford
    ATTN: M. Pongratz
    ATTN: E. Jones
    ATTN: MS 362
    ATTN: R. Carlos
    ATTN: Librarian
    ATTN: G. Davis
    ATTN: R. Jeffries
    ATTN: MS 670, J. Hopkins

Sandia National Laboratories
Livermore National Laboratory
    ATTN: T. Cook

Sandia National Laboratories
    ATTN: Org 1250, W. Brown
    ATTN: M. Kramm
    ATTN: L. Anderson
    ATTN 3141

126

DEPARTMENT OF DEFENSE CONTRACTORS

Aero-Chem Research Labs, Inc
      ATTN: A. Fontijn

Aerodyne Research, Inc
      ATTN: F. Bien
      ATTN: M. Camac

Aeronautical Rsch Assoc of Princeton, Inc
      ATTN: H. Pergament

Aerospace Corp
      ATTN: J. Straus
      ATTN: I. Garfunkel
      ATTN: J. Reinheimer
      ATTN: N. Cohen
      ATTN: H. Mayer
      ATTN: T. Widhoph
      ATTN   V. Josephson

University of Alaska
      ATTN: J. Wagner
      ATTN: B. Watkins
3 cy ATTN: N. Brown

AVCO Everett Research Lab, Inc
      ATTN: C. Von Rosenberg, Jr
      ATTN: A830
      ATTN: Technical Library

Battelle Memorial Institute
      ATTN: H. Lamuth
      ATTN: R. Thatcher
      ATTN: STOIAC

Berkeley Research Associates, Inc
      ATTN: J. Workman

Boston College
2 cy ATTN: Chairman, Dept of Physics
2 cy ATTN: Chairman, Dept of Chemistry

Boston College
      ATTN: E. Hegblom
      ATTN: W. Grieder

University of California at Riverside
      ATTN: J. Pitts, Jr
      ATTN: A. Lloyd

California Institute of Technology
      ATTN: J. Ajello

University of California
      ATTN: W. Miller
      ATTN: H. Johnston
      ATTN: H. Strauss
      ATTN: F. Mozer

Calspan Corp
      ATTN: W. Wurster
      ATTN: C. Treanor
      ATTN: J. Grace
      ATTN: M. Dunn

DEPARTMENT OF DEFENSE CONTRACTORS (Continued)

University of Colorado
      ATTN: G. Lawrence-LASP
      ATTN: J. Pearce-LASP
      ATTN: C. Lineberger-JILA

Columbia University
      ATTN: H. Foley

Columbia University
      ATTN: B. Phelan

Concord Sciences
      ATTN: E. Sutton

Cornell University
      ATTN: M. Kelly

University of Denver
      ATTN: D. Murcray

University of Denver
      ATTN: B. Van Zyl

Environmental Rsch Inst of Michigan
      ATTN: IRIA Library

General Electric Co
      ATTN: M. Bortner
      ATTN: F. Alyea
      ATTN: P. Zavitsanos
      ATTN: J. Burns

General Electric Co
      ATTN: R. Edsall

Kaman Tempo
      ATTN: W. Knapp
      ATTN: V. Stull
      ATTN: B. Gambill
      ATTN: T. Stephens
      ATTN: K. Schwart
      ATTN: J. Jordano
5 cy ATTN: DASIAC

General Research Corp
      ATTN: J. Ise, Jr

Institute for Defense Analyses
      ATTN: H. Wolfhard
      ATTN: E. Bauer

Lockheed Missiles & Space Co, Inc
      ATTN: D. Divis

Lockheed Missiles & Space Co, Inc
      ATTN: R. Sears
      ATTN: M. Walt
      ATTN: J. Reagan
      ATTN: J. Cladis
      ATTN: J. Kumer
      ATTN: B. McCormac
      ATTN: T. James

University of Lowell
    ATTN: G. Best

University of Minnesota
    ATTN: J. Winkler

Mission Research Corp
    ATTN: M. Scheibe
    ATTN: D. Sappenfield
    ATTN: P. Fischer
    ATTN: D. Archer
5 cy ATTN: Tech Library

Pacific-Sierra Research Corp.
    ATTN: H. Brode

Photometrics, Inc
    ATTN: I. Kofsky

Physical Dynamics, Inc
    ATTN: A. Thompson

Physical Science Lab
    ATTN: W. Berning

Physical Sciences, Inc
    ATTN: K. Wray
    ATTN: R. Taylor
    ATTN: G. Caledonia

Physics International Co
    ATTN: Technical Library

University of Pittsburgh
    ATTN: F. Kaufman
    ATTN: M. Biondi
    ATTN: W. Fite

Princeton University
    ATTN: Librarian

R & D Associates
    ATTN: R. Turco
    ATTN: F. Gilmore
    ATTN: R. Lindgren
    ATTN: B. Gabbard
    ATTN: R. Lelevier
    ATTN: H. Ory
    ATTN: P. Haas

R & D Associates
    ATTN: J. Rosengren
    ATTN: B. Yoon

SRI International
    ATTN: W. Chesnut
    ATTN: R. Leadabrand
    ATTN: M. Baron
    ATTN: D. McDaniels

SRI International
    ATTN: C. Hulbert

Stewart Radiance Laboratory
    ATTN: R. Huppi

Technology International Corp
    ATTN: W. Boquist

Teledyne Brown Engineering
    ATTN: Technical Library
    ATTN: N. Passino

Utah State University
    ATTN: Sec Ofc for C. Wyatt
    ATTN: Sec Ofc for D. Burt
    ATTN: Sec Ofc for A. Steed
3 cy ATTN: Sec Ofc for D. Baker
3 cy ATTN: Sec Ofc for K. Baker

Visidyne, Inc.
    ATTN: C. Humphrey
    ATTN: W. Reidy
    ATTN: T. Degges
    ATTN: J. Carpenter
    ATTN: H. Smith

Wayne State University
    ATTN: R. Kummler

Wayne State University
    ATTN: W. Kauppila

Yale University
    ATTN: Engineering Dept

Rand Corp
    ATTN: C. Crain

Science Applications, Inc
    ATTN: D. Hamlin
    ATTN: D. Sachs

Space Data Corp
    ATTN: S. Fisher

Spectral Sciences, Inc.
    ATTN: F. Bein